Title

A First-Principles Investigation on Structural and Catalytic Properties of MoS2 Nanocatalysts for Hydrodesulfurization

Permalink

https://escholarship.org/uc/item/0sj6s2d2

Author

Joo, Paul Hyunggyu

Publication Date

2019

Peer reviewed|Thesis/dissertation

UNIVERSITY OF CALIFORNIA SAN DIEGO

A First-Principles Investigation on Structural and Catalytic Properties of MoS_2 Nanocatalysts for Hydrodesulfurization

A dissertation submitted in partial satisfaction of the
requirements for the degree
Doctor of Philosophy

in

Materials Science and Engineering

by

Paul Hyunggyu Joo

Committee in charge:

Professor Kesong Yang, Chair
Professor Prabhakar Bandaru
Professor Shengqiang Cai
Professor Zheng Chen
Professor Andrea Tao

2019

The dissertation of Paul Hyunggyu Joo is approved, and it is acceptable in quality and form for publication on microfilm and electronically:

Chair

University of California San Diego

2019

DEDICATION

To my family, friends, and God

TABLE OF CONTENTS

LIST OF FIGURES

LIST OF TABLES

ACKNOWLEDGEMENTS

First and mostly, I would like to express my sincere attitude to thesis advisor, Dr. Kesong Yang. Under his excellent guidance and support, I was able to plunge myself into the challenges in research during my graduate studies. His knowledge and passion in research had always inspired me and gave me the motivations to work harder.

I would also like to acknowledge my committee members, Professor Prabhakar Bandaru, Professor Shengqiang Cai, Professor Zheng Chen, and Professor Andrea Tao for making time to participate as the committee members and for their comments and advices to my research.

I also thank Dr. Maziar Behtash, Dr. Jianli Cheng, Yuheng Li, Sicong Jiang, and Joseph Wong for being the best lab mates from the beginning to the end. Their support has made this trip much easier for me to complete.

I cannot describe in words, how grateful I am to my parents, my sister, and my brother-in-law. They always gave me the love and support and never stopped praying for the path that I took and just for being myself.

And Finally, to the *Amazing God*.

Chapter 2, in full, is a reprint of the material ”Size effects and odd-even effects in MoS_2 nanosheets: first-principles studies” as it appears in Physical Chemistry Chemical Physics. Paul H. Joo, Jianli Cheng, Kesong Yang, 19, 29927-29933, 2017. The dissertation author was the primary investigator and author of this paper.

Chapter 4, in full, is currently being submitted for publication of the material ”Descriptors of Transition Metal Promoters on MoS_2 Nanocatalysts for Hydrodesulfurization: Binding Energy of Metal Sulfides from First Principles”. Paul H. Joo, Kesong Yang. The dissertation author is the primary investigator and author of this paper.

Chapter 5, in part, is a reprint of the material ”Energetic Stability, Oxidation States, and Electronic Structure of Bi-doped $NaTaO_3$: First-Principles Hybrid Functional Study” as it appears in Physical Chemistry Chemical Physics. Paul H. Joo, Maziar Behtash, Kesong Yang, 18,

857-865, 2016. The dissertation author is the primary investigator and author of this paper.

Chapter 6, in part, is a reprint of the material " Nip the Sodium Dendrites in the Bud on Planar Doped Graphene in Liquid/Gel Electrolytes". Xiaofei Hu, Paul Hyunggyu Joo, Huan Wang, Edward Matios, Chuanlong Wang, Jianmin Luo, Xuan Lu, Kesong Yang, and Weiyang Li. The dissertation author is the primary co-investigator and co-author of this paper.

VITA

2013	B. S. in Chemistry, McGill University
2015	M. S. in Chemical Engineering, University of California San Diego
2013-2019	Research Assistant, University Of California San Diego
2019	Ph. D. in Materials Science and Engineering, University of California San Diego

PUBLICATIONS

Paul H. Joo, Kesong Yang, “Effective Descriptor-Based Transition Metal Promotion Effects on MoS_2 Nanocatalysts for Hydrodesulfurization: First-Principles Studies”, *submitted*, 2019.

Xiaofei Hu, Paul H. Joo, Huan Wang, Edward Matios, Chuanlong Wang, Jianmin Luo, Xuan Lu, Kesong Yang, Weiyang Li, “Nip the Sodium Dendrites in the Bud on Planar Doped Graphene in Liquid/Gel Electrolytes”, *Adv. Funct. Mater.*, 1807974, 2019.

Paul H. Joo, Jianli Cheng, Kesong Yang, “Size effects and odd-even effects in MoS_2 nanosheets: first-principles studies”, *Phys. Chem. Chem. Phys.*, 19, 29927-29933, 2017.

Paul H. Joo, Maziar Behtash, Kesong Yang, “Energetic Stability, Oxidation States, and Electronic Structure of Bi-doped $NaTaO_3$: First-Principles Hybrid Functional Study”, *Phys. Chem. Chem. Phys.*, 18, 857-865, 2016.

ABSTRACT OF THE DISSERTATION

A First-Principles Investigation on Structural and Catalytic Properties of MoS_2 Nanocatalysts for Hydrodesulfurization

by

Paul Hyunggyu Joo

Doctor of Philosophy in Materials Science and Engineering

University of California San Diego, 2019

Professor Kesong Yang, Chair

MoS_2-based catalysts have been used in the petroleum industry for decades and it is of long-term interests to improve their catalytic efficiency in a hydrodesulfurization (HDS) process. Our focus is centered on studying the structural, thermochemical, and catalytic properties of the single-layer MoS_2 nanosheets, with an objective of generating the ideal HDS catalysts using first-principles calculations.

In the first project, we discovered the size and odd-even effects on the formation of sulfur vacancies in the triangular MoS_2 nanosheets. The S-terminated edges were found to be energetically more favorable than Mo-terminated edges. Two types of sulfur dimer vacancies

at the center (V_S@Cen) and the corner (V_S@Cnr) site of the S-terminated nanosheets revealed odd-even effects in the vacancies formation with respect to size.

In the second project, we introduce a new material called a monolayer Janus MoXY, which is a promising alternative to the MoS_2 catalyst. The Janus MoXY nanosheets can also be found in a triangular shape, exhibiting similar structural properties as MoS_2. For the enhancement of the catalytic activity, the ideal Gibbs free energy (ΔG_H) of hydrogen adsorption must be close to zero. Interestingly, our calculated ΔG_H also result in the similar odd-even effect in the hydrogen adsorption with respect to size.

In the third project, we report the transition metal (TM) promotion effects on the catalytic activity of S-terminated hexagonal MoS_2 nanosheets using 26 TM elements. The HDS activity of TM-promoted MoS_2 nanosheets is evaluated by modelling three consequent steps in an HDS process with a dibenzothiophene (DBT) molecule. The reaction energy of each steps were calculated with respect to the descriptor, binding energy (E_b) of TM sulfides. On the basis of the descriptor, several candidates including Co, Fe, and Cr are identified to be the ideal TM promoters.

In the fourth project, we examined the properties of Bi-doped $NaTaO_3$ for an additional application of photocatalytic water splitting . The Bi-doping sites were found to be dependent on the materials preparation conditions of $NaTaO_3$ and our results showed enhanced photocatalytic hydrogen evolution under visible light for Bi doping, simultaneously, at Na and Ta sites (Bi@(Na,Ta)).

In the fifth project, we theoretically investigated the affinity of Na atoms to B- and N-doped graphene substrates for the application of electrochemical energy storage. Compared to the pristine graphene, B- and N-doped graphene were found to possess different binding energies with the Na atoms with different doping forms.

Chapter 1

Introduction

1.1 Petrochemistry

Since the oil discovery in the Oil Creek Valley of Pennsylvania in 1859, petroleum has become a major industry in the United States.[6] The petroleum industry divides into three major sectors. First, the upstream sector involves the exploration of underground oil deposits to drill and bring up the crude oil and raw natural gas to the ground.[65, 43] Second, the midstream sector transports and stores the petroleum products *via* such as pipeline or oil tanker,[43] and lastly, the downstream sector refines and purifies the petroleum crude oil and the raw natural gas, respectively, and eventually reaches the consumers for use as fuels for transportation, paving roads, and electric generation, etc.[43] In the modern refining process, crude oil liquids and vapors break down into separate groups of hydrocarbon compounds (known as *fractions*), under atmospheric/vacuum distillation, depending on the boiling points and are converted into new petroleum products, such as gasoline and clean diesel fuels *via* several methods including cracking and catalytic processes.[28, 142] The variety of hydrocarbon compound groups mostly contains sulfur (S) and in fact, one of the major concerns during the refining process is the release of the elemental S into the atmosphere. Human activities have dominantly contributed to such excessive sulfur release through burning of the fossil fuels and industrial facilities. The release of sulfur into the air leads to the formation of sulfur dioxide (SO_2), which causes air pollution and SO_2 reacts with oxygen and other chemicals in the air to form sulfuric acids, eventually causing acid rain, as well.[43, 64] In recent years, the increasing energy consumption all over the world and strict environmental legislation that requires less than 10 ppm sulfur in transportation fuel, have resulted in a growing demand for ultra-low sulfur diesel.[122, 123, 124] As a result, the production of ultra clean diesel fuels has become a major challenge in the petroleum refinery industry, and this imminently requires the development of high-performance catalysts for deep desulfurization of diesel fuel.

1.2 Hydrodesulfurization

As one of the most important catalytic reactions in the petroleum refinery process, the hydrodesulfurization (HDS) plays a critical role in producing clean diesel fuel from the crude oil by removing sulfur and other contaminants.[71, 17, 5, 122, 123] As the demand for the ultra-low sulfur diesel is growing over decades[122, 123, 124], there have been many attempts to achieve and develop high-performance catalysts for deep HDS of diesel fuel. These HDS catalysts are mainly based on transition metal dichalcogenides, which exist in the form MX_2, where M represents a transition metal atom (Mo and W, etc.) and X represents a chalcogen atom (S, Se, or Te). For more than 70 years, transition metal sulfide (TMS) catalysts have been extensively studied and continuously applied in the petroleum industry.[71, 17, 5]. In the chemical process of HDS, the TMS catalyst under H_2 exposure generates sulfur vacancy sites, also known as the coordinatively unsaturated sites (CUSs), by the extrusion of H_2S, which occurs as H_2 dissociates to bond to the surface of the catalyst. The CUS plays a vital role in the reaction as it is recognized as the catalytically active site, because it attracts and adsorbs the S-containing crude oil compound. The CUS has been experimentally observed on the edges of the MoS_2 catalysts *via* scanning tunneling microscopy (STM)[45, 68, 129, 9]. The TMS catalyst then traps the elemental sulfur of the organic compound and leads to the breakage of the C-S bonds. Therefore, S is removed from the organic compound and refills the CUS of the catalyst. This is also known as the direct desulfurization pathway.[11, 112, 129]

1.3 Molybdenum Disulfide (MoS_2)

As mentioned in the previous section, a transition metal dichalcogenide consists of one transition metal atom and two chalcogen atoms, in the stoichiometric ratio. More specifically, the two chalcogen atoms are chemically bonded to the transition metal atom from top and bottom. This is considered as a monolayer of MX_2. In the bulk structure, each layer of MX_2 are bonded by weak van der Waals forces.

One of the most extensively studied 2D TMS catalyst in the petrochemistry is molybdenum disulfide (MoS_2).[95, 23, 38] MoS_2 is known as the next generation of graphene, since it overcomes the limitation of graphene, such as its lack of band gap and its incapability as a catalyst. However, in order for MoS_2 to work in various applications, including photovoltaics, transistors, and especially the enhancement of catalytic reactions (HDS), it must be converted from its bulk structure into few- or single-layer nanosheets,[113, 100, 17, 5] In fact, the bulk MoS_2 is not a good candidate for catalytic activity. Some common experimental methods of such conversion have already been revealed, including chemical vapor deposition (CVD), chemical exfoliation, and mechanical exfoliation. The CVD method requires high temperature to grow single-layer MoS_2 from $MoCl_5$, elemental S, and SnS_2,[106, 145] the chemical exfoliation method involves the intercalation of Li in the van der Waals gap between each MoS_2 layer for separation,[89, 146] and finally, the mechanical exfoliation method simply uses an adhesive tape to be pressed and peel off the layers from the bulk MoS_2.[59, 88]

A wide range of further experimental techniques have been employed to characterize the microstructures/nanostructures and catalytic properties of the single-layer MoS_2-based catalysts,[144, 127, 94, 37, 67, 68, 129] such as M*ö*ssbauer spectroscopy,[144, 127] laser Raman spectroscopy,[94] and scanning tunneling microscopy (STM).[37, 67, 68, 129] It has been a long-time standing issue to address the detailed edge structures of unpromoted and promoted MoS_2 due to the limitation of atomic resolution structural characterization.[5] A milestone in the microstructure characterization is the identification of Co-Mo-S structures in the MoS_2-based catalysts.[144, 127] It was found that Co-Mo-S catalysts exhibit small MoS_2-like-nanocrystal structures, with the promoter atoms (Co) at the edges of MoS_2 layers (and also in the same plane with Mo atoms). Later research studies suggest that the coordinatively unsaturated sites (CUS) formed by sulfur vacancies on the edges of MoS_2 are active catalytic sites, and accordingly the role of promoter Co (Ni) atoms can be interpreted to optimize the catalytic activity of MoS_2 by increasing the number of active catalytic sites, *i.e.*, sulfur vacancies.[45, 68, 129, 9] Accordingly, sulfur vacancies at the edges are considered as a key descriptor to evaluate the catalytic activity of MoS_2-based catalysts.

Depending on the its growth conditions, the single-layer MoS_2 exists in multiple shapes.[12, 129, 9] The shape undergoes an evolution from dodecagonal to hexagonal, and to triangular from sulfur-poor to sulfur-rich growth conditions.[12, 143] Under sulfur-rich condition, Lauritsen *et al.* successfully observed a triangular MoS_2 nanocluster using Scanning Tunneling Microscopy (STM) and classified the nanoclusters with respect to size.[68] Shi *et al.* also observed well-defined triangular MoS_2 layers that were prepared using a chemical vapor deposition (CVD) method.[116] Under sulfur-poor condition, Co-Mo-S structures were found in a hexagonal shape *via* an STM analysis.[5] Tuxen *et al.* found that Co promotion on the MoS_2 nanoclusters lead to a hexagonal nanocluster under the HDS environment.[130]

1.4 Catalytic Efficiency

For several decades, there have been many attempts to improve the catalytic efficiency of the MoS_2 catalysts. The ways to improve such efficiency share one common factor, which is the increase in the amount of active catalytic site on the surface of the catalyst. In order to achieve the inflation of the active sites, the MoS_2 catalysts must exist under the condition of large surface exposure. For instance, Deepak *et al.* was able to obtain a structure of largely surface-exposed MoS_2 nanotubes and successfully achieved a HDS reaction, converting a S-containing dibenzothiophene (DBT) molecule to biphenyl (BP) with an efficiency of approximately 19%.[21] The synthesis of Co_3S_4@MoS_2 heterostructures was also found to enhance the hydrogen evolution reaction (HER) activity, possible due to the abundant electrochemical surfaces and modulated coordinations.[33] The active catalytic sites can also be increased by the promotion of the edges of the MoS_2 nanosheet by transition metals (TM).[102] The TM promotion is known to enhance the opening of the active sites and thus, aids in the attraction of the organic compounds for the HDS reaction. This will be discussed in more details in Chapter 3.

1.5 Additional Energy Renewables

In addition to petrochemistry, the worldwide energy and environmental concerns are also growing demands in other clean energy systems, such as the clean renewable sources and storages. One promising way of harvesting clean and sustainable energy is by the photocatalytic generation of hydrogen using semiconductor photocatalysts. This requires high solar-to-hydrogen efficiency with visible-light-driven photocatalysts.[39, 16, 136, 92, 13, 131] As photocatalysis contributes only 4% to hydrogen production worldwide, compared to 48% of natural gas steam reforming, 30% of oil-based, and 18% coal gasification,[132] it is in critical need to develop and improve highly efficient ways to generate hydrogen by photocatalysis. Thus, photocatalytic semiconducting materials have been gaining an increasing amount of interests because of their potential applications for highly efficient hydrogen generation *via* water splitting. Photocatalytic water splitting is a chemical reaction that produces $2H_2$ and O2 from the decomposition of $2H_2O$, initiated by the absorbance of light (hν). Specifically, the absorbance of light causes excitation of electrons from the valence band (VB) to the conduction band (CB) of the catalyst, leaving a hole with a positive charge in VB that leads to the oxidation of H_2O to O_2 and reduction of H^+ to H_2 in CB.[30] For a successful water splitting, the minimum band gap at pH = 0 is 1.23 eV,[46, 120] which corresponds to approximately 1008 nm in the infrared light region. Perovskite oxide semiconductors (ABO_3) have been receiving tremendous amount of attention because of their capability of increasing the efficiency of the photocatalytic water splitting and environmental friendliness.[57, 74, 141, 36, 148, 40, 26, 76, 55, 158, 159, 73, 42, 75, 157, 103, 53, 55, 138, 84] Chapter 4 will discuss on one promising perovskite oxide semiconductor candidate, sodium tantalate ($NaTaO_3$), in details.

Sodium (Na) is one of the most promising alternatives to lithium (Li) for the cost-effective electrochemical energy storage systems.[80, 2] However, one major challenge with the Na metal is its severe dendritic growth at high current densities.[110] Therefore, a detailed examination of the Na nucleation mechanism in different electrolyte systems is necessary. Chapter 5 will discuss the Na nucleation mechanism on boron (B)- and nitrogen (N)-doped graphene substrates for stablizing Na metal batteries, using first-principles calculations.

Chapter 2

Size effects and odd-even effects in MoS_2 nanosheets: first-principles studies

As outlined in Chapter 1, molybdenum disulfide (MoS_2) nanostructures have been widely used as catalysts in the petroleum refinery industry for the HDS process, in which sulfur vacancies play a critical role in determining the catalytic activity. In this chapter, we report size effects and oddeven effects on the formation of sulfur vacancies in the triangular MoS_2 nanosheets using first-principles calculations. By modeling four types of edge structures of MoS_2 nanosheets, S-terminated edges are found to be energetically more favorable than Mo-terminated edges, and are then selected for studying energetics of sulfur vacancies. Two types of sulfur dimer vacancies at the center (V_S@Cen) and at the corner (V_S@Cnr) of the edges of S-terminated MoS_2 nanosheets are modeled, respectively. Our results reveal a strong odd-even effect on the formation of sulfur dimer vacancies, particularly for small MoS_2 nanosheets, in terms of the size of nanosheets that is defined by the number of Mo atoms on the edge. The V_S@Cen dimer vacancy has a low formation energy at an even-number but a high formation energy at an odd-number, while the V_S@Cnr dimer vacancy exhibits a complete opposite trend. These results indicate that small MoS_2 nanosheets can exhibit unique material properties for catalytic applications.

2.1 Introduction

As mentioned in Chapter 1, MoS_2 is one of the most extensively studied TMS catalyst in the petroleum refinery. MoS_2 stabilizes as single layers in the catalytic environment[17, 5] and the single-layer MoS_2 nanostructures could exist in multiple shapes, depending on the materials growth conditions.[37, 67, 45, 129, 68, 9, 12] For instance, Besenbacher's team reported the first real-space STM images of single-layer MoS_2 nanoparticles and observed their triangular shapes under the sulfiding conditions.[37, 67] After that, more and more experimental STM images confirmed the formation of the triangular MoS_2 nanocrystal under the sulfur-rich growth condition.[68, 45, 129, 9] In the computational/theoretical side, density functional theory calculations demonstrated that the shape of MoS_2 nanoparticles is strongly dependent on the sulfiding conditions: a high chemical potential of sulfur leads to triangular shape of MoS_2 and a low chemical potential of sulfur is likely to lead to a (deformed) hexagon.[108] Moreover, a recent first-principles computational study demonstrates a shape evolution of monolayer MoS_2 from the dodecagonal shape, to the hexagonal shape, and to the triangular shape with the variation of the chemical potential of sulfur from sulfur-poor to sulfur-rich condition.[12]

In addition to the structural evolution of MoS_2 nanosheets under various types of sulfiding conditions, atom-resolved STM studies also revealed that the triangular MoS_2 nanocrystals may exhibit a structural progression as a function of their size, and there might exist some certain energetically favored “magic” nanoclusters.[68] More interestingly, Besenbacher's team found that the location of the sulfur vacancies is sensitive to the size of the MoS_2 nanoclusters.[129] Their statistical analysis indicated that many sulfur vacancies appear at the MoS_2 nanoclusters with size $n = 5$ and 8 (n refers to the number of Mo atoms along the edge of the triangular MoS_2 cluster). They also found that for the small cluster with $n = 5$, the sulfur vacancy tends to form at the corner rather than at the center of the edge, while for the large cluster with $n = 8$, the behavior seems to be opposite. This finding implies that the catalytic activity of MoS_2 nanosheets may show a strong size effect and even an odd-even effect (the nanoclusters with an odd and even size number exhibit different or even opposite property). Despite of these important experimental findings, a detailed atomistic understanding into such effects is not fully elucidated yet and a computational and theoretical study of the structural and energetic evolution as a function of the cluster size is necessary.

In Chapter 2, by using first-principles density functional theory calculations, we studied the structural and energetic evolution of MoS_2 nanosheet (without and with sulfur dimer vacancies on the edges) as a function of its size that is defined by the number of Mo atoms on the edge. Our results clearly indicate a strong odd-even effect on the formation of the sulfur vacancies in the S-terminated MoS_2 nanosheets, implying that nanostructured MoS_2 may exhibit unique catalytic properties. Lastly, a potential alternative for the MoS_2 nanosheet is introduced.

2.2 Computational and Structural Details

First-principles density functional theory (DFT) electronic structure calculations were carried out using Vienna Ab-initio Simulation Package (VASP).[63, 60] The Projector-Augmented Wave (PAW) potential was employed to treat electron-ion interactions and the Generalized Gradient Approximation (GGA) parameterized by Perdew-Burke-Ernzerhof (PBE) was used for electron exchange-correlation functional.[7, 96] The cut-off energy of 340 eV for the plane-wave basis set and the single Γ point were used in our calculations. All the atomic positions of the MoS_2 nanosheets were relaxed until all components of the residual forces were less than 0.02 eV/Å. The convergence tolerance for the self-consistent-field iteration was set to 10^{-5} eV.

The bulk crystal structure of molybdenum disulfide, at room temperature is, hexagonal (space group no. 194, $P6_3/mmc$) with experimental lattice constant a = 3.15 Å and c = 12.3 Å.[134] Our calculated equilibrium lattice parameters within the GGA-PBE framework are a = 3.18 Å and c = 13.4 Å, which is in a good agreement with the experimental value. In this

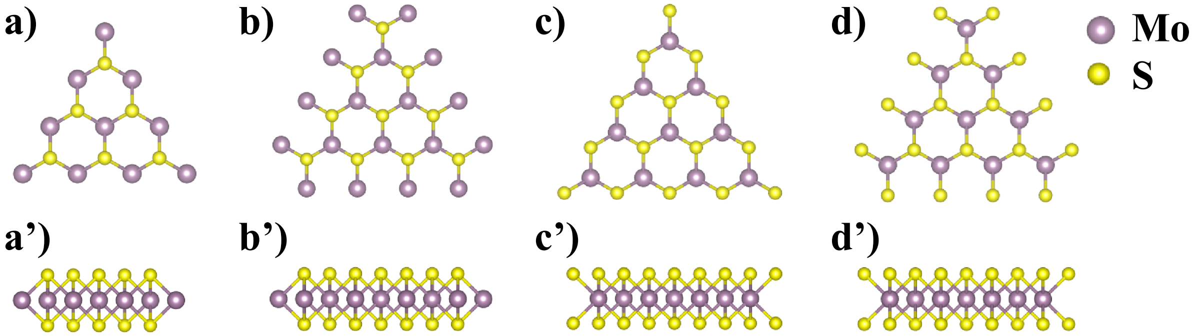

Figure 2.1: Single-layer MoS_2 nanosheets (n = 4) with zig-zag patterned edges from top view (a-d) and side view (a'-d'), respectively. (a, a') ZZ-Mo1, (b, b') ZZ-Mo2, (c, c') ZZ-S1, and (d, d') ZZ-S2. The large purple and small yellow balls represent Mo and S atoms, respectively. The size of the nanosheet (n) is indicated by the number of Mo atoms in the edge of the MoS_2 nanosheet.

work, we modeled four types of MoS_2 edge structures with a zig-zag pattern, including two Mo-terminated (defined as ZZ-Mo1 and ZZ-Mo2) and two S-terminated (defined as ZZ-S1 and ZZ-S2) edges, respectively, shown in Figure 2.1.

The size of the MoS_2 nanosheet is defined by the number of Mo atoms on each edge, indicated by a variable n. For example, all four types of nanosheets in Figure 2.1 have a size number of n = 4. In the ZZ-Mo1 structure (see Figure 2.1a), each Mo atom on the edge is coordinately bonded to two adjacent S dimers, and all the S dimers are trapped within the triangle framed by the Mo atoms. In the ZZ-Mo2 structure (see Figure 2.1b), Mo atoms on the edges are protruded externally in a perpendicular direction of the triangular nanosheet, and the protruded Mo atoms are each bonded to a S dimer located in the inner frame. These S dimers also form a zig-zag pattern on the each side of the triangle. The nanosheets with S-terminated edges, *i.e.*, ZZ-S1 and ZZ-S2 structures, are similar to those with Mo-terminated edges, but with Mo and S atoms switched in each position from top view, see Figure 2.1c and 2.1d. However, it is worth mentioning that, at the same size n, the ZZ-Mo1 (ZZ-Mo2) does not share the same total number of atoms with the ZZ-S1 (ZZ-S2) since the Mo-atom layer is stacked between two S-atom layers, see Figure 2.1a'-d'.

2.3 Results and Discussion

2.3.1 MoS$_2$ Nanosheets

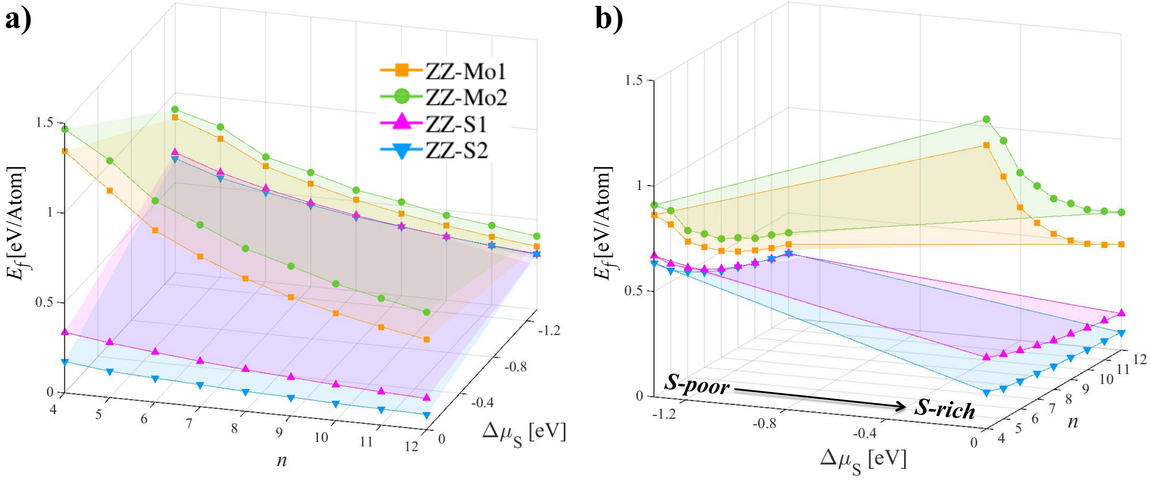

Figure 2.2: Calculated formation energies of ZZ-Mo1, ZZ-Mo2, and ZZ-S1, and ZZ-S2 nanosheets with respect to the size (*n*) and chemical potential of sulfur ($\Delta\mu_S$), plotted from viewing angle of a) size, *n* and b) $\Delta\mu_S$.

To evaluate the structural stability of the triangular MoS$_2$ nanosheets, we calculated their formation energies. The formation energy per atom for the MoS$_2$ nanosheets, with a formula of Mo$_x$S$_y$, was calculated using the equation,

$$E_f = [E_{Mo_xS_y} - x\mu_{Mo} - y\mu_S]/(x+y) \tag{2.1}$$

where $E_{Mo_xS_y}$ is the total energy of the MoS$_2$ nanosheet, μ_{Mo} and μ_S are chemical potentials of Mo and S atoms, and x and y are the number of Mo and S atoms, respectively. μ_S and μ_{Mo} are not fixed but dependent on the growth condition of MoS$_2$ nanosheets, and they are linked by the stability of MoS$_2$ phase:

$$\mu_{Mo} + 2\mu_S = E_{MoS_2} \tag{2.2}$$

where E_{MoS_2} is the total energy of bulk MoS$_2$ per formula unit. Accordingly, eq. 2.1 can also be rewritten as:

$$E_f = [E_{Mo_xS_y} - xE_{MoS_2} + (2x - y)\mu_S]/(x + y) \tag{2.3}$$

Under extremely S-rich (Mo-poor) condition, μ_S can be obtained from the total energy per atom for the bulk S system, *i.e.*, E_S, and μ_{Mo} can be calculated from the MoS_2 growth condition. Under extremely Mo-rich (S-poor) condition, μ_{Mo} can be obtained from the total energy per atom for the bulk Mo metal, *i.e.*, E_{Mo}, and μ_S can be calculated from the MoS_2 growth condition.

For convenient discussion, herein we define reference chemical potential of S ($\Delta\mu_S$) and Mo ($\Delta\mu_{Mo}$) using the following equations:

$$\Delta\mu_{Mo} = E_{Mo} - \mu_{Mo} \tag{2.4}$$

$$\Delta\mu_S = E_S - \mu_S \tag{2.5}$$

The extremely S-rich condition is characterized by $\Delta\mu_S = 0$, that is, μ_S = E_S, while the extremely Mo-rich condition is characterized by $\Delta\mu_{Mo} = 0$, that is, μ_{Mo} = E_{Mo}. The formation enthalpy of MoS_2 is defined as:

$$\Delta H(MoS_2) = E_{MoS_2} - E_{Mo} - 2E_S. \tag{2.6}$$

By using above definitions, the formation enthalpy of MoS_2 can also be rewritten as:

$$\Delta H(MoS_2) = \Delta\mu_{Mo} + 2\Delta\mu_S \tag{2.7}$$

To have a reference of evaluating the stability of MoS_2 nanosheet, we first calculated the formation enthalpy of bulk MoS_2. Our calculated formation enthalpy for bulk MoS_2 is 2.63 eV/atom, which is in a good agreement with a prior theoretical value of 2.64 eV/atom.[119, 12] These calculated values are consistent with the experimental value of 2.82 eV/atom.[90]

The calculated formation energies of the four types of nanosheet structures, ZZ-Mo1, ZZ-Mo2, ZZ-S1, and ZZ-S2, as a function with the reference chemical potential of S, $\Delta\mu_S$, and nanosheet size, n, are plotted in Figure 4.4. To clearly visualize the trend of the formation energy, the figures are plotted from the viewing angle of $\Delta\mu_S$ (Figure 4.4a) and n (Figure 4.4b), respectively. Our calculations reveal the following trends:

(i) As the size of MoS_2 nanosheet (n) increases, the formation energy of all the four types of MoS_2 nanosheets decreases, indicating that larger MoS_2 nanosheets are energetically more favorable to form, see Figure 4.4a. Moreover, the formation energy of Mo-terminated nanosheets (ZZ-Mo1 and ZZ-Mo2) decrease much faster than that of S-terminated nanosheets (ZZ-S1 and ZZ-S2). This can be rationalized from two different perspectives: a) atomic ratio between the number of S and Mo atoms (N_S/N_{Mo}), and b) atomic ratio between the number of atoms on the edge and total atoms (N_{Edge}/N_{Total}), see Figure 2.3 and 2.4. The atoms on the edge are not fully coordinated and thus have dangling bonds.

Regarding the first perspective, as n increases, for ZZ-Mo1 (ZZ-Mo2) nanosheet, N_S/N_{Mo} increases from 1.2 (1.11) to 1.69 (1.53), and for ZZ-S1 (ZZ-S2) nanosheets, N_S/N_{Mo} decreases from 3.0 (3.6) to 2.33 (2.62). As n reaches infinite, both reaches to stoichiometric atomic ratio of 2.0 in the bulk MoS_2. About the second perspective, as n increases, the atomic ratio N_{Edge}/N_{Total} decrease. In other words, the relative number of uncoordinated (rigorously speaking, not fully coordinated) atoms decreases, and thus the formation energy decreases as n increases. Although the two atomic ratios, N_S/N_{Mo} and N_{Edge}/N_{Total}, have different meaning, they are strongly correlated. This is because as N_{Edge}/N_{Total} decreases, N_S/N_{Mo} naturally tends close to 2.0. These findings highlight direct relationships between the atomic ratios (N_S/N_{Mo} and N_{Edge}/N_{Total}) and energetic stability of MoS_2 nanosheets with respect to the size.

(ii) The S-terminated nanosheets (ZZ-S1 and ZZ-S2) have lower formation energies than Mo-terminated ones (ZZ-Mo1 and ZZ-Mo2) in the whole range of the $\Delta\mu_S$, and they have maximum formation energy difference under the S-rich condition. This indicates that S-terminated nanosheets can be prepared energetically more favorably than Mo-terminated ones.

This conclusion is well consistent with the prior experimental studies,[68, 129, 9, 66] in which the majority of the triangular nanosheets were found to be S-terminated edge structures (ZZ-S1 and/or ZZ-S2) under the S-rich condition.

(iii) The ZZ-S2 models are energetically more favorable to form than ZZ-S1 structures for most range of $\Delta\mu_S$, though they tend to have similar formation energies under extremely S-poor condition. This conclusion is well consistent with one recent experiment in which 95% of the observed MoS_2 triangular nanosheets exhibit ZZ-S2 structure.[9]

(iv) As $\Delta\mu_S$ increase, *i.e.*, from S-poor to S-rich condition, the formation energies of the two Mo-terminated nanosheets (ZZ-Mo1 and ZZ-Mo2) increase, while those of the two S-terminated nanosheets (ZZ-S1 and ZZ-S2) decrease. This indicates that the S-terminated nanosheets tend to form under S-rich condition.

(v) Under S-rich growth condition, the formation energies of the four types of nanosheets lie within a wide range for all studied size. Their formation energies follow the order: ZZ-Mo2 $>$ ZZ-Mo1 $>$ ZZ-S1 $>$ ZZ-S2. Under S-poor growth condition, the formation energies of the four types of nanosheets lie within a narrow range, indicating that they are energetically comparable. The calculated formation energies decrease in the order: ZZ-Mo2 $>$ ZZ-Mo1 $>$ ZZ-S1 $>$ ZZ-S2, and they tend to converge as n increases. For example, the formation energy of ZZ-S1 and ZZ-S2 nanosheets converge at $n \geq 8$. However, the formation energy of these two types of structures under S-poor condition are much larger than that under S-rich condition, implying that S-terminated nanosheets is unlikely to be formed under S-poor condition. Actually, MoS_2 nanosheets in triangular shape have not been experimentally found under S-poor growth conditions.[12, 8, 129]

2.3.2 Sulfur Vacancies

Next, we studied the size effects on the formation of sulfur vacancies on the edges of MoS_2 triangle nanosheet. As discussed above, ZZ-S2 nanosheets are energetically more favorable

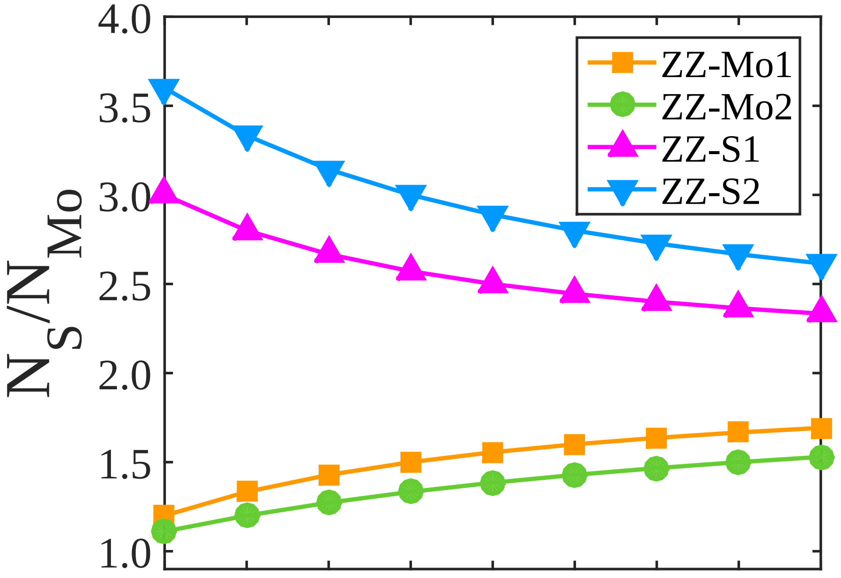

Figure 2.3: Atomic ratio between the number of S and Mo atoms (N_S/N_{Mo}) as a function of the size of the MoS_2 nanosheets, *n*.

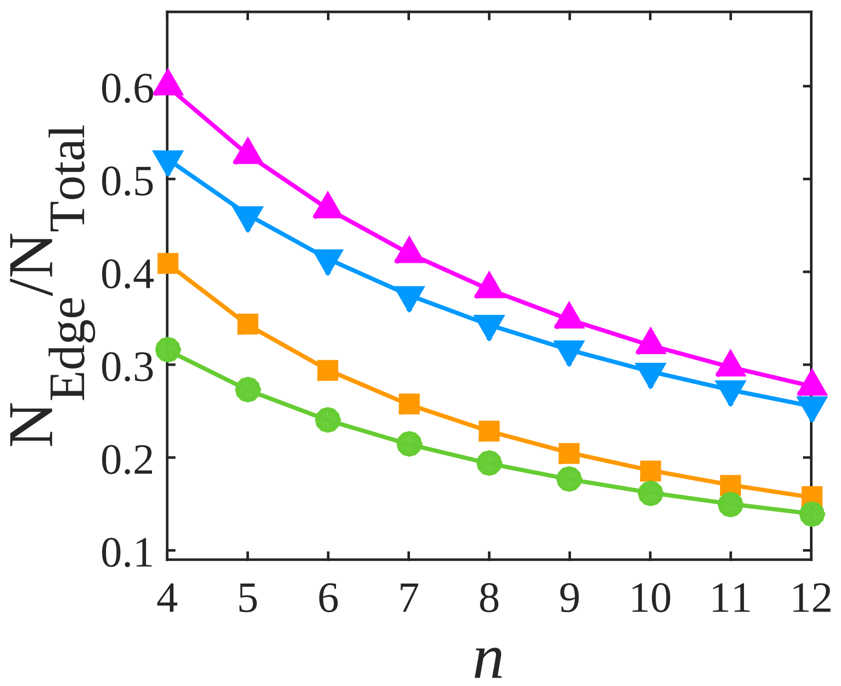

Figure 2.4: Atomic ratio between the number of atoms on the edge and total atoms (N_{Edge}/N_{Total}) as a function of the size of the MoS_2 nanosheets, *n*.

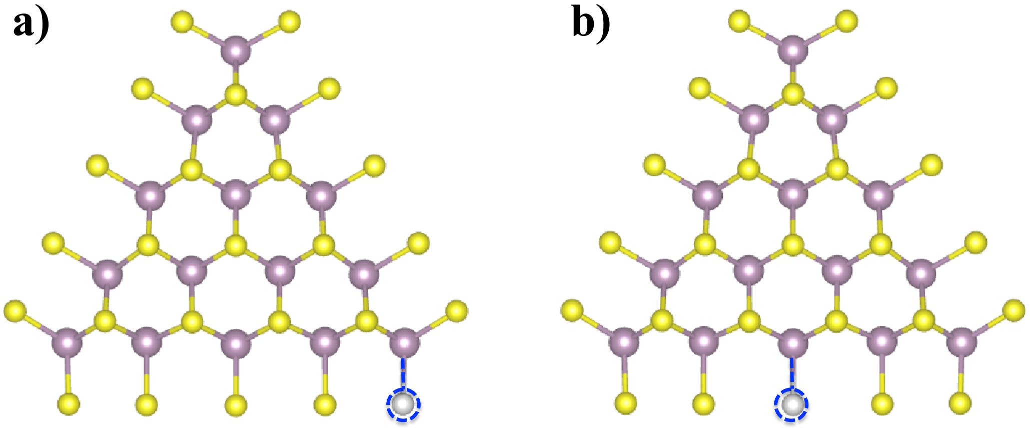

Figure 2.5: Geometrical structures of ZZ-S2 MoS_2 nanosheet (n = 5) with sulfur dimer vacancy at (a) corner site (V_S@Cnr) and (b) at center site (V_S@Cen) on the edge. The gray spheres with blue dash circles represent the sulfur vacancies.

than the ZZ-S1 and Mo-terminated nanosheets. Hence, herein we focus on the ZZ-S2 MoS_2 nanosheet, and consider two types of sulfur vacancies on the edge, *i.e.*, sulfur vacancy at corner (V_S@Cnr) and at center (V_S@Cen), respectively. It is important to note that there are two layers of S atoms that lie above and below the Mo-atom layer, respectively, forming a symmetrical sandwich-like structure with middle Mo-atom layer as symmetry plane, see Figure 2.1d'. As a result, in principle, the two sulfur vacancies on the top and bottom S-layer share the same formation probability. Actually, such a sulfur dimer vacancy has been experimentally confirmed through STM images.[68, 129] Therefore, in this work, we modeled the sulfur dimer vacancy by removing two symmetrical S atoms simultaneously from the relaxed MoS_2 nanosheet. As an example, the geometrical structures of these two types of sulfur dimer vacancies, *i.e.*, V_S@Cnr and V_S@Cen, in the n = 5 ZZ-S2 nanosheet, are shown in Figure 2.5a and b, respectively. We calculated the formation energy of a sulfur dimer vacancy using the equation:

$$E_f = E_{Mo_xS_{y-2}} - E_{Mo_xS_y} + 2\mu_S \tag{2.8}$$

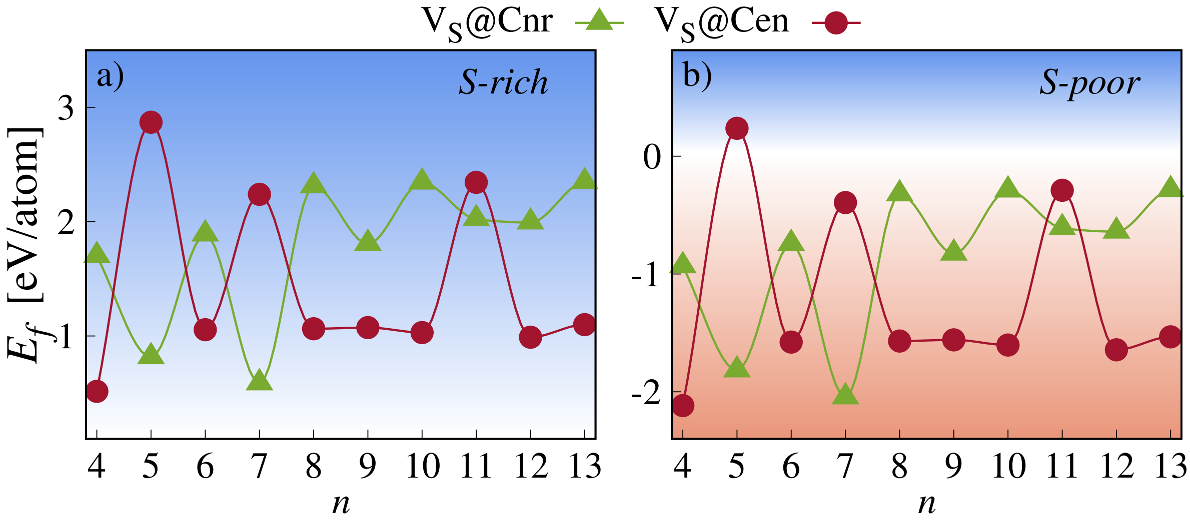

Figure 2.6: Calculated formation energy (E_f) of ZZ-S2 MoS_2 nanosheet with sulfur dimer vacancy as a function of the size (n) of the nanosheets under the a) S-rich and b) S-poor conditions, respectively. Blue line with triangular points represent V_S@Cnr and red line with circular points represent V_S@Cen.

where $E_{Mo_xS_{y-2}}$ is the total energy of a MoS_2 nanosheet with one sulfur dimer vacancy, $E_{Mo_xS_y}$ is the total energy of a MoS_2 nanosheet without sulfur dimer vacancy, and x and y are the number of Mo and S atoms, respectively. The calculated formation energy of a sulfur dimer vacancy in the ZZ-S2 MoS_2 nanosheets with different sizes (n = 4-13) is shown in Figure 2.6. Figure 2.6a and 2.6b show the E_f under the extremely sulfur-rich and sulfur-poor conditions, respectively. The following trends can be found:

(i) The calculated E_f under the S-rich and S-poor conditions both have the same pattern, and as expected, E_f under the S-poor condition is much lower than that under the S-rich condition.

(ii) At $4 \leq n \leq 8$, *i.e.*, for small MoS_2 nanosheets, the V_S@Cen dimer vacancy has a low formation energy for even-number size but high formation energy for odd-number size, while the V_S@Cnr dimer vacancy has a complete opposite trend. These results indicate a strong odd-even effect in the formation of sulfur vacancies in the small MoS_2 nanosheets and the energetic preference for the location of sulfur dimer vacancies. For instance, at n = 5, V_S@Cnr has a much lower formation energy than that of V_S@Cen, implying that the sulfur dimer vacancy tends to

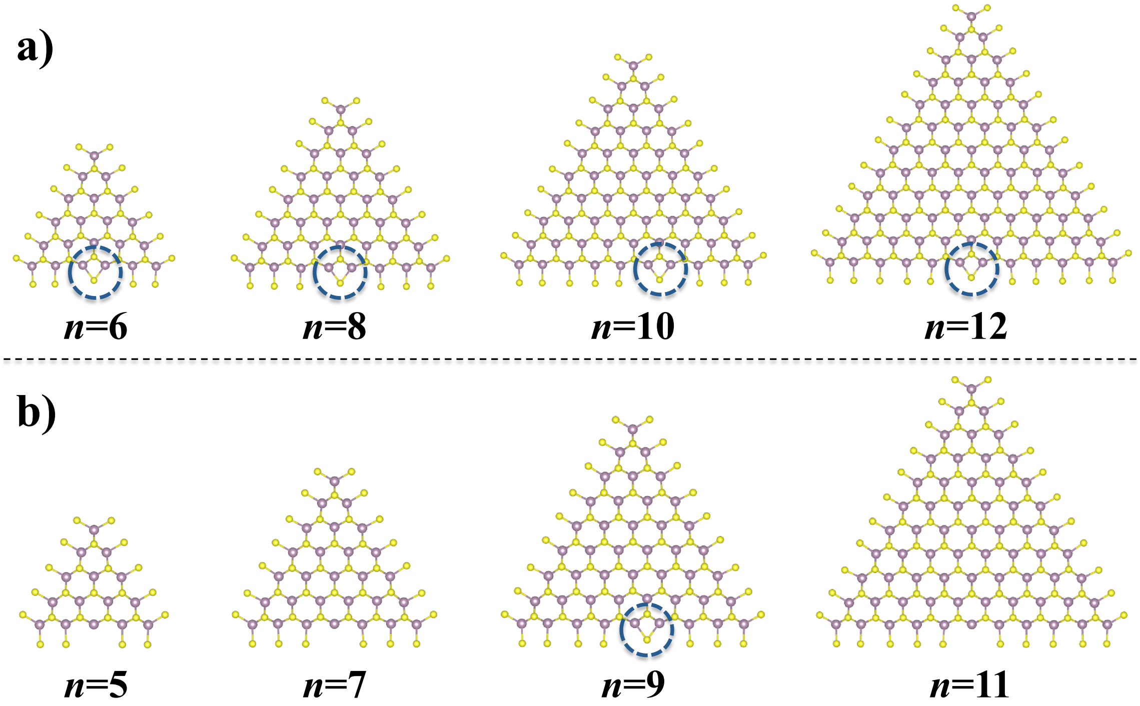

Figure 2.7: Geometrical structures of the relaxed MoS_2 nanosheet with sulfur vacancy at the center of the edge (V_S@Cen) for a) even-number size (n = 6, 8, 10, and 12) and b) odd-number size (n = 5, 7, 9, and 11). The new formed S-Mo bonds between the coordinatively unsaturated sites (Mo atoms with dangling bonds) and its adjacent S dimer are highlighted by the blue circle.

form at a corner site. It is worth mentioning that this result is well consistent with the experimental findings from STM images.[129] In the experiment,[129] it is found that for n = 5 nanosheet, the probability of formation of the corner vacancies (V_S@Cnr) is much higher than that of center vacancies (V_S@Cen). More interestingly, for n = 8 nanosheet, the experimental STM images reveal an opposite phenomenon, *i.e.*, high probability of formation of the center vacancies than that of the corner vacancies, which is in an excellent agreement with our computational finding.

(iii) At $9 \leq n \leq 13$, *i.e.*, for relatively large MoS_2 nanosheets, the two types of dimer vacancies basically follow the same trend with that at $4 \leq n \leq 8$, but the odd-even effect becomes relatively weak. For instance, V_S@Cnr has a comparable formation energy at n = 12 and at n = 11, and V_S@Cen has a relatively low and comparable formation energy at n = 9 and at n = 10.

(iv) For V_S@Cnr dimer vacancy, as n increases, its formation energy at $9 \leq n \leq 13$ is

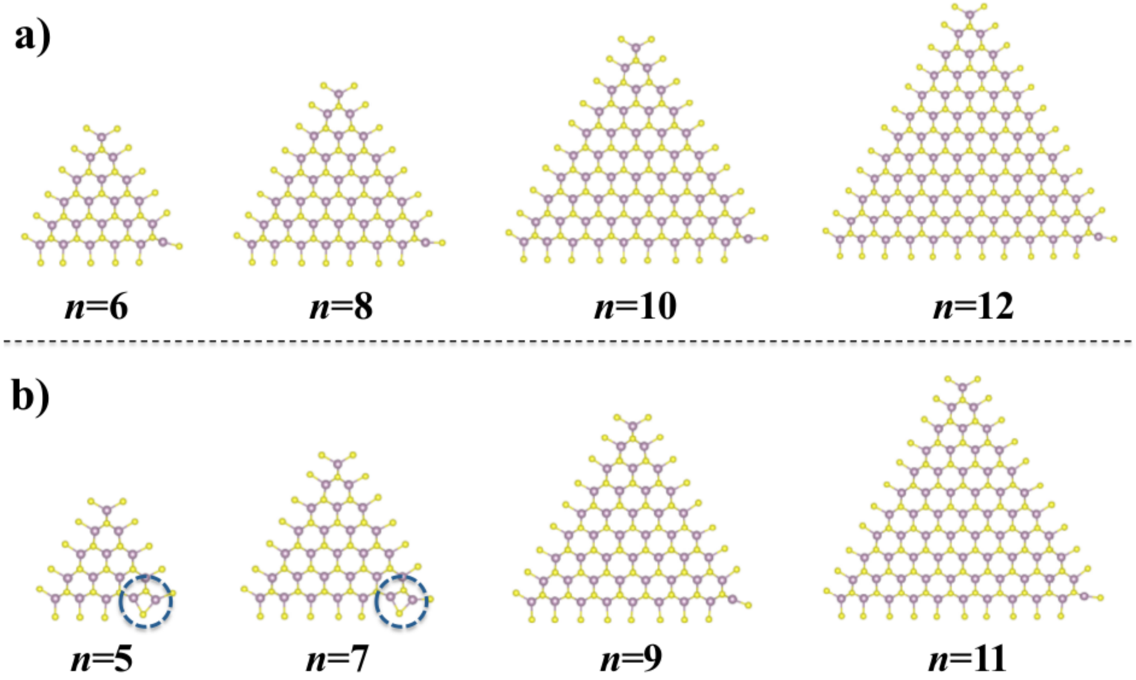

Figure 2.8: Geometrical structures of the relaxed MoS_2 nanosheet with sulfur vacancy at the corner of the edge (V_S@Cnr) for a) even-number size (n = 6, 8, 10, and 12) and b) odd-number size (n = 5, 7, 9, and 11). The new formed S-Mo bonds between the coordinatively unsaturated sites (Mo atoms with dangling bonds) and its adjacent S dimer are highlighted by the blue circle.

generally larger than that at $4 \leq n \leq 8$. This indicates that the V_S@Cnr dimer vacancies tend to be formed in the small MoS_2 nanosheets.

(v) For V_S@Cen dimer vacancy, at $n = 4$, the V_S@Cen dimer vacancy has a much low formation energy. At $n \geq 6$, its formation energy for n = 6, 8, 10, and 12 is almost unchanged. Unlike the case of V_S@Cnr dimer vacancy, these results indicate that V_S@Cen dimer vacancy does not have a strong energetic preference to form in terms of the size of the nanosheet.

The microscopic mechanism of the odd-even effects on the formation energy of the sulfur dimer vacancy is strongly associated with the geometrical properties of MoS_2 nanosheets, including the triangular shape and the number of atoms on the edge. In particular, the relaxed geometrical structures can clearly reveal the odd-even pattern.

The geometrical structures of MoS_2 nanosheets with sizes n = 5-12 for V_S@Cen and

V_S@Cnr dimer vacancy are shown in Figure 2.7 and 2.8, repectively. The relatively lower formation energy of MoS_2 nanosheet results from the interaction between the coordinatively unsaturated site (CUS) (the Mo sites with dangling bonds caused by the sulfur dimer vacancy) and the adjacent sulfur dimer. If the sulfur dimer moves towards the CUS and forms new S-Mo bonds with the CUS, then the MoS_2 nanosheets will reach a new equilibrium state with lower formation energy, see Figure 2.7a (n = 6, 8, 10, and 12) and Figure 2.8b (n = 5 and 7). If the sulfur dimer does not move towards the CUS and the CUS remains unsaturated, then the MoS_2 nanosheets have a relatively high formation energy, see Figure 2.7b (n = 5, 7, and 11) and Figure 2.8a (n = 6, 8, 10, and 12).

The reason for the displacement of sulfur dimer can be further explained as following. For the MoS_2 nanosheets with even-number size (n = 6, 8, 10, and 12), the introduction of one V_S@Cen dimer vacancy leads to an odd number of sulfur dimers on the edge. As a result, the sulfur dimer in the center tends to be shared by the two Mo atoms in the center, saturating the CUS (*i.e.*, Mo atom with dangling bonds) and thus forming a stable edge structure. For the MoS_2 nanosheets with odd-number size (n = 5, 7, and 11), the introduction of one V_S@Cen dimer vacancy leads to an even number of sulfur dimers on the edge, which are uniformly separated by the V_S@Cen dimer vacancy. Accordingly, the sulfur dimers on each side (separated by the vacancy) reach an equilibrium state by keeping CUS unsaturated, resulting in a relatively high formation energy. An exception occurs for n = 9, in which the sulfur dimer on the right side saturates the CUS and leads to a relatively low formation energy.

On the basis of the odd-even effects in the formation of sulfur vacancy, one can speculate that there should also exist odd-even effects in the HDS reaction on the MoS_2 nanosheet since this reaction involves the sulfur edge vacancies.[129, 9, 128, 93] In this process, the sulfur edge vacancies and by products, H_2S, are formed upon the H_2 dissociation and reactions with sulfur edge atoms on the MoS_2 nanosheets. Figure 4.7 shows the scheme of the HDS reaction on the MoS_2 nanosheet. Here we show one example application of the odd-even effects in evaluating

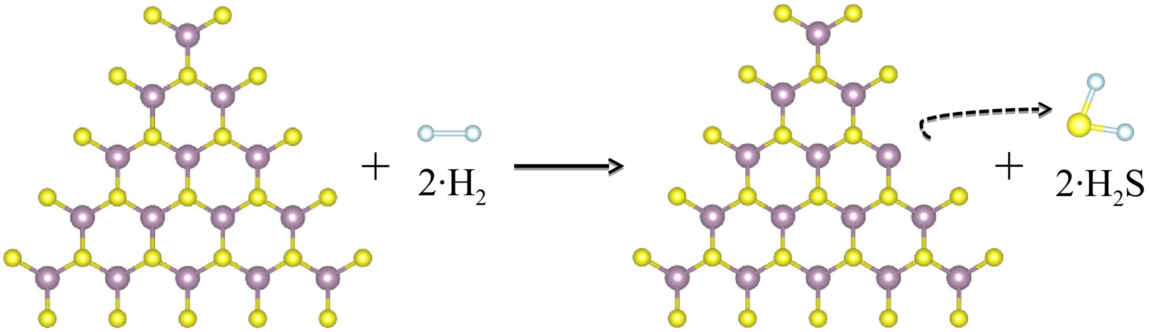

Figure 2.9: Scheme of the HDS reaction on the ZZ-S2 type MoS_2 nanosheet. One sulfur dimer reacts with two H_2, forming one dimer sulfur vacancy and two H_2S molecules.

the HDS reaction energy (ΔE_r) using below equation:

$$\Delta E_r = (E_{Mo_xS_{y-2}} + 2E_{H_2S}) - (E_{Mo_xS_y} + 2E_{H_2}) \tag{2.9}$$

where E_{H_2S} and E_{H_2} refer to the total energy of H_2S and H_2 molecules, respectively. By combining eq. 2.8 and 2.9, we have:

$$\Delta E_r = E_f - 2(\mu_S + E_{H_2} - E_{H_2S}) \tag{2.10}$$

which indicates that the HDS reaction energy ΔE_r is always less than the formation energy of a sulfur dimer vacancy E_f by a constant of $2(\mu_S + E_{H_2} - E_{H_2S})$ (about 0.7 eV). Therefore, an odd-even pattern with respect to the nanosheet sizes is also expected in the HDS reaction energy ΔE_r, see the calculated ΔE_r based on V_S@Cnr and V_S@Cen models in Figure 2.10.

2.4 Conclusions

In summary, we have studied the size effects and odd-even effects on the structural and energetic evolution of the triangular MoS_2 single-layer nanosheets using first-principles density functional theory calculations. It is found that S-terminated edge structures are energetically preferred to form and their formation energies decrease as the size of the nanosheet increases.

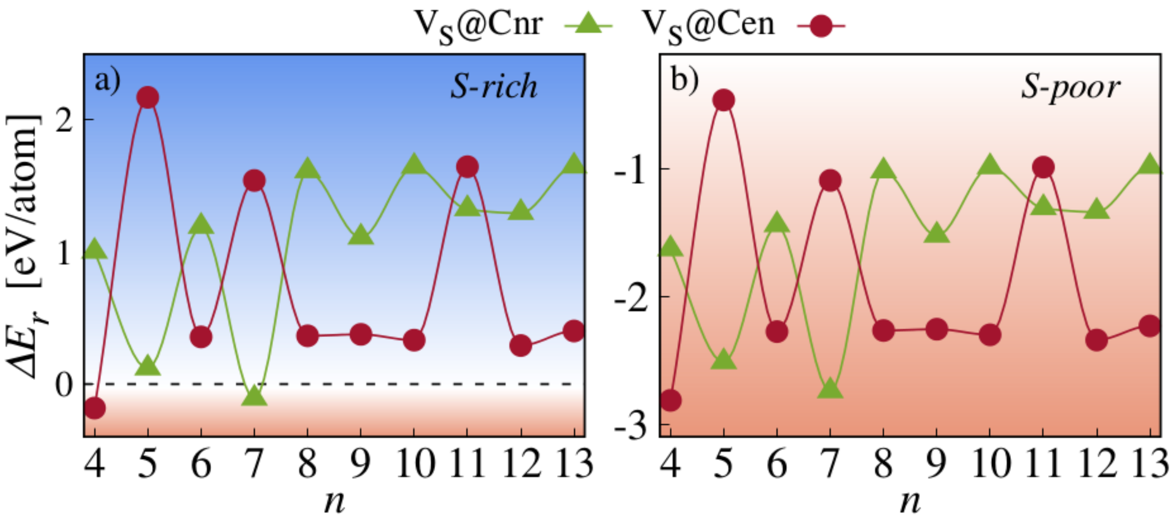

Figure 2.10: Calculated HDS reaction energy (ΔE_r) on the ZZ-S2 type MoS_2 nanosheet as a function of the size (n) of the nanosheets under the a) S-rich and b) S-poor conditions, respectively. The dash line indicated the ΔE_r at zero.

Moreover, there exists a strong odd-even effect in the formation of sulfur dimer vacancies in the S-terminated MoS_2 nanostructures. That is, at an odd number size, sulfur dimer vacancies tend to form at the corner of the MoS_2 nanosheet rather than at the center; at an even number size, sulfur dimer vacancies tend to form at the center of the MoS_2 nanosheet rather than at the corner, which can be explained from the formation of Mo-S bonds near the sulfur dimer vacancy in the relaxed structures. This finding is in an excellent agreement with experimental STM images of MoS_2 nanostructures.

2.5 Acknowledgment

Chapter 2, in full, is a reprint of the material ”Size effects and odd-even effects in MoS_2 nanosheets: first-principles studies” as it appears in Physical Chemistry Chemical Physics. Paul H. Joo, Jianli Cheng, Kesong Yang, 19, 29927-29933, 2017. The dissertation author was the primary investigator and author of this paper.

Chapter 3

Monolayer Janus MoXY nanosheets

A monolayer Janus MoXY (X/Y = S, Se, or Te) nanosheet haas, recently, been introduced for the hydrogen evolution reaction (HER) process, in which hydrogen adsorption to the catalytic site is responsible for its catalytic behaviour. By modeling two types of edge structures that resemble ZZ-S1 and ZZ-S2 from Chapter 2, we first calculate the formation energy of the triangular MoSSe and MoSTe nanosheets with respect to size to compare the structural stability of the Janus structures to the regular MoS_2. Our results reveal a similar decreasing trend in the formation energy with increase in the size of the MoSSe and MoSTe nanosheets. After confirming the best catalytic performance by the H adsorption on the corner Se-site of the ZZ-S1 MoSSe nanosheets, we calculated the hydrogen Gibbs free energies (ΔG_H) for both ZZ-S1 and ZZ-S2 MoSSe nanosheets with respect to size, each corresponding to the H-adsorption on the corner Se-site (H@Cnr). Our calculated results reveal an interesting odd-even effect on the H-adsorption at the corner of MoSSe nanosheets. The H@Cnr for the ZZ-S1 type MoSSe shows relatively lower ΔG_H for the even number of Mo atoms on the edges, while relatively higher ΔG_H for the odd number of Mo atoms. On the other hand, the H@Cnr for the ZZ-S2 type MoSSe results in a complete opposite trend. These results of the monolayer Janus MoXY nanosheets emphasize and reminds the unique structural and catalytic properties of the MoS_2 nanosheets.

3.1 Introduction

For many years, a tremendous amount of efforts has been made to synthesize high crystalline monolayer MoS_2 catalysts due to their efficient catalytic activity and the structural stability.[5, 106, 25, 114] However, the catalytic active sites are only limited to the edges of the monolayer MoS_2 catalysts and therefore, does not satisfy the requirements for the economic production.[114] There have been many attempts to improve the catalytic activity on the inert basal plane of MoS_2 by several methods, including chemical doping[115] and applying mechanical strain.[70]

Recently, monolayer Janus MoXY has been introduced as a potential alternative to MoS_2, with the intention of increasing the catalytic active sites for HER. Similar to MoS_2, MoXY also consists of two layers of chalcogen atoms, sandwiching the Mo atoms layer from top and bottom, but instead of having the same chalcogen layers, it possesses two different atoms and thus, breaking the symmetry. A typical example of a Janus monolayer MoXY is MoSSe, as it can be synthesized *via* several experimental procedures, including sulfurization of $MoSe_2$[161] and hydrogen plasma treatment.[78] It has been discovered that MoSSe nanocatalysts can provide catalytic active sites on both the Mo-edge and S/Se-edges, especially for the HER process.[114] Although there have been some important findings, there are still lack of understandings and clarifications, regarding the Janus MoXY catalysts as it has only been introduced recently.

In this chapter, we have considered the potentiality of the MoXY catalysts for HER to assume the equal potentiality for the overall catalytic activity. Hydrogen bonding to the catalytic site can play a critical role in determining the catalytic performance. Specifically, an ideal catalytic behaviour is indicated by an optimal hydrogen Gibbs free energy value, which is zero (ΔG_H=0).[86] This is because, a large negative ΔG_H means that the catalyst and hydrogen are chemcially bonded too strongly that it would permanently block the surface of the catalyst, while a large positive ΔG_H means extremely weak hydrogen bonding.[156] In this work, we modeled two triangular chalcogen-terminated MoXY nanosheets in the same manner of ZZ-S1 and ZZ-S2 edge-type MoS_2 nanosheets. We calculated the free energies corresponding to the hydrogen adsorption, in order to examine the relationship between the catalytic activity and the size of the Janus MoXY nanosheets.

3.2 Computational and Structural Details

First-principles density functional theory (DFT) calculations were performed using Vienna Ab-initio Simulation Package (VASP).[63, 60] The Projector-Augmented Wave (PAW) potential was employed for the treatment of the electron-ion interactions[7] and the Generalized Gradient Approximation (GGA) parameterized by Perdew-Burke-Ernzerhof (PBE) was used for electron exchange-correlation functional.[96] A single Γ point was used in our calculations with a cut-off energy of 310 eV for the plane-wave basis set. All the atomic positions of the Janus MoXY nanosheets were relaxed until all components of the residual forces were less than 0.02 eV/Å and the tolerance of convergence for the self-consistent-field iteration was set to 10^{-5} eV

Figure 3.1 depicts the triangular MoSSe in the ZZ-S1 and ZZ-S2 models. After structural relaxation, the MoSSe nanosheet tends to stretch outward towards the Se layer. This is assumed to be due to the difference in the atomic radius and mass between the Se and S atoms. An Se atom is larger than an S atom, having larger atomic radii and mass. Thus, Se atoms have greater repulsion to one another, relative to that of S atoms. The size of the MoXY nanosheets is indicated by the number of Mo atoms on each of the three edges of a triangular nanosheet, indicated by the variable, n.

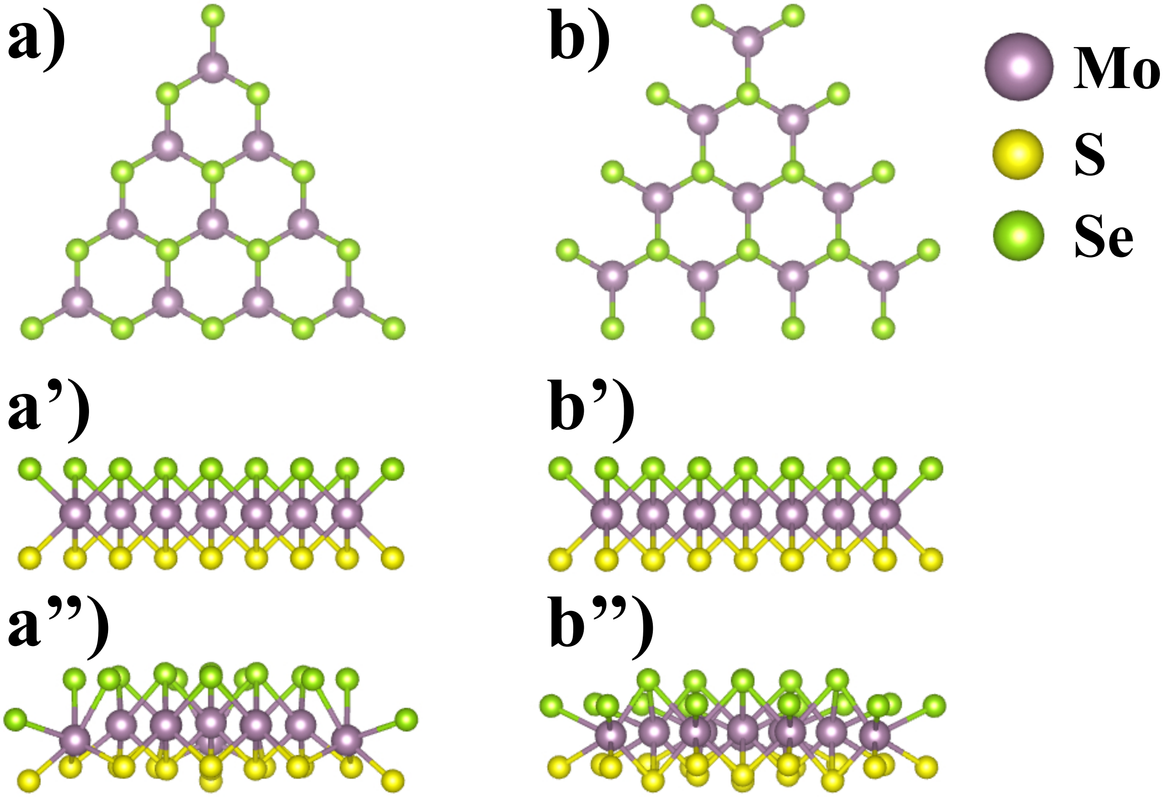

Figure 3.1: Janus single-layer MoSSe nanosheets (n = 4) with zig-zag patterned edges from top view (a-b), side view (a'-b'), and side view after structural relaxation (a"-b") , respectively. (a, a', and a") ZZ-S1, (b, b', b") ZZ-S2. The purple, yellow, and green balls represent Mo, S, and Se atoms, respectively. The size of the nanosheet (n) is indicated by the number of Mo atoms in the edge of the MoSSe nanosheet.

3.3 Results and Discussion

3.3.1 Formation Energy

To evaluate the structural stability of the MoXY nanocatalysts, we calculated the formation energies of MoSSe and MoSTe nanosheets using the equation

$$E_f = [E_{total} - zE_{MoXY} + (x-z)\mu_X + (y-z)\mu_Y]/(x+y+z) \tag{3.1}$$

where E$_{total}$ is the total energy of a MoXY nanosheet, E$_{MoXY}$ is the total energy of the bulk MoXY structure, μ_X and μ_Y are the chemical potentials of X (S) and Y (Se or Te), respectively, and x, y, and z is the number of X, Y, and Mo atoms, respectively.

The calculated formation energies are plotted in Figure 3.2 with respect to the size ,*n*. As a comparison, the formation energies of MoS_2 nanosheets are re-shown in the plot. Similar to the MoS_2 nanosheets, the formation energies of MoSSe and MoSTe both show a decreasing trend with respect to size, indicating that larger MoXY nanosheets are energetically more favorable to form. The order of structural stability of the triangular nanosheets goes from MoSTe (most stable), MoSSe, then MoS_2 (least stable). This, in fact, agrees for both the ZZ-S1 and ZZ-S2 edge types. Therefore, the structural stability of the triangular Janus MoXY nanosheets follows the exact same size effects as the MoS_2 nanosheets.

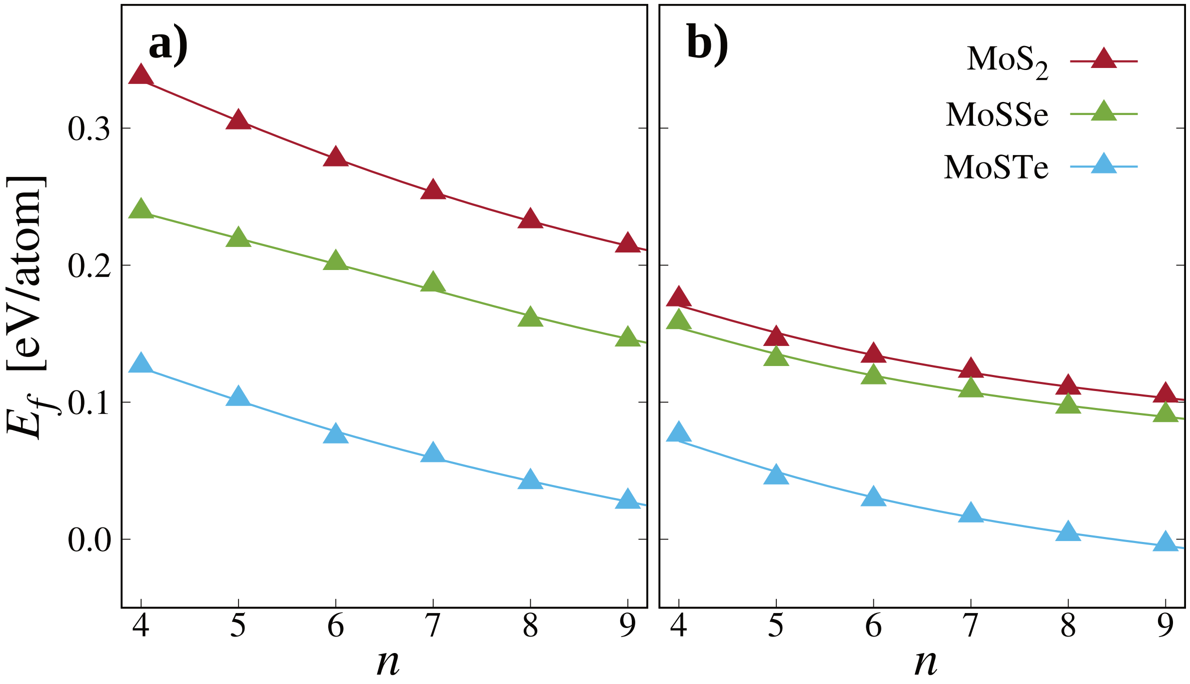

Figure 3.2: Calculated formation energies of a) ZZ-S1 and b) ZZ-S2 models of MoS_2 (red), MoSSe (green), and MoSTe (cyan) nanosheets, with respect to the size (*n*).

3.3.2 Hydrogen Gibbs Free Energy

In order to evaluate the catalytic performances of the MoXY nanosheets, one hydrogen atom (H^+) was applied to the catalytic sites on the Se layer of the the MoSSe nanosheets. The hydrogen-adsorbed MoSSe nanosheet (H^*-MoSSe) acts as an intermediate state, being responsible for its catalytic activity. The ideal Gibbs free energy of the hydrogen-bonded MoSSe must be zero ($\Delta G_H = 0$) in order to be catalytically active. In that sense, the Gibbs free energy value that is close to zero can be considered as active.

As representatives, the MoSSe nanosheets of n = 4 and 5 were considered and one hydrogen atom was applied on each of the different Se-sites. The Gibbs free energy of the H^*-MoSSe nanosheets was then calculated using the equation

$$\Delta G_H = \Delta E_H + \Delta E_{ZPE}(H) - T\Delta S_H \tag{3.2}$$

where ΔE_H is the difference in the total energy between H^*-MoSSe and unbound hydrogen and MoSSe nanosheet, separately, and $\Delta E_{ZPE}(H)$ and ΔS_H are the difference in zero point energy and entropy of hydrogen, respectively, between its adsorbed states and its isolated states. The value of 0.41 eV for $T\Delta S_H$ was taken from past literature[114], where ΔS_H is half entropy of H_2 in the gas phase at T = 300K.

Primarily, ΔG_H was calculated for the H-adsorption on each of the possible Se-sites of the ZZ-S1 MoSSe nanosheets (n = 4 and 5). Figure 3.3a represents the plotted ΔG_H with respect to the H-adsorption site. The geometrical representation of the H-adsorption at each site is shown in Figure 3.3b and c for n = 4 and 5, respectively. Based on the calculations, the followings are revealed:

(i) The H-adsorption on the edges, excluding the corner site, leads to a relatively larger negative value of ΔG_H, indicating a spontaneous H-adsorption process and thus, more difficult for the H atom to desorb. On the other hand, the H-adsorption near the center of the nanosheet leads to a relatively large positive value of ΔG_H, which means more energy is required for the hydrogen to adsorb.

(ii) The H-adsorption at the corner site results in ΔG_H that is the closest to zero for both MoSSe nanosheets with $n = 4$ and 5, indicating the best catalytic behavior.

Since the best catalytic behavior was revealed with the H-adsorption at the corner, both ZZ-S1 and ZZ-S2 MoSSe were taken into account to calculate the ΔG_H for the corner adsorption of hydrogen with respect to the size of the nanosheets. The calculated ΔG_H of ZZ-S1 and ZZ-S2 MoSSe nanosheets are plotted in Figure 3.4a. Figure 3.4b and c depict the geometrical representation of the H-adsorption at the corner site of ZZ-S1 and ZZ-S2 MoSSe nanosheets, respectively.

Interestingly, a similar odd-even effect is shown with the Janus structures. For ZZ-S1 structures, the MoSSe nanosheets with even n's have relatively lower ΔG_H, as compared to relatively higher ΔG_H for the odd n's. The ZZ-S2 structures, on the other hand, result in a complete opposite odd-even effect. As a result, the ZZ-S1 nanosheet with $n = 5$ and the ZZ-S2 nanosheet with $n = 4$ demonstrate the best catalytic behavior, as indicated by the values of ΔG_H at 0.10 and -0.19 eV, respectively, which are closest to zero.

The odd-even effects revealed with the formation sulfur vacancies, due to the new structural equilibrium state based on the size of the MoS_2 nanosheets, can relate to the catalytic activity MoS_2, since sulfur vacancy generation is a primary step in the catalytic reaction. Similarly, the Janus MoSSe nanosheets also demonstrate the odd-even effects with respect to size, with the adsorption of hydrogen at the catalytic sites. In conclusion, the catalytic behavior within the 2D TMS catalysts can significantly differ with insignificant changes in size and therefore, further understanding of the structural, thermodynamic, and catalytic properties is necessary for future research directions.

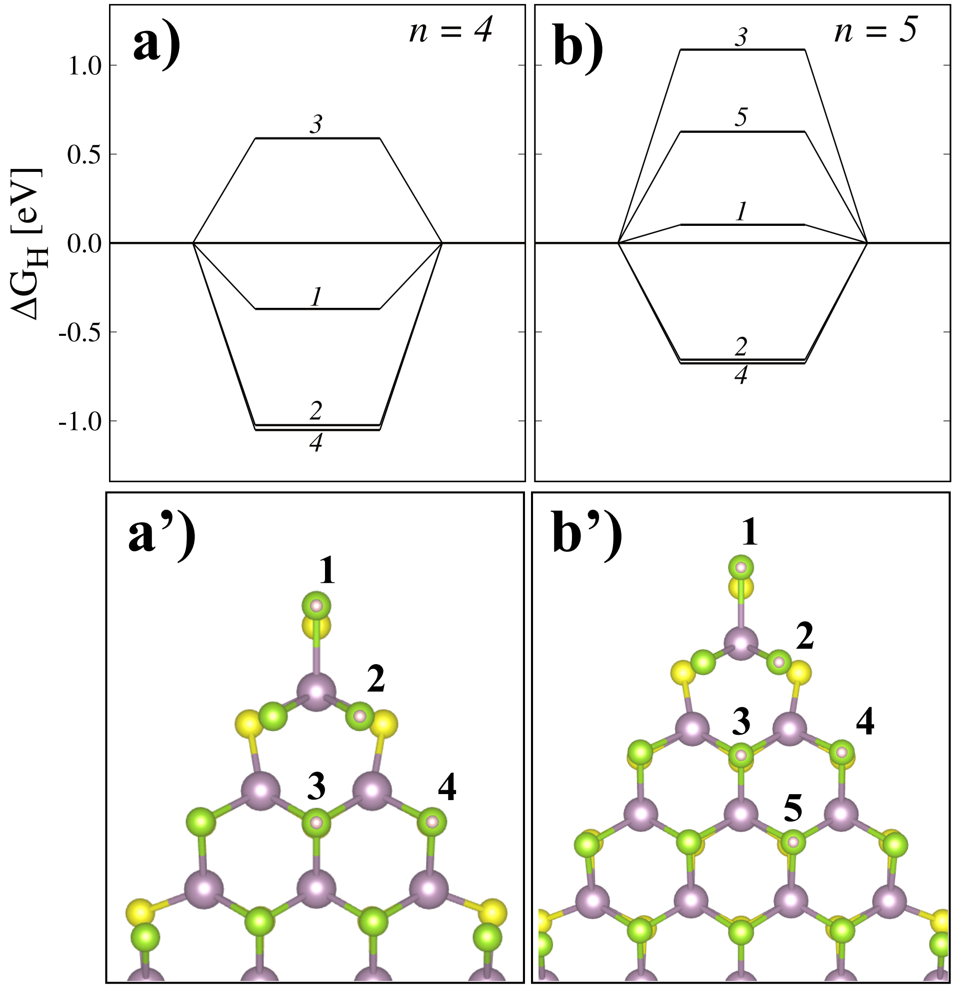

Figure 3.3: a) Calculated hydrogen Gibbs free energies (ΔG_H) with respect to the different H-adsorption sites of ZZ-S1 MoSSe nanosheets. The red triangles and green circles indicate the calculated ΔG_H for n = 4 and 5, respectively. b-c) The geometrical display of the H-adsorption sites for n = 4 and 5, respectively.

3.4 Conclusions

In summary, we have discovered the similar size and odd-even effects on the structural evolution and the catalytic behaviour, respectively. With the same decreasing trend in the formation energy with respect to size, the order of energetic preference of formation is MoSTe, MoSSe, then MoS_2. Furthermore, hydrogen adsorption plays a key role in determining the catalytic activity, in which ΔG_H shoule be closer to zero in order to be active. The H@Cnr for

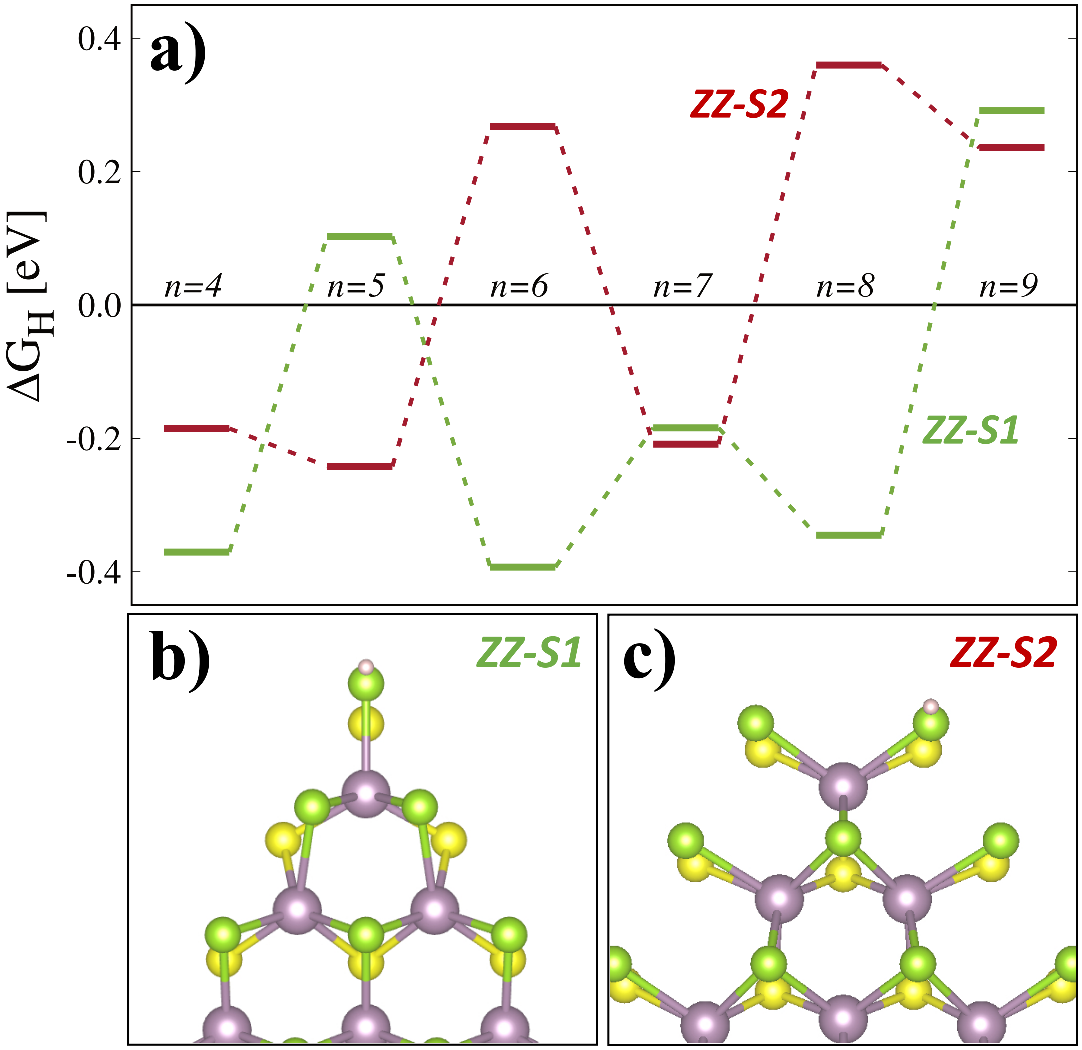

Figure 3.4: a) Calculated hydrogen Gibbs free energies (ΔG_H) of ZZ-S1 and ZZ-S2 MoSSe nanosheets with respect to size, *n*. b-c) The geometrical display of the H-adsorption at the corner site for ZZ-S1 and ZZ-S2 nanosheets, respectively.

both ZZ-S1 and ZZ-S2 edge-type MoSSe nanosheets reveals an odd-even effect, but in a complete opposite trend. The ZZ-S1 MoSSe shows relatively lower ΔG_H for even *n*'s, while ZZ-S2 MoSSe shows relatively lower ΔG_H for odd *n*'s. Finally, from the calculated ΔG_H, ZZ-S1 MoSSe with *n*=5 and ZZ-S2 MoSSe with *n*=4 result in the values closest to zero and therefore, are the most catalytically active from the theoretical point of view.

Chapter 4

Descriptors of Transition Metal Promoters on MoS_2 Nanocatalysts for Hydrodesulfurization: Binding Energy of Metal Sulfides from First Principles

In Chapter 2, we have discussed the effects associated with the structural stability of the triangular MoS_2 nanosheets. Since MoS_2-based catalysts have been used in the petroleum refinery industry for decades, it is of long-term interests to improve their catalytic efficiency in HDS process. In this chapter, we report a comprehensive computational study of TM promotion effects on the catalytic activity of MoS_2 nanosheets with 26 TM elements, including ten 3*d*, eight 4*d*, and eight 5*d* elements, using sulfur-terminated hexagonal MoS_2 nanosheets. The HDS activity of sulfur saturated TM-MoS_2 nanocatalysts is evaluated by modeling three consequent steps in an HDS process with a dibenzothiophene molecule. We calculated the reaction energy for each step with respect to the binding energy (E_b) of TM sulfides and found that E_b can be an effective descriptor for selecting TM promoters to enhance the catalytic activity of MoS_2 nanocatalysts, that is, E_b of an ideal TM promoter should neither be extremely high nor extremely low. On the basis of this descriptor, several candidate TM promoters including Mn, Cr, Co, Fe, Ni, V, Ru, and Pt are identified, which is consistent with prior experimental findings. This work is expected to provide an informative guide to the design of high-performance MoS_2-based nanocatalysts for HDS.

4.1 Introduction

Several methods including the synthesis of MoS_2 nanoflowers and nanotubes, fabrication of MoS_2-based heterostructures, and edge-promotion *via* TM atoms, have been introduced in Chapter 1.[21, 33, 20, 22, 102] The TM promotion on the hexagonal MoS_2 nanosheets enables the enhancement of catalytic active sites,[102, 85] in which these adsorption sites can attract and convert the organic compounds into clean diesel fuel compounds. [20, 22, 102] For example, Rao *et al.* conducted the HDS reaction of thiophene with Co- and Ni-promoted MoS_2 and reached a conversion efficiency of 97.8% and 94%, respectively, under 375°C.[102] Niefield *et al.* revealed a direct desulfurization path of the HDS process with Co-promoted MoS_2 nanosheets in the forming gas (H_2/N_2) atmosphere.[85] In addition to Co[107, 101, 69, 11, 139, 22] some other TM promoters including Ni[101, 69, 11, 139, 24] Fe,[11, 139] Cu,[139] and Zn[117] have also been explored in the experimental side. In contrast, the effects of various TM promoters on the HDS activity of MoS_2 nanocatalysts are not fully understood yet from the theoretical side. For instance, one might wonder which TM promoter can best improve the HDS activity of MoS_2 nanocatalysts, and to answer this question, a systematic comparison of the promotion effects of various TM atoms on the MoS_2 nanocatalysts is necessary.

In Chapter 3, using first-principles density functional theory calculations, we studied the effects of 26 TM elements, as a promoter on the hexagonal MoS_2 nanosheets, on the catalytic activity in the HDS process. The article is organized as follows. First, we discussed the energetic stability of the TM-promoted MoS_2 nanosheets by calculating the binding energies. Next, we calculated the formation energies of sulfur vacancy on the promoted edge of the nanosheets. Lastly, we evaluated the catalytic activity by calculating the reaction energies in the HDS process. Our results show that the binding energy of TM sulfides could be one effective descriptor for selecting TM promoters for the MoS_2 nanocatalyts to optimize catalytic activity for HDS.

4.2 Computational Details

First-principles density functional theory (DFT) electronic structure calculations were carried out using the Vienna *Ab initio* Simulation Package (VASP).[63, 60] The Projector Augmented Wave (PAW) potential was employed for treating electron-ion interactions[7] and the Generalized Gradient Approximation (GGA) parameterized by Perdew-Burke-Ernzerhof (PBE) was applied for the electron-correlation functional.[96] A cut-off energy of 450 eV for the plane-wave basis set, a convergence tolerance of 10^{-4} eV for the self-consistent-field iteration, and a single k-point with wavevector at Γ point were used in our calculations. The atomic positions of the MoS_2 nanosheets were fully relaxed until all components of the residual forces became less than 0.05 eV/Å. To model the hydrodesulfurization process, the Grimme's D3 dispersion correction on the PBE functional (PBE+D3) was employed to calculate the chemical reaction energy between the organosulfur compounds and MoS_2 nanosheets, since it is capable of predicting more accurate thermochemical energy.[31] Zero-point energies were calculated based on the harmonic frequencies of the molecules adsorbed on the substrates. The movement of the substrates was assumed to be negligible compared to the movement of the absorbing molecules.[83, 109]

A single-layer MoS_2 nanosheet structure consists of one Mo layer and two S layers, with the Mo layer sandwiched by the two S layers. In our prior work, we defined two types of zig-zag edges for MoS_2 nanosheet structure, including ZZ-S1 and ZZ-S2.[49] The ZZ-S1 edge has a S-termination, with each S dimer coordinatively bonded to two Mo atoms. The ZZ-S2 edge also

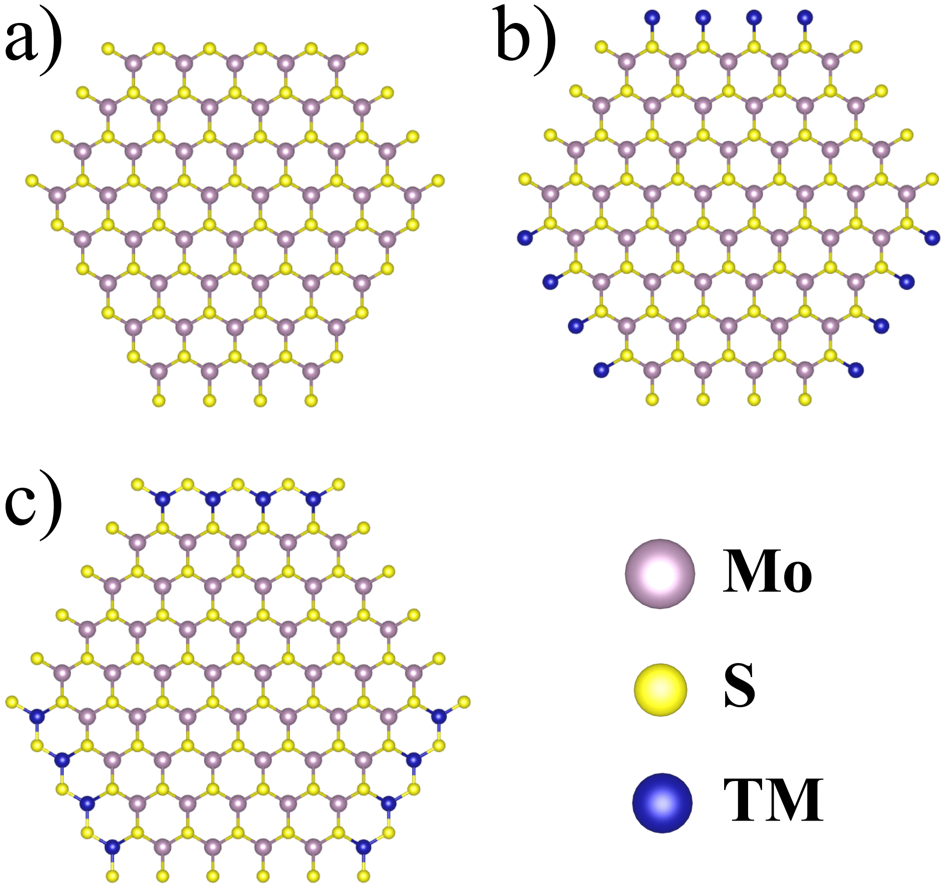

Figure 4.1: Schematic illustration of single-layer hexagonal MoS_2 nanosheet structures. (a) Unpromoted and (b) promoted with transition-metal (TM) atoms without and (c) with sulfur saturation.

has a S-termination, but with S dimers protruding externally in a perpendicular direction from the edges.[49] In this work, a hexagonal MoS_2 nanosheet model was built with three ZZ-S1 and three ZZ-S2 edges, see Figure 4.1a. This is because, such a configuration has been experimentally confirmed using the atom-resolved STM images.[38, 69, 137, 143] To eliminate the interaction between neighboring slabs, a vacuum region of 10 Å was applied in our models. Based on the growth conditions of the MoS_2 nanosheet and inspired by prior experimental studies,[164] we built another two models for the TM promotion, including one without sulfur saturation (see Figure 4.1b) and the other with sulfur saturation (see Figure 4.1c). The promoted MoS_2 model was built by promoting S dimers of the three ZZ-S1 edges with TM atoms which share the same layer with Mo atoms. The TM atoms including ten 3*d*, eight 4*d*, and eight 5*d* elements were selected. In the case of TM-promoted model with sulfur saturation, S monomers are attached on the TM atoms in the same layer, in a similar manner of ZZ-S1 type edge. Such model resembles the Co-[22, 101, 32] and Ni-[101]promoted MoS_2 nanosheets observed in the experiments.

4.3 Results and Discussion

4.3.1 Binding Energy

To quantitatively evaluate the binding strength between TM atoms and MoS_2 nanosheets, we first calculated the binding energies (E_b^{sheet}) of the TM-promoted MoS_2 nanosheets without sulfur saturation using the formula:

$$E_b^{sheet} = [E_{unprom} + x\mu_{TM} - E_{prom}]/x \tag{4.1}$$

where x and μ_{TM} are the total number and the chemical potential of the TM atom, respectively. E_{unprom} and E_{prom} indicate the total energy of the unpromoted and promoted hexagonal MoS_2 nanosheets, respectively.

The calculated binding energies for these TM-promoted MoS_2 nanosheets are shown in Fig 4.2a. The binding energy can be interpreted as the energy required for the TM atoms to detach from the MoS_2 nanosheets. Our results show a negative binding energy for most of TM-MoS_2 nanosheets except for Sc-, Y-, Zn-, and Cd-MoS_2. The negative binding energy indicates a spontaneous dissociation of the TM atoms from the MoS_2 nanosheet, which implies that TM promotion on the nanosheet without sulfur saturation is not energetically possible.

Next, we calculated the binding energy (E_b^{satu}) of the TM-promoted model with sulfur saturation using the equation:

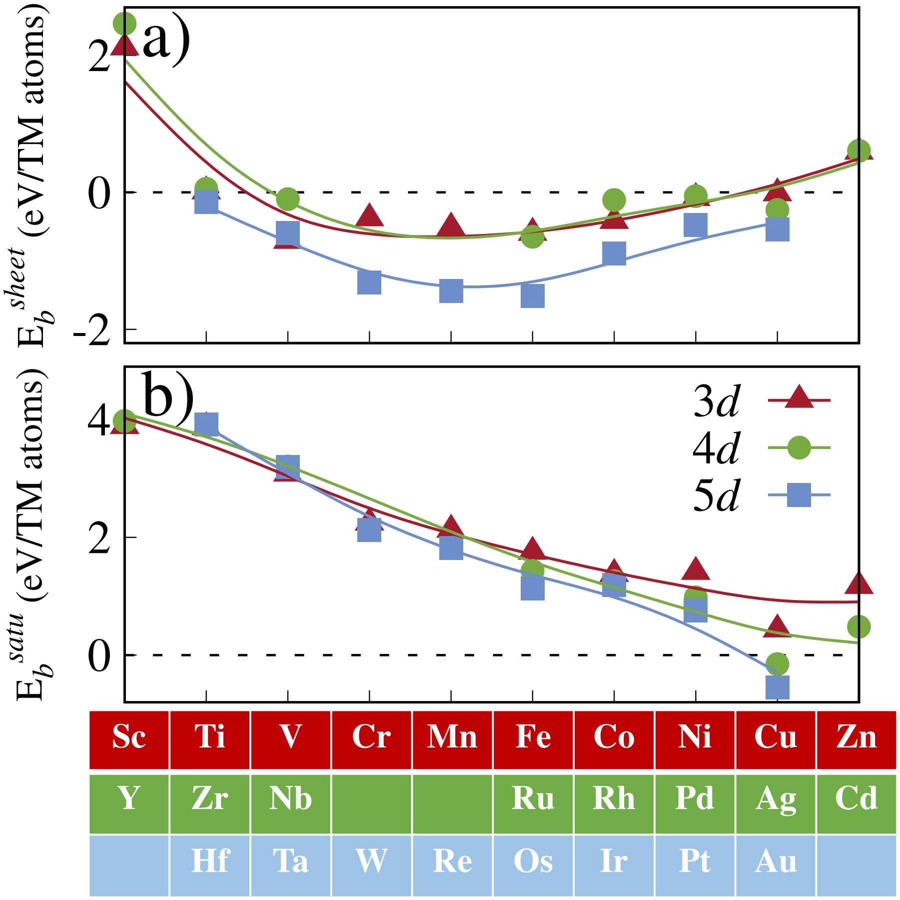

Sc	Ti	V	Cr	Mn	Fe	Co	Ni	Cu	Zn
Y	Zr	Nb			Ru	Rh	Pd	Ag	Cd
	Hf	Ta	W	Re	Os	Ir	Pt	Au	

Figure 4.2: Calculated binding energies of TM-promoted MoS_2 nanosheets a) without and b) with sulfur saturation. The chemical potentials of TM and sulfur atoms calculated from their ground state bulk structures were used in this and subsequent figures.

$$E_b^{satu} = [E_{unprom} + x\mu_{TM} + y\mu_S - E_{satu}]/x \tag{4.2}$$

where E_{satu} is the total energy of the sulfur saturated TM-MoS_2, μ_{TM} and μ_S are the chemical potentials of the TM and S atom, respectively, and x and y are total number of the TM atoms and the saturating S atoms on the promoted edges, respectively.

The calculated binding energies of the TM-promoted MoS_2 nanosheets with sulfur saturation are plotted in Figure 4.2b. Our calculations reveal two major conclusions:

1) All TM-MoS_2 nanosheets have a positive binding energy, except for Ag- and Au-MoS_2.

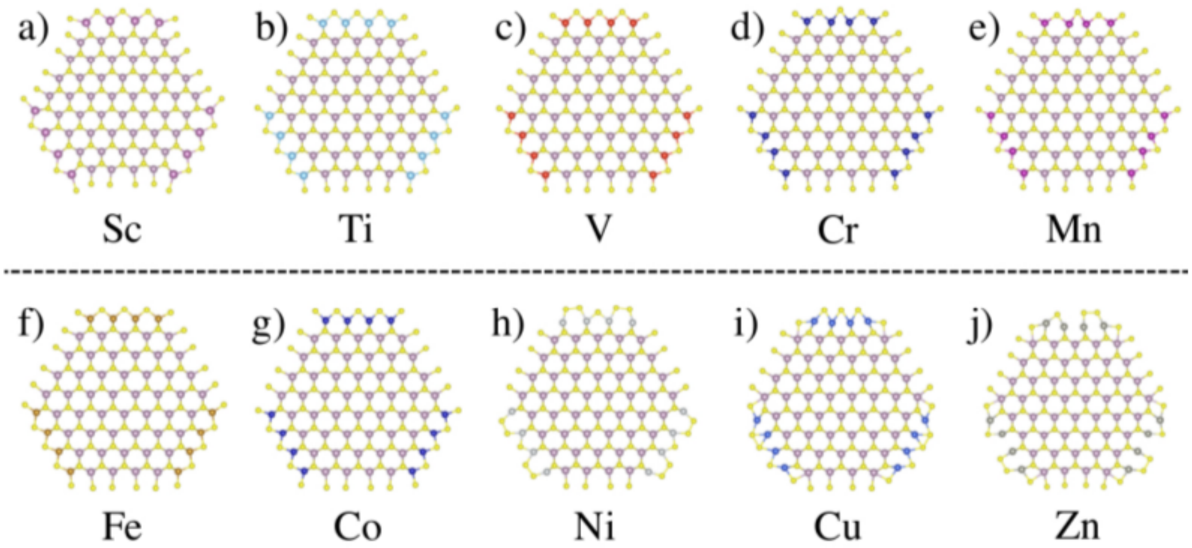

Figure 4.3: Geometrical structures of the relaxed TM-promoted MoS_2 nanosheets with sulfur saturation, with the 3d TM promoters; a) Sc, b) Ti, c) V, d) Cr, e) Mn, f) Fe, g) Co, h) Ni, i) Cu, and j) Zn.

This indicates the feasibility of the TM promotion on the MoS_2 nanosheet under the sulfur saturating condition as compared to the infeasibility under unsaturating condition.

2) The binding energy decreases along the groups in the periodic table for each of the 3*d*, 4*d*, and 5*d* TM elements. The TM atoms from group 3 (Sc and Y) and group 4 (Ti, Zr, and Hf) lead to the higher binding energy, while the TM atoms from group 11 (Cu, Ag, and Au) and group 12 (Zn and Cd) lead to the lower binding energy. This can be explained from the electronegativity of the TM elements. For the TM elements with low electronegativity (high electropositivity) in the lower groups of periodic table, they tend to cause strong binding with S atom. For the TM elements with high electronegativity (low electropositivity) in the high groups of periodic table, they tend to have weaker binding with the S atom.

As a reference, the geometrically relaxed structures of the 3*d* TM-promoted MoS_2 nanosheets with sulfur saturation are shown in Figure 4.3.

4.3.2 Formation Energy of Sulfur Vacancy

Next, we calculated the formation energy of sulfur vacancy on the TM-MoS$_2$ nanosheets with sulfur saturation. This is because the sulfur vacancy site is considered as an active site and plays a critical role in the HDS reaction by attracting the organosulfur compounds. The sulfur vacancy site is also called the coordinatively unsaturated site (CUS),[49] which has been spotted *via* STM images in the experiment.[66] In this work, the sulfur vacancy (V$_S$) was modeled by removing one sulfur monomer from the center site of the TM-promoted edge (V$_S$@Cen). The formation energy of V$_S$@Cen was calculated using the equation,

$$E_f = E_{V_S@Cen} + \mu_S - E_{satu} \tag{4.3}$$

where $E_{V_S@Cen}$ is the total energy of the V$_S$@Cen and μ_S is the chemical potential of the S atom.

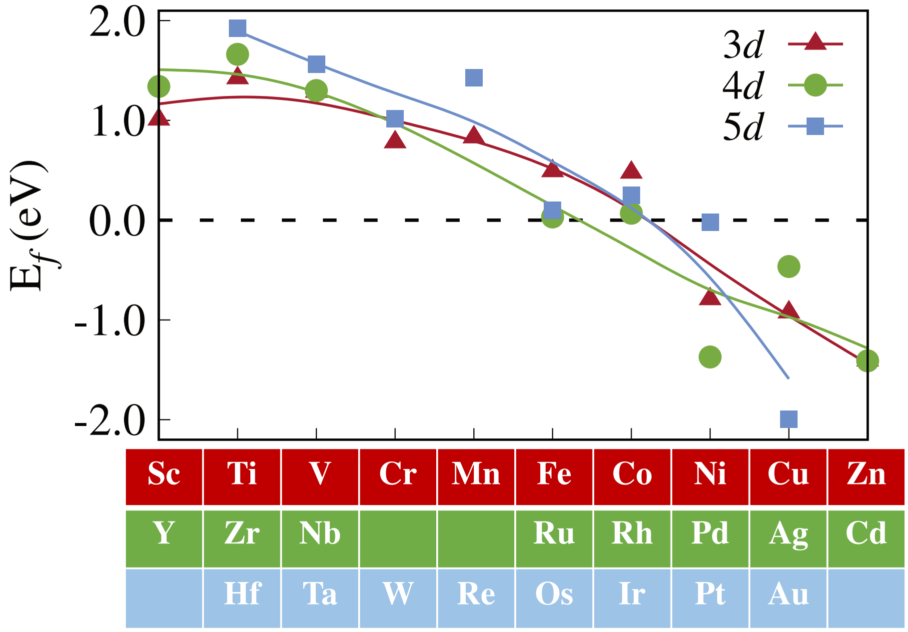

Figure 4.4: Calculated formation energies of TM-promoted MoS$_2$ nanosheets with sulfur vacancy at the center site of the saturated edge (V$_S$@Cen) at sulfur-poor condition.

The calculated formation energies of V$_S$@Cen are depicted in Figure 4.4. It shows that the formation energy, generally, decreases from group 3 to group 12 for all rows of 3*d*, 4*d*, and 5*d* TM elements, indicating that V_S@Cen is energetically more favorable in the systems with TM promoters in the higher groups of periodic table. Interestingly, the V_S@Cen for Ni-, Cu-, Zn-, Pd-, Ag-, Cd-, and Au-MoS_2 nanosheets have a negative formation energy (-0.79, -0.93, -1.41, -1.37, -0.46, -1.41, and -2.00 eV, respectively), which indicates a spontaneous formation of V_S@Cen. This can directly relate to the decreasing trend in the binding energy (E_b) for TM-sulfides, shown in Figure 4.5. In general, E_b decreases with the TM atoms from group 3 to group 12. ScS and TiS have a relatively high E_b of 5.63 and 5.74 eV/atom, respectively, while ZnS has a relatively low E_b of 2.99 eV/atom, as shown in Figure 4.5 and Table 4.1. A lower E_b means weaker binding strength between the TM and S atoms, thus leading to a relatively easier formation of V_S.

In fact, the decrease in the formation energy of V_S@Cen can also relate to the decrease in the binding energy of the TM-MoS_2 with sulfur saturation (Figure 4.2b), because such binding energy also reflects on the binding strength between the TM and S atoms. However, their difference is that the V_S@Cen formation accounts for the interaction between the TM atoms and the S monomers that lie on top of the promoted TM atoms, while the binding energy of the TM-MoS_2 with sulfur saturation refers to the interaction between the TM atoms and the S dimers that connect the TM atoms to the MoS_2 nanosheet.

As a reference, the geometrically relaxed structures of the 3*d* TM-promoted MoS_2 nanosheets with V_S@Cen are shown in Figure 4.6.

4.3.3 Hydrodesulfurization Modeling

The HDS process consists of three consequent steps: (1) generation of V_S, (2) adsorption of a S-containing organic molecule into the V_S site of the catalyst via the S atom, and (3) desulfurization of the organic molecule with S refilling the V_S site. The schematic diagram of the HDS process is shown in Fig. 4.7. Dibenzothiophene (DBT) is a typical natural-occurring organosulfur compound in petroleum.[81] Here, we modeled the HDS by using the DBT molecule

Table 4.1: Calculated binding energy values of the TM-sulfides corresponding to the 3*d*, 4*d*, and 5*d* TM elements.

	3*d*		4*d*		5*d*	
group	TM-sulfides	E_b(eV/atom)	TM-sulfides	E_b(eV/atom)	TM-sulfides	E_b(eV/atom)
3	ScS	5.63	YS	6.09	LaS	6.06
4	TiS	5.74	ZrS	6.14	HfS_2	6.36
5	VS	5.20	NbS	6.09	TaS	6.36
6	Cr_2S_3	4.06	Mo_7S_8	5.22	WS	5.96
7	Mn_2S_3	3.94			ReS_2	5.32
8	FeS	4.70	RuS_2	4.95	OsS_2	5.31
9	Co_9S_8	4.75	Rh_2S_3	3.48	Ir_2S_3	5.25
10	NiS	4.41	PdS	3.71	PtS	4.78
11	CuS	3.58	Ag_2S	2.80	Au_2S	3.15
12	ZnS	2.99	CdS	2.64	HgS	1.85

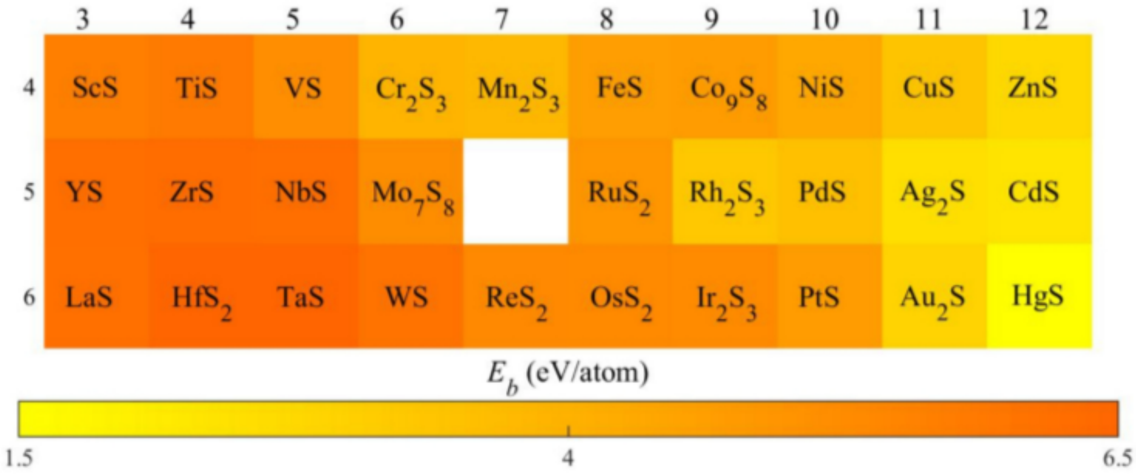

Figure 4.5: Binding energy for the TM-sulfides plotted in rows and columns of the periodic table. Orange means high binding energy, while yellow is for low binding energy.

as a feed compound which becomes a biphenyl (BP) after the HDS reaction. The attachment of DBT to the V_S@Cen site was modeled in a perpendicular orientation to minimize steric hindrance. To evaluate HDS activity of TM-MoS_2 nanosheets, we calculated the Gibbs free energies for each of reaction (1), (2), and (3) using the following equations by taking zero point energy and entropy

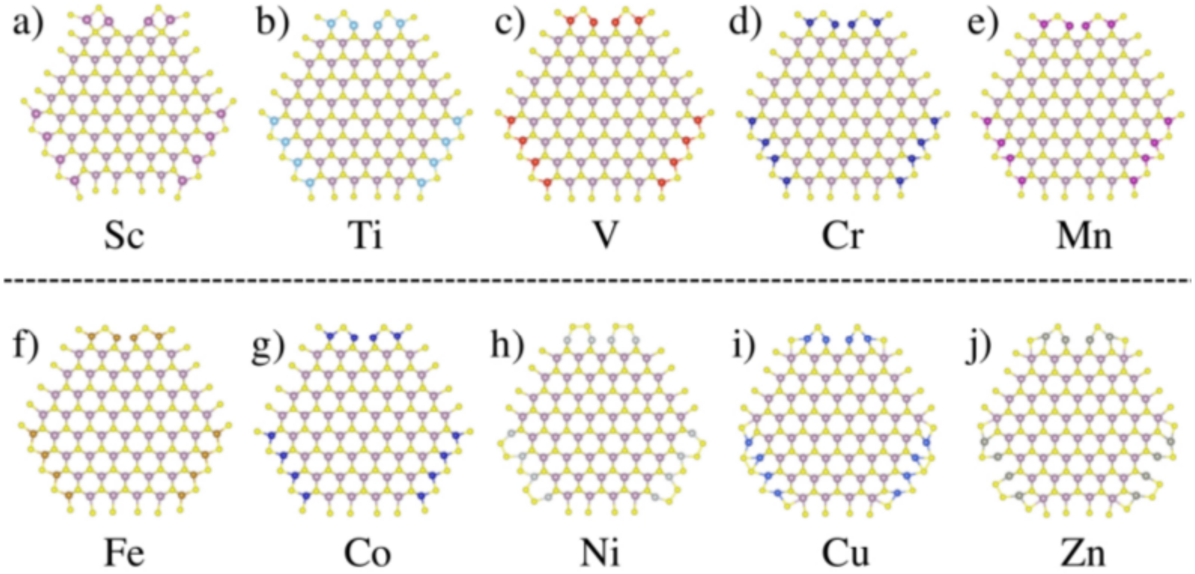

Figure 4.6: Geometrical structures of the relaxed TM-promoted MoS_2 nanosheets without sulfur saturation, with the 3d TM promoters; a) Sc, b) Ti, c) V, d) Cr, e) Mn, f) Fe, g) Co, h) Ni, i) Cu, and j) Zn.

corrections into account, respectively:

$$\Delta G_1 = \Delta E_1 - \Delta E_{ZPE}(H_2) - \Delta E_{ZPE}(H_2S) - T(\Delta S_{H_2S} - \Delta S_{H_2}) \tag{4.4}$$

$$\Delta G_2 = \Delta E_2 + \Delta E_{ZPE}(DBT) + T\Delta S_{DBT} \tag{4.5}$$

$$\Delta G_3 = \Delta E_3 - \Delta E_{ZPE}(H_2) - \Delta E_{ZPE}(BP) - T(\Delta S_{BP} - \Delta S_{H_2}) \tag{4.6}$$

where ΔE_1, ΔE_2, and ΔE_3 are the reaction energies in reaction (1), (2), and (3), respectively; $\Delta E_{ZPE}(H_2)$, $\Delta E_{ZPE}(H_2S)$, $\Delta E_{ZPE}(DBT)$, and $\Delta E_{ZPE}(BP)$ and ΔS_{H_2}, ΔS_{H_2S}, ΔS_{DBT}, and ΔS_{BP} are the difference in zero point energy and entropy of H_2, H_2S, DBT, and BP between their adsorbed states and their isolated states, respectively. The room temperature 298 K was used in calculations. The difference in entropy are obtained from $S^{\circ}_{H_2S}$[133], $S^{\circ}_{H_2}$[133], S°_{DBT}[19], and

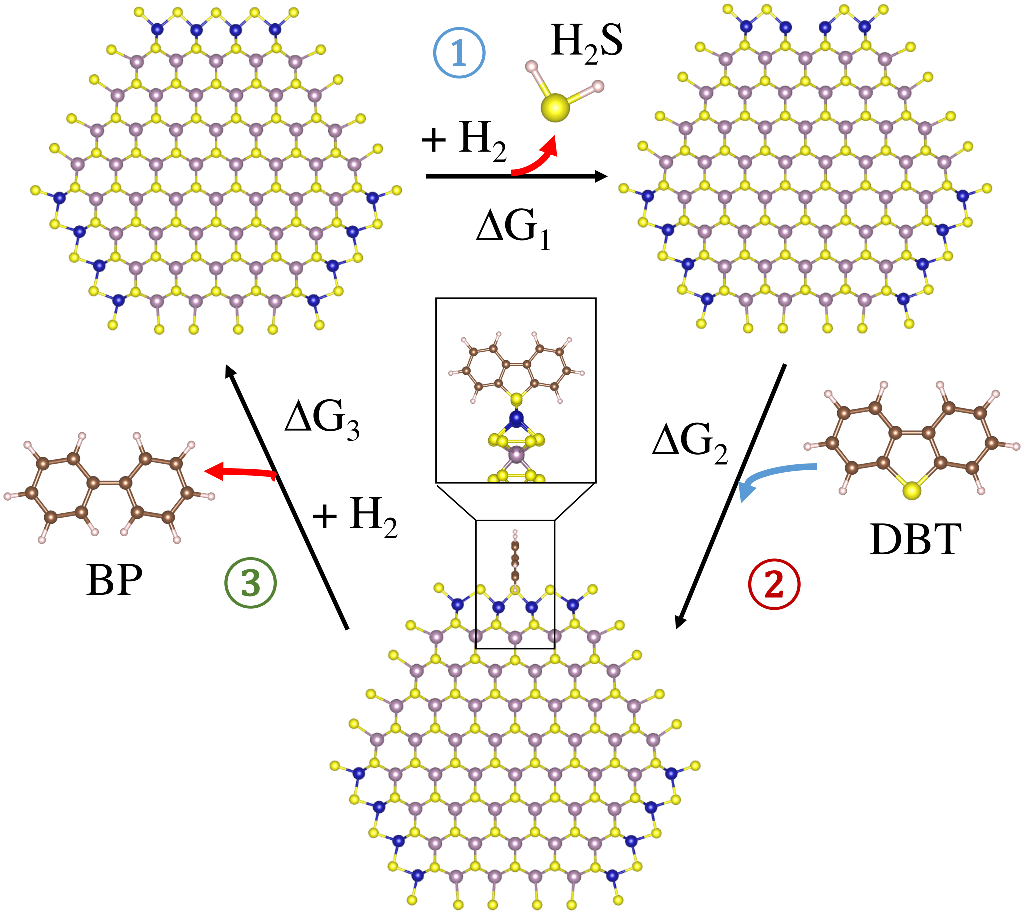

Figure 4.7: The schematic diagram of the HDS reaction of DBT to BP with TM-MoS_2 nanosheet. (1) Generation of sulfur vacancy at the center site of the edge (V_S@Cen), (2) Adsorption of DBT, and (3) Desulfurization of DBT into BP. The blue arrow indicates the incoming reactant in the reaction, while the red arrow indicates the release of a product in the reaction.

S°_{BP}[18], respectively, based on the assumption that the vibrational entropy in their adsorbed states is small.[86] The calculated difference in zero point energy and entropy is listed in the Table S1 of Supporting Information for reference. Also note that the magnitudes of $\Delta E_{ZPE}(H_2)$ in equations (4) and (6) are slightly different since their absorbed states are different, with MoS_2 and BP being as their absorbing systems, respectively. The reaction energies for reaction (1), (2), and (3) can be calculated using the following equations, respectively:

$$\Delta E_1 = E_{V_S@Cen} + E_{H_2S} - E_{MoS_2} - E_{H_2} \tag{4.7}$$

$$\Delta E_2 = E_{DBT-MoS_2} - E_{V_S@Cen} - E_{DBT} \tag{4.8}$$

$$\Delta E_3 = E_{MoS_2} + E_{BP} - E_{DBT-MoS_2} - E_{H_2} \tag{4.9}$$

where E_{MoS_2}, E_{H_2S}, and E_{H_2} are the total energy of TM-MoS_2 (equivalent to $E_{saturated}$), H_2S, and H_2, respectively, and $E_{DBT-MoS_2}$, E_{DBT}, and E_{BP} are the total energy of DBT-adsorbed TM-MoS_2, DBT, and BP, respectively. The ΔG_1, ΔG_2, and ΔG_3 are plotted against the calculated binding energy (E_b) of binary transition-metal sulfides in Fig. 4.8a, b, and c, respectively. There are two reasons to choose E_b as a descriptor: i) E_b generally measures the bonding strength between the TM and S atoms, which is strongly correlated to the formation of V_S and chemical adsorption of the DBT via TM-S bond. ii) E_b is a relatively simple parameter that can be accessed from both experiments and theoretical calculations. Actually, earlier experimental and theoretical studies both indicate a correlation between the trends of the HDS activity and the binding energy of sulfur to the transition metals (or the positions of the metals in the periodic table).[95, 87] The 3*d*, 4*d*, and 5*d* TM promoters are depicted as red triangle, green circle, and blue square points, respectively. The calculated E_b is listed in Table S2 for reference.

The ΔG_1 in Fig. 4.8a represents the reaction energy of V_S@Cen under the H_2 exposure. It shows that ΔG_1 increases as E_b increases, meaning that more energy is required to create V_S@Cen. In contrast, a lower E_b leads to a relatively lower ΔG_1, indicating an easier formation of V_S@Cen. In fact, the negative ΔG_1 for Cu-, Ni-, Zn-, Pd-, Cd-, Ag-, and Au-MoS_2 nanosheets indicates spontaneous formation of V_S@Cen.

The ΔG_2 in Fig. 4.8b represents the reaction energy of DBT adsorbing into the V_S@Cen of the TM-MoS_2 nanosheet. For MoS_2 with 3*d* TM promoters, ΔG_2 first decreases, then increases as E_b increases. The primary decrease in ΔG_2 can be explained by a strong binding strength between the TM atoms and the S atom as indicated by high E_b. A lower ΔG_2 means that less

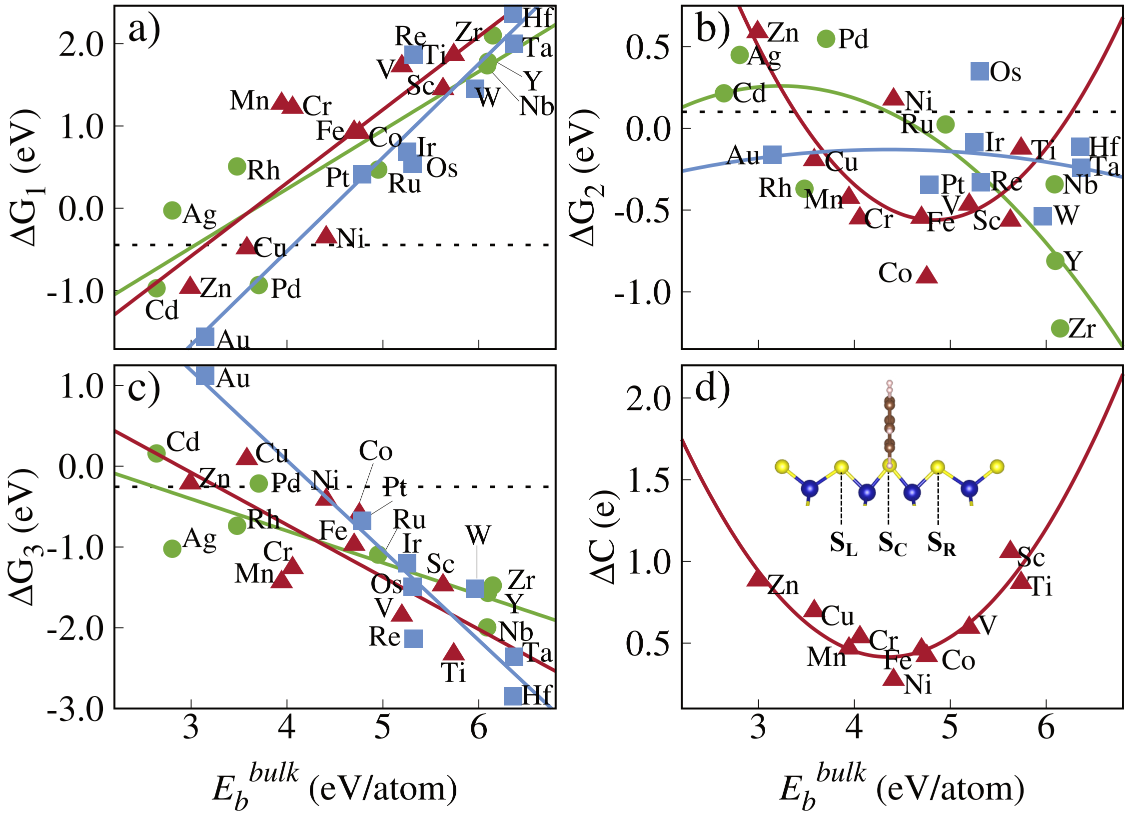

Figure 4.8: Calculated Gibbs free energies, a) ΔG_1, b) ΔG_2, and c) ΔG_3 with respect to the binding energy (E_b) of each corresponding TM-sulfides, d) the plotted Bader charge difference (ΔC) between the transferring S atom (S_C) and the adjacent S atoms (S_L and S_R). The 3*d* promoters are in red triangle, 4*d* promoters in green circle, and 5*d* promoters in blue square points. The dashed lines indicate the Gibbs free energies of the reactions with the unpromoted MoS_2 nanosheet.

energy is required for the adsorption of DBT to the MoS_2 nanosheet and therefore, it can also be interpreted as a stronger adsorption of DBT. Interestingly, ΔG_2 starts to increase as E_b increases over ∼4.75 eV/atom. To understand this behavior, we studied the charge distribution among the S atoms upon DBT adsorption by calculating the difference of Bader charge (ΔC) between the S atom from DBT (S_C) and the two adjacent S atoms (S_L and S_R) from the MoS_2 nanosheet ((S_L+S_R)/2 - S_C). Fig. 4.8d represents the plotted ΔC as a function of E_b. Note that ΔC is above zero, which refers to more charge migration towards S_L and S_R. Similar to ΔG_2, ΔC decreases first, then increases with respect to E_b. The decrease in ΔC indicates that less charge is transferred towards S_L and S_R, suggesting that there is a more comparable charge distribution among the S atoms. In contrast, the increase in ΔC at relatively high E_b means more charge migration towards S_L and S_R. This indicates a weak binding strength between the TM atoms and S_C, thus leading to an increase of ΔG_2. The 4*d* TM promoters, generally, result in a low ΔG_2 at high E_b, which can be simply related to a strong TM-S bonding strength. The 5*d* TM promoters tend to have a consistent ΔG_2.

The ΔG_3 in Fig. 4.8c represents the reaction energy required to produce BP and regenerate TM-MoS_2 by refilling the V_S@Cen site with the S atom from DBT. As E_b increases, ΔG_3 decreases, which means less energy is required to refill the V_S@Cen site. In fact, the negative ΔG_3 indicates a spontaneous reaction. A higher E_b indicates a stronger binding strength between the TM and the S atoms and therefore, leads to a relatively easier refilling of the V_S@Cen site.

For a clear comparison, the corresponding ΔG_1, ΔG_2, and ΔG_3 for the unpromoted MoS_2 nanosheet were also calculated, shown by the dashed lines in Fig. 4.8a, b, and c, respectively. Here, the V_S@Cen was modeled by removing one sulfur atom from the sulfur dimer located at the center of the edge of the unpromoted nanosheet, as in the case of TM-promoted MoS_2. It is clear that step (1) occurs spontaneously, as indicated by the negative values of ΔG_1. The TM promotion improves the refilling of the V_S@Cen site in step (3) for most of the TM atoms, as indicated by the lower value of ΔG_3 compared to the unpromoted nanosheet. Finally, the relatively high value of ΔG_2 for the unpromoted MoS_2 indicate that most of the TM promoters cause stronger adsorption of DBT than the unpromoted one, emphasizing the improvement of the HDS activity by TM promotion.

As mentioned above, the HDS process is composed of three consequent steps, which involves three parameters, ΔG_1, ΔG_2, and ΔG_3. The ΔG_1 describes the energy required for the formation of V_S@Cen and thus, a lower ΔG_1 is desirable for step (1). The ΔG_2 evaluates the tendency to adsorb DBT *via* the V_S@Cen site and thus, a lower ΔG_2 is desirable for step (2). The ΔG_3 means the reaction energy required to refill the V_S@Cen site and produce BP and thus, a lower ΔG_3 is desirable for step (3). It is worth mentioning that the total change of free energies ($\Delta G = \Delta G_1 + \Delta G_2 + \Delta G_3$) in all three steps is about -0.60 eV, which does not depend on the choice of TM promoters. However, by combining the three steps and the trends of the three parameters as E_b, we are able to conclude that the an ideal TM promoter should neither be extremely high or extremely low E_b for its corresponding TM sulfides. This is also consistent with the Sabatier principle, that is, the interaction between the catalyst and the substrate should neither be too strong nor too weak.[104, 82] In other words, the E_b can be considered as one effective descriptor for selecting TM promoters. On the basis of this descriptor, we are able to identify several promising TM promoters including 3*d* elements Mn, Cr, Co, Fe, Ni, and V, 4*d* element Ru, and 5*d* element Pt for enhancing the catalytic performance in the HDS process, with neither too strong nor too weak bonding interaction with S, as shown in Fig. 4.8. This is in good agreement with prior experimental findings that highlight the potential of 3*d* elements Cr,[91, 147] Mn,[99] Fe[91], Co[121, 107, 160, 101] and Ni,[101, 69, 11] 4*d* element Ru[29] as promoters of MoS_2 catalysts for HDS reaction. Interestingly, recent studies also indicate that the 3*d* element V[35] or 5*d* element Pt[118] can be appropriate promoters for improving catalytic activity of MoS_2 in the oxygen reduction reaction and hydrogen evolution reaction, respectively, which is consistent with our prediction.

4.4 Conclusions

In summary, we have studied the TM promotion effects on the HDS activity of MoS_2 nanocatalysts using first-principles density functional theory calculations. Our theoretical finding reveals that TM atoms are promoted on the edges of the hexagonal MoS_2 nanosheets under sulfur saturating conditions, with an exception of Ag and Au. As indicated by the negative binding energies, the TM atoms are unable to be attached on the nanosheets without the sulfur saturations. Moreover, the calculated formation energies of sulfur vacancy decrease with the TM promoters from group 3 to group 12 in the periodic table. This can directly relate to the decrease in the binding strength between the TM and S atoms, which is represented by the binding energy (E_b) of the TM-sulfides. By modeling the three subindividual steps in the HDS process with a DBT molecule, we calculated the Gibbs free energies for each step and revealed that E_b can be an effective descriptor for the rightful selections of the TM promoters. That is, an ideal TM promoter should have neither extremely low nor extremely high E_b for its corresponding TM-sulfide. On the basis of this finding, our thermochemical results show several promising TM promoters including 3*d* elements Mn, Cr, Co, Fe, Ni, and V, 4*d* element Ru, and 5*d* element Pt to enhance the catalytic performance.This work, therefore, provides a useful guidance to the design of high-performance MoS_2-based nanocatalysts.

4.5 Acknowledgment

Chapter 4, in full, is currently being submitted for publication of the material ”Descriptors of Transition Metal Promoters on MoS_2 Nanocatalysts for Hydrodesulfurization: Binding Energy of Metal Sulfides from First Principles”. Paul H. Joo, Kesong Yang. The dissertation author is the primary investigator and author of this paper.

Chapter 5

Energetic Stability, Oxidation States, and Electronic Structure of Bi-doped NaTaO$_3$: First-Principles Hybrid Functional Study

In this chapter, we discuss the defect formation energies, oxidation states of the dopants, and electronic structures of Bi-doped NaTaO$_3$ used for photocatalytic water splitting purpose. Three possible structural models, including Bi-doped NaTaO$_3$ with Bi at the Na site (Bi@Na), with Bi at the Ta site (Bi@Ta), and with Bi at both Na and Ta sites [Bi@(Na,Ta)], are constructed. Our results show that the preferred doping sites of Bi are strongly related to the preparation conditions of NaTaO$_3$. It is energetically more favorable to form a Bi@Na structure under Na-poor conditions, to form a Bi@Ta structure under Na-rich conditions, and to form a Bi@(Na,Ta) structure under mildly Na-rich conditions. The Bi@Na doped model shows an n-type conducting character along with an expected blueshift of the optical absorption edge, in which the Bi atoms exist as Bi^{3+} (6s^{2}6p^0). The Bi@Ta doped model has empty gap states consisting of Bi 6s states in its band gap, which can lead to visible-light absorption via the electron transition among the valence band, the conduction band, and the gap states. The Bi dopant is present as a Bi^{5+}

ion in this model, consistent with the experimental results. In contrast, the Bi@(Na,Ta) doped model has occupied gap states consisting of Bi 6s states in its band gap, and thus visible-light absorption is also expected in this system due to electron excitation from these occupied states to the conduction band, in which the Bi dopants exist as Bi^{3+} ions. Our first-principles electronic structure calculations revealed the relationship between the Bi doping sites and the material preparation conditions, and clarified the oxidation states of Bi dopants in $NaTaO_3$ as well as the origin of different visible-light photocatalytic hydrogen evolution behaviors in Bi@Ta and Bi@(Na,Ta) doped $NaTaO_3$. This work can provide a useful reference for preparing a Bi-doped $NaTaO_3$ photocatalyst with desired doping sites.

5.1 Introduction

Recently, perovskite oxide materials (ABO_3) have received increasing attention because of their potential applications for highly efficient water splitting.[13, 131, 126] Among perovskite oxide semiconductors, alkaline tantalum oxide $NaTaO_3$ has been a focus of research interests mainly due to its ultra high photocatalytic efficiency and environmental friendliness.[57, 74, 141, 36, 148, 40, 26, 76, 55, 158, 159, 73, 42, 75, 157, 103, 53, 55, 138, 84] For example, Kato *et al.* reported a maximum quantum efficiency of 56% under the ultraviolet light (270 nm) in the La-doped $NaTaO_3$ with NiO cocatalyst, which, so far, has been the highest record of the quantum yield for the direct photocatalytic water splitting.[57] After that, encouraged by this milestone work, a number of experimental efforts have been made mainly based on two major considerations, that is, either to explore various materials preparation approaches to simplify the synthesis of $NaTaO_3$[74, 36, 148, 40, 26, 76] or to improve its visible-light quantum efficiency *via* doping.[158, 159, 73, 42, 75, 157, 55, 103]

In terms of the materials preparation, it is found that the crystalline structure is very sensitive to the synthetic route. For instance, the conventional solid-state synthesis and sol-gel synthesis were both widely used to prepare $NaTaO_3$-based photocatalysts. The solid-state method that requires a high operating temperature leads to an orthorhombic crystalline structure with a direct band gap, while the sol-gel method that can be operated under low temperature leads to a monoclinic crystalline structure with an indirect band gap.[74, 76] In addition to the solid-state and sol-gel methods, the hydrothermal process can also be used to prepare the $NaTaO_3$-based photocatalysts.[26, 76] Regarding the improvement of the visible-light quantum efficiency *via* doping, a number of experimental and theoretical efforts have been made to explore the doping effects on the visible-light photocatalyitc activity. For example, the alkaline earth metal doping[42] and La doping[57] were found to be capable of promoting the crystallinity by reducing the crystal size, which leads to a high photocatalytic activity because of the reduction of the defects in the crystal and thus the high electron-hole separation rate. The solid solutions of $Na_{1-x}La_xTa_{1-x}Co_xO_3$ and $Na_{1-x}La_xTa_{1-x}Cr_xO_3$ prepared from the $NaTaO_3$ and $LaCoO_3$[158] or $LaCrO_3$[159] had a tuned band gap with changing x values and exhibited water splitting ability under visible-light irradiation. Ahuja *et al.* studied the anion (N, S, C, and P) doping influence on the electronic properties of $NaTaO_3$ from first-principles analysis.[138] The possibility of narrowing the band gap via anion-cation co-doping such as (N, Mo) and (N, Cr) doping were also explored from electronic structure calculation.[84]

Recently, Bi-based oxides such as $NaBiO_3$,[51] Bi_2O_3,[47] and $BiVO_4$[72, 135]have shown great potential as visible-light photocatalysts because of their narrow band gap.[34] Consequently, one may speculate that Bi doping can be an effective approach to narrow the band gap to promote the visible-light photocatalytic activity of $NaTaO_3$. Another reason for choosing Bi as dopants is due to its d^{10} configuration. The underlying mechanism is that the photoexcited electron transitions by the visible-light involve delocalized 6*s* and 6*p* orbitals rather than localized 5*d* orbitals, and thus photoinduced carriers (electrons and holes) in the 6*s* or 6*p* bands have high mobility, which facilitates the electron-hole separation and promotes the photocatalytic activity. Indeed, some experimental work has been done to explore Bi doping influence on the visible-light photocatalytic activity of $NaTaO_3$.[55, 73, 103, 56, 54] However, the optical property and photocatalytic performance of Bi-doped $NaTaO_3$ were found to be very sensitive to the Bi oxidation states and the preparation conditions of the samples.[55, 56] Cui *et al.* reported that the Bi^{3+} doping did not promote the photocatalytic activity of $NaTaO_3$, while Bi^{5+} and Bi^{3+} doping did. In principle, materials preparation conditions determine Bi doping sites in $NaTaO_3$, *i.e.*, Bi at Na, Bi at Ta, or Bi at both Na and Ta sites, and the resulting Bi oxidation states, which further influence the electronic structures and the optical absorption properties. For instance, Chen *et al.* found that the Bi-doped $NaTaO_3$ sample did not show visible-light absorption under Na-poor condition but did so under Na-rich condition and under mildly Na-rich condition.[55] More surprisingly, Kanhere *et al.* found that the prepared Bi-doped $NaTaO_3$ sample under the mildly Na-rich condition shows enhanced photocatalytic hydrogen evolution under the visible-light irradiation while the sample under the Na-rich condition does not, though both of them show a visible-light absorption.[56] So far, there has been no convincing explanations for such a phenomenon. In principle, the preferred doping sites can be predicted from the formation energy for each structure, which is often correlated to the chemical potential of some element such as oxygen. The chemical potential range of the element can be used as an important reference to control the material preparation condition. Nevertheless, there has been little work on the systematic studies of the energetic stability of the various types of Bi-doped $NaTaO_3$ as a relationship of the materials preparation conditions.

In addition, although the oxidation state and chemical environment of the Bi ions in the doped samples can be partially evaluated from the X-ray photoemission (XPS) spectra, a conclusive conclusion of the actual oxide state of the dopant cannot be obtained because the binding energies of Bi^{3+} and Bi^{5+} are too close.[27] For example, Kanhere *et al.* claimed that their XPS analysis could not conclusively confirm the presence of Bi^{5+} ions in the Bi-doped $NaTaO_3$,[55] though in principle, Bi could be doped in the lattice either in Bi^{3+} or Bi^{5+} oxidation states. Actually, similar case also occurs in Cr-doped TiO_2 in which the Cr^{3+} and Cr^{4+}

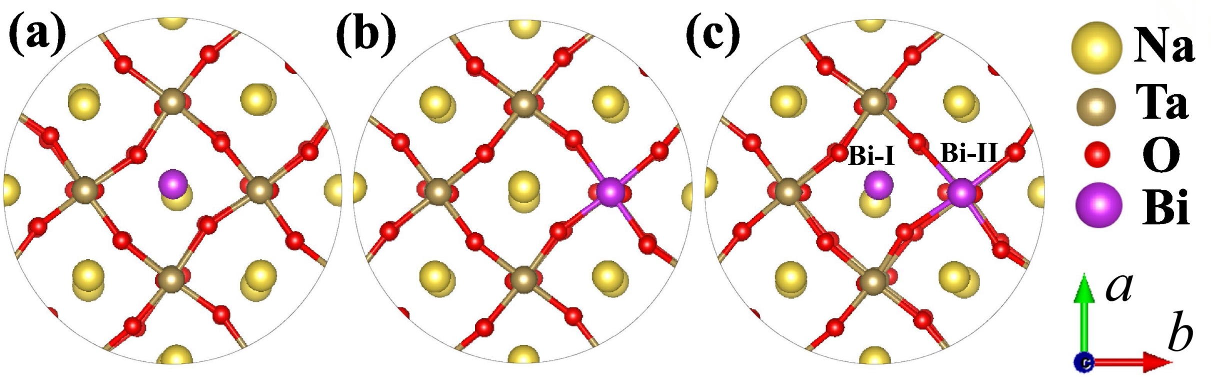

Figure 5.1: Local geometrical structures of $NaTaO_3$ with substitutional doping of Bi ion at (a) Na site (Bi@Na), (b) Ta-site (Bi@Ta), and two Bi ions at (c) both Na and Ta sites [Bi@(Na,Ta)] simultaneously.

cannot be accurately distinguished from XPS measurement.[153] In this regard, a comprehensive understanding of the relationship between the Bi doping sites and the materials preparation condition as well as the oxidation states of Bi dopants are essentially required.

In this chapter, using first-principles hybrid density functional theory calculations, we studied the defect formation energies, dopant oxidation states, and electronic properties of Bi-doped $NaTaO_3$ by modeling three possible structural models. The stability of the the compound, oxidation states of Bi dopants, and its doping sites are found to strongly depend on the materials preparation conditions, *i.e.*, Na-poor, Na-rich, and mildly Na-rich conditions. The chemical potential range of oxygen corresponding to the preferred Bi doping sites are revealed. In each doped structure, the oxidation states, relative band edge positions, qualitative photocatalytic ability, and the optical properties are discussed.

5.2 Computational and Structural Details

The crystal structure of a pristine $NaTaO_3$ at room temperature has as an orthorhombic structure (space group no. 62, *Pnma*) with experimental lattice constants a = 5.484 Å, b = 5.521 Å, and c = 7.795 Å.[1] In this work, the estimated equilibrium lattice parameters within the

GGA-PBE framework are a = 5.474 Å, b = 5.590 Å, and c = 7.887 Å, which are in a good agreement with the experimental values. In this work, we used a 80-atom $2 \times 2 \times 1$ supercell to model substitutional Bi-doped $NaTaO_3$. The structure of Bi-doped $NaTaO_3$ with Bi at the Na site (hereafter referred to as Bi@Na) was modeled by replacing one Na atom with one Bi atom. Similarly, the structure of Bi-doped $NaTaO_3$ with Bi at the Ta-site (hereafter referred to as Bi@Ta) was constructed by replacing one Ta atom with one Bi atom. It is noted that from symmetry analysis of the pristine $NaTaO_3$ crystal, all the Na (Ta) sites are equivalent in the unit and supercell model. This means that substituting any one Na (Ta) atom using one Bi atom in the supercell model is equivalent. In other words, there exist unique Bi@Na (Bi@Ta) doping model. For the Bi-doped $NaTaO_3$ system with Bi at both Na- and Ta-site (hereafter referred to as Bi@(Na,Ta)), considering that the dopants often have a tendency to form a cluster,[155] we modeled the structure by replacing the adjacent Na and Ta atoms simultaneously using two Bi atoms. For convenience, the first Bi atom at Na site is labeled as Bi-I and the second Bi atom at Ta site is labeled as Bi-II. The local geometrical structures of the three substitutional Bi-doped models are shown in Figure 5.1.

The calculated band gap of primitive $NaTaO_3$ is 2.67 eV from the standard DFT calculations, fairly consistent with the prior calculated value of 2.65 eV.[53] Nevertheless, this band gap is much underestimated compared to the experimental value of 4.1 eV,[84, 58, 98] which is mainly because of the well-known shortcoming of the GGA functional that cannot accurately describe the electron correlation and exchange effects.[48] To reproduce the accurate experimental band gap, we carried out hybrid functional calculations in which the percent contribution of the Hartree-Fock (HF) exchange was tuned for matching the calculated values with experimental ones. To do this, we performed hybrid functional calculations with the HF contribution tuned to 0 (a standard DFT calculation), 10%, 20%, 30%, and 40%. Although not shown here, the calculated electronic band gaps with respect to varying percent HF contribution explicitly shows that the calculated band gaps exhibit a linear relationship with the percentage contributions of the HF exchange. This relationship actually applies to a wide range of semiconductors and insulators.[3, 4, 111] Based on this finding, we concluded that the ideal HF percentage contribution of 26% can reproduce the experimental band gap of 4.1 eV for pristine $NaTaO_3$.[84, 58] This is comparable to previously calculated band gap value of 4.0 eV with 25% HF contribution.[53] In the following calculations, the 26% HF percentage contribution is employed for the pristine and Bi-doped $NaTaO_3$ systems.

First-principles Density Functional Theory (DFT) electronic structure calculations were carried out using the Vienna *Ab-initio* Simulation Package (VASP).[62, 61] Our calculations employed Projector-Augmented Wave (PAW)[7] potentials for treating electron-ion interactions and Generalized Gradient Approximation (GGA) parameterized by Perdew-Burke-Ernzerhof (PBE) for electron exchange-correlation functional.[97] The cut-off energy of 700 eV and $2 \times 2 \times 3$ k-point mesh centered at the Γ point were used. The cell parameters and atomic positions of the doped systems were fully relaxed until all components of the remaining forces were less than 0.01 eV/Å. The tetrahedron method with Blöchl corrections was employed to determine the accurate density of states (DOS) and the convergence tolerance for the self-consistent energy was set to 10^{-4} eV. To account for the DFT underestimation of the band gap, the Heyd-Scuseria-Ernzerhof (HSE06) hybrid functional[**?**] was employed to correctly reproduce the electronic band structure of $NaTaO_3$, in which the screening parameter value was fixed as 0.2 $Å^{-1}$.

5.3 Results and discussion

5.3.1 Defect Formation Energy

To evaluate the relative structural stability of the three substitutional Bi-doped $NaTaO_3$ systems, we calculated their formation energies. The defect formation energy required for Bi@Na and Bi@Ta doping could be calculated from the following formulas, respectively.

$$E_f = E_{doped} - E_{undoped} - \mu_{Bi} + \mu_{Na} \tag{5.1}$$

$$E_f = E_{doped} - E_{undoped} - \mu_{Bi} + \mu_{Ta} \tag{5.2}$$

E_{doped} refers to the total energy of the Bi-doped $NaTaO_3$ supercell, $E_{undoped}$ the total energy of the undoped supercell, μ_{Na} (μ_{Ta}) the chemical potential of the Na (Ta) atom, and μ_{Bi} the chemical potential of Bi. For the Bi@(Na,Ta) doped $NaTaO_3$ system, its defect formation energy is defined as below:

$$E_f = E_{doped} - E_{undoped} - 2\mu_{Bi} + \mu_{Na} + \mu_{Ta} \tag{5.3}$$

in which the factor 2 of μ_{Bi} means two Bi ions replacing one Na and one Ta ion in the system.

The chemical potentials, μ_{Na} and μ_{Ta}, depend on whether $NaTaO_3$ is prepared under Na-rich (Ta-poor) or Ta-rich (Na-poor) growth conditions.[55, 56] Under Na-rich (Ta-poor) condition, the chemical potential of Na is obtained from the energy of bulk Na metal (E_{Na}) while the Ta chemical potential is obtained from the growth condition:

$$\mu_{Na} + \mu_{Ta} + 3\mu_O = E_{NaTaO_3} \tag{5.4}$$

Herein, the oxygen chemical potential, μ_O, was calculated from the ground-state energy of O_2 molecule ($\frac{1}{2}E_{O_2}$), and E_{NaTaO_3} refers to the total energy of the $NaTaO_3$ unit cell. This is based on the assumption that doped $NaTaO_3$ material system was prepared under O-rich condition because it is a general trend that the substitutional cation doping is thermodynamically more favorable under O-rich growth condition than under O-poor growth condition.[154, 150, 151, 152] Accordingly, μ_{Bi} was calculated by the stability of Bi_2O_3, $2\mu_{Bi} + 3\mu_O = E_{Bi_2O_3}$, under the O-rich condition. In other words, the chemical potential range of Bi is bounded by the material growth condition of Bi_2O_3. In fact, Reddy *et al.* has reported that Bi doping into $NaTaO_3$ could form a secondary phase compound, Bi_2O_3, from X-ray diffraction analysis.[103] In light of the experimental preparation condition of the $NaTaO_3$, we divided the materials preparation conditions into two extreme cases, that is, Na-rich (Ta-poor) and Na-poor (Ta-rich) conditions.

Under Na-rich (Ta-poor) condition, μ_{Na} is calculated from the total energy of the most stable low-temperature phase of bulk Na-metal (E_{Na}), while μ_{Ta} is then calculated from equation (4). Similarly, we use the same procedure to obtain the μ_{Na} and μ_{Ta} under Na-poor (Ta-rich) condition. It is worth mentioning that Na and Ta are host ions of the $NaTaO_3$, and thus their chemical potential ranges are bounded by equation (4) instead of other Na and Ta oxides. The chemical potential references of Na, Ta, and O are defined using following equations:

$$\Delta\mu_{Na} = \mu_{Na} - E_{Na} \tag{5.5}$$

$$\Delta\mu_{Ta} = \mu_{Ta} - E_{Ta} \tag{5.6}$$

$$\Delta\mu_{O} = \mu_{O} - \frac{1}{2}E_{O_2} \tag{5.7}$$

The extreme Na-rich condition is characterized by $\Delta\mu_{Na}$=0, that is, $\mu_{Na} = E_{Na}$; the extreme Ta-rich (Na-poor) condition $\Delta\mu_{Ta}$=0, that is, $\mu_{Ta} = E_{Ta}$; and the O-rich condition $\Delta\mu_{O}$=0. The formation enthalpy of $NaTaO_3$ is defined as:

$$\Delta H_f(NaTaO_3) = E_{NaTaO_3} - E_{Na} - E_{Ta} - \frac{3}{2}E_{O_2} \tag{5.8}$$

which can be also written as below using the above definitions:

$$\Delta H_f(NaTaO_3) = \Delta\mu_{Na} + \Delta\mu_{Ta} + 3\Delta\mu_{O} \tag{5.9}$$

Our calculated formation enthalpy of $NaTaO_3$ is -2.37 eV/atom from the HSE calculation and -2.66 eV/atom from the standard DFT calculation within PBE functional. The later is more consistent with the experimental value of -2.86 eV under standard thermodynamic state.[105] However, previous theoretical work indicates that the hybrid functional approach can give more accurate results of the defect formation energies than the standard DFT calculations.[44, 3] As

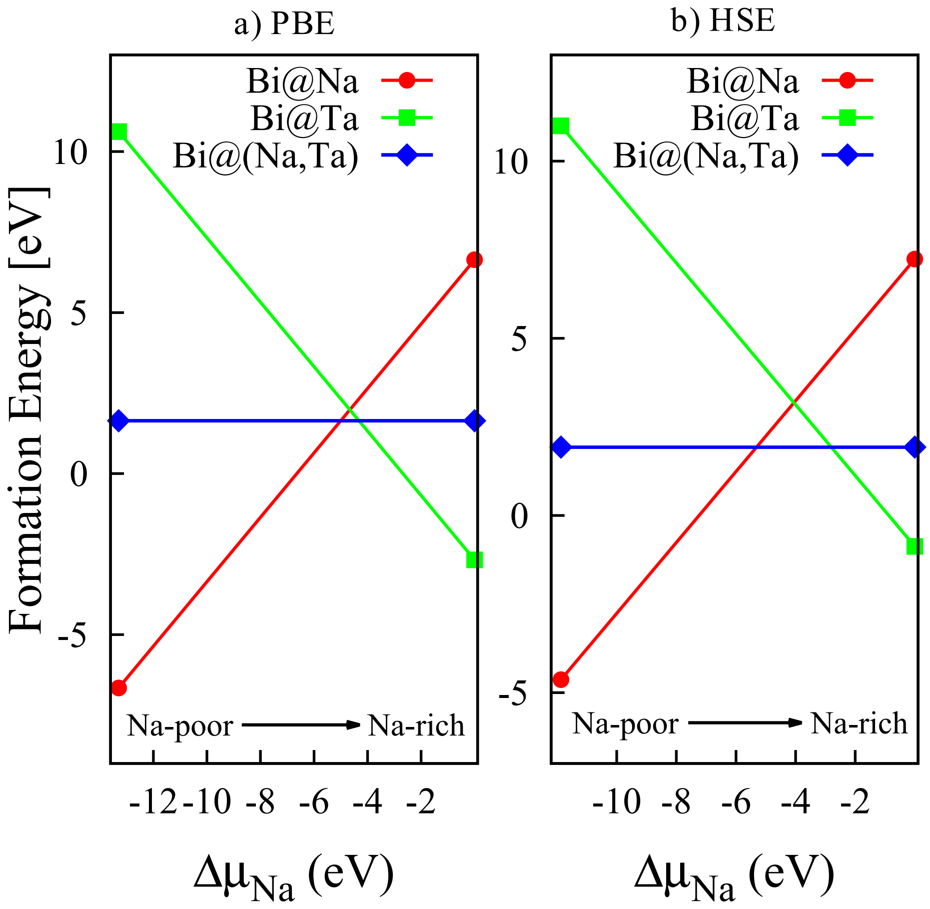

Figure 5.2: (Color online) Calculated formation energies of Bi@Na, Bi@Ta, and Bi@(Na,Ta) doped $NaTaO_3$ with respect to $\Delta\mu_{Na}$ within DFT-PBE (a) and HSE (b) approach.

a result, one speculates that similar case may also occur in Bi-doped $NaTaO_3$. To verify this assumption, we calculated the formation energies of three Bi-doped models as a function of $\Delta\mu_{Na}$ using the standard DFT-PBE calculation and HSE calculation, respectively, which are shown in Figure 5.2a and 5.2b. The two methods give similar trend of the formation energy for Bi@Na and Bi@Ta doped models despite the slight difference of the absolute values, while the relative formation energy of Bi@(Na, Ta) doped model with respect to the other two models are significantly different. The standard DFT-PBE results show that it is nearly impossible to form Bi@(Na, Ta) doped model because of the extremely narrow range of $\Delta\mu_{Na}$. In contrast, the HSE results do show that at an appropriate range of $\Delta\mu_{Na}$ (-5.5 eV $< \Delta\mu_{Na} <$ -3.0 eV), the Bi@(Na, Ta) model has lower formation energy than that of the other two models, implying that the Bi@(Na, Ta) structure is energetically preferred within this chemical potential range. As discussed below, the calculated formation energy trend from the HSE method is more consistent with the experiments than that from the standard DFT-PBE method. Actually, a prior report on oxygen vacancy in TiO_2 also shows that HSE calculation can produce the defect formation energy with better consistency with the experimental results than the standard DFT-PBE calculations.[44] From the trend of the HSE-calculated formation energy with respect to $\Delta\mu_{Na}$, we found the following conclusions:

(1) Under Na-poor growth condition, the formation energy of substitutional Bi@Na doped $NaTaO_3$ is much lower than that of the Bi@Ta model, indicating that it is thermodynamically preferable for Bi to occupy the Na site rather than Ta site. Moreover, the defect formation energy of the Bi@Na structure is negative under the Na-poor condition, implying that the formation of Bi@Na structure is thermodynamically spontaneous.

(2) Under Na-rich growth condition, the formation energy of substitutional Bi@Ta doped $NaTaO_3$ is lower than that of the Bi@Na structure, indicating that it is thermodynamically more favorable for Bi to occupy the Ta site rather than the Na site.

(3) Under mildly Na-rich condition, the formation energy of Bi@(Na,Ta) doped $NaTaO_3$ is relatively lower than that of the Bi@Na and Bi@Ta model, implying that it is thermodynamically more favorable for Bi to occupy at both the Na- and Ta-site.

Our calculated formation energy within HSE framework are well consistent with the previous experimental conclusions by Kanhere *et al.*[55, 56] They found that, under Na-deficient condition, Bi ions predominantly occupy the Na sites, while under Na-rich condition, Bi ions predominantly occupy the Ta sites , and under mildly Na-rich condition, Bi can occupy both the Na and Ta sites. These results suggest that the Bi doping sites can be well tuned by controlling the preparation conditions of $NaTaO_3$. Our results show that the calculated formation energy within HSE framework

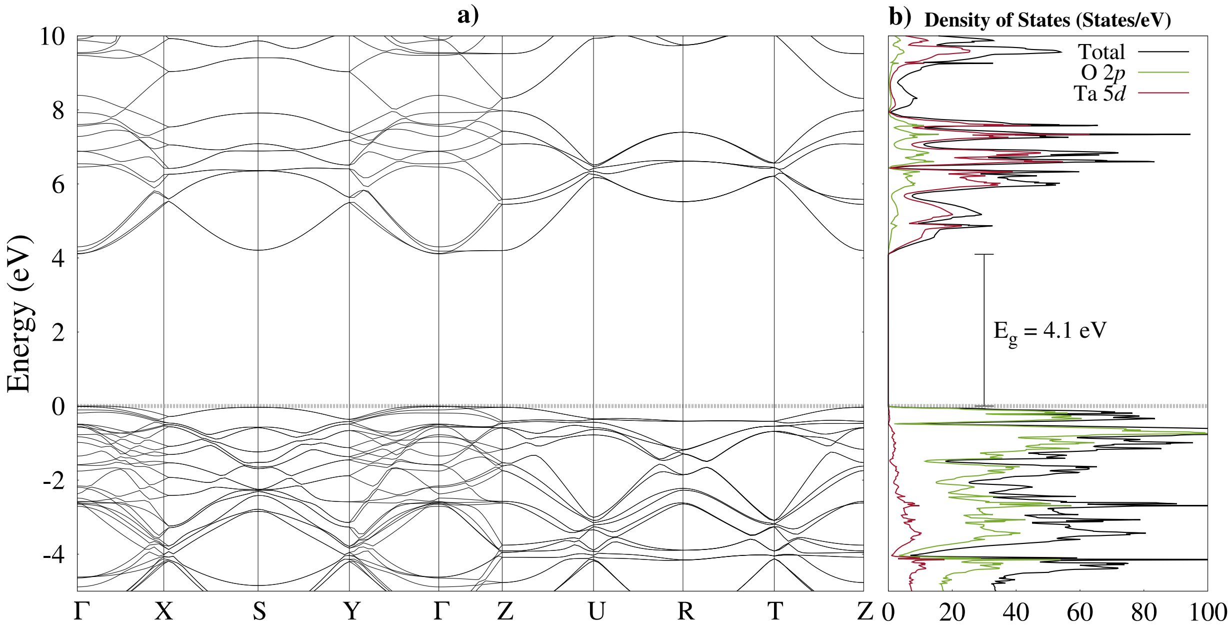

Figure 5.3: (Color online) Calculated (a) electronic band structure along the Brillouin Zone path of the orthorhombic lattice and (b) DOS plot of orthorhombic $NaTaO_3$. The zero point energy represents the valence band maximum.

5.3.2 Electronic Structure and Oxidation States

The calculated electronic band structure along the Brillouin Zone path of the orthorhombic lattice (ORC) and DOS plot of pristine $NaTaO_3$ are shown in Figure 5.3a and 5.3b, respectively. It shows that the Conduction Band Minimum (CBM) and Valence Band Maximum (VBM) are both located at the Γ-point with a band gap of 4.1 eV, indicating a direct band-gap character, which is consistent with the experimental diffuse reflectance UV-vis spectroscopic analysis.[40] The calculated DOS plot displays that the conduction band consists largely of Ta 5*d* states, while the valence band is composed primarily of O 2*p* states, indicating a strong ionic bond character of the Ta-O bond.

Next, we studied the electronic properties of various Bi-doped $NaTaO_3$ systems. For Bi@Na doped $NaTaO_3$ system, the calculated partial DOS and total DOS plots are shown in Figure 5.4a and 5.4b, respectively. The total DOS plot shows that no impurity states appear within the band gap, and the Fermi level lies within the conduction band, indicating an *n*-type conducting character. The calculated partial DOS shows that the majority of Bi 6*p* states lie within the conduction band, while the Bi 6*s* states almost entirely locate within the valence band, implying that the Bi dopant has an electron configuration like that of a Bi^{3+} ($6s^2 6p^0$) at the Na site. This conclusion is well consistent with the recent experimental characterization of the chemical state of Bi in $NaTaO_3$ by X-ray photoelectron spectroscopy (XPS) measurements,[41, 55, 54] in which the chemical state of Bi ions at the Na sites were found to be $3+$. Hence, the Bi^{3+} will release two more electrons into the system than the Na^+ and thus producing the *n*-type conductivity, which is in a good agreement with the experimental *n*-type conducting character in Bi@Na doped $NaTaO_3$ *via* photoelectrochemical measurement.[103] The two additional electrons occupy the lowest conduction band states below the Fermi level, and thus the electron excitation with coincidental optical absorption must occur from the valence band states to higher conduction band states above the Fermi level due to the Pauli blocking principle. Consequently, this effect will lead to a widening of the optical band gap, which is known as the Burstein-Moss shift.[10, 14] The calculated total DOS of the Bi@Na doped model shows that the effective optical band gap is about 4.37 eV, larger than that of the undoped system of 4.1 eV. The widened optical band gap implies that there will exist a blueshift of the optical absorption edge in the Bi@Na doped $NaTaO_3$ system. This is similar to the case of B-doped TiO_2 system in which the interstitial B doping leads to a widened optical band gap and the resulting blueshift of the optical absorption edge.[50, 15, 149] However, it is worth mentioning that, in the experiments, the Bi@Na doped $NaTaO_3$ was found to show a redshift of the optical absorption edge,[103, 55, 54, 56, 41] which is probably because of the formation of some secondary phase compounds with lower optical band gap such as Bi_2O_3 (2.8 eV).[103, 56] Actually, as previously mentioned, the formation of the secondary phase, Bi_2O_3, has been proven experimentally.[103]

For Bi@Ta doped $NaTaO_3$ system, its calculated partial DOS and total DOS plots are shown in Figure 5.5a and 5.5b, respectively. Its band gap is about 4.0 eV, less than that of the

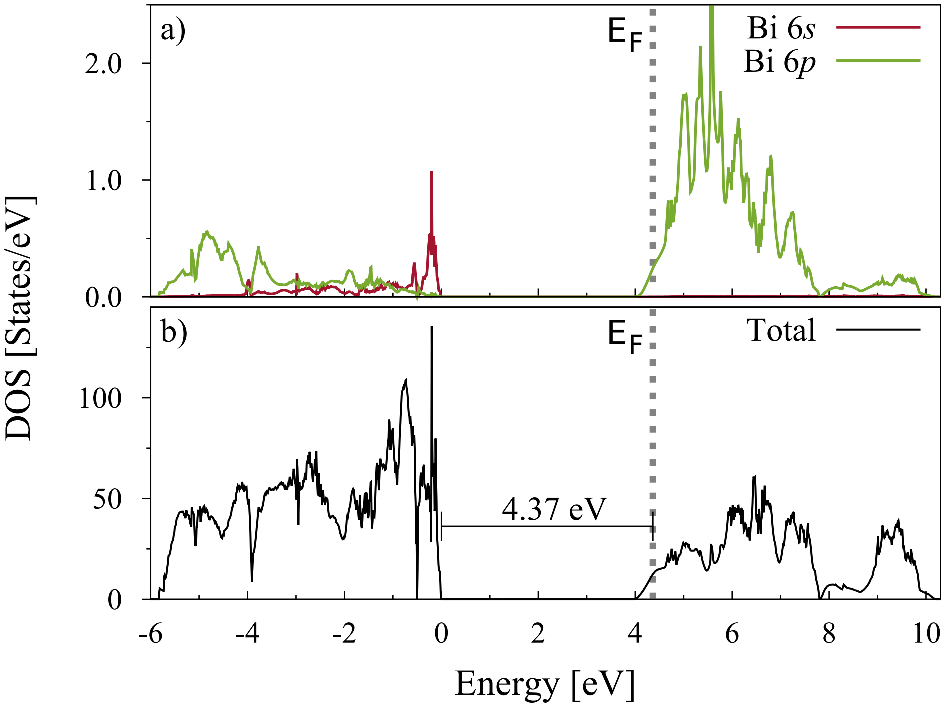

Figure 5.4: (Color online) Calculated (a) partial DOS and (b) total DOS of Bi@Na doped $NaTaO_3$. The vertical dashed line indicates the Fermi level in this and each subsequent DOS plot.

pristine $NaTaO_3$ system by 0.1 eV. Unlike the case of Bi@Na doped system, in the Bi@Ta doped system, the Fermi energy level lies in the band gap with no states crossing the Fermi level. Moreover, with respect to the pristine system, some unoccupied gap states are introduced in the band gap just below the conduction band bottom. The electron transition energy from the valence band to these gap states is about 2.62 eV, much less than that of the band gap of pristine $NaTaO_3$, thus leading to the visible-light absorption. The partial DOS plot shows that these gap states mainly consists of Bi 6*s* states, while the majority of Bi 6*p* states lie in the conduction band. This suggests that the Bi dopant should have an electron configuration like $6s^0 6p^0$, implying that the Bi exists as Bi^{5+} ion at the Ta site. This is consistent with the experimental binding energy measurement of Bi^{5+} in Bi@Ta doped $NaTaO_3$ from XPS analysis.[52]

Next, we considered the Bi@(Na,Ta) doped $NaTaO_3$ in which two Bi dopants replace Na and Ta simultaneously and respectively. Its calculated partial DOS of Bi-I (at Na-site), Bi-II (at

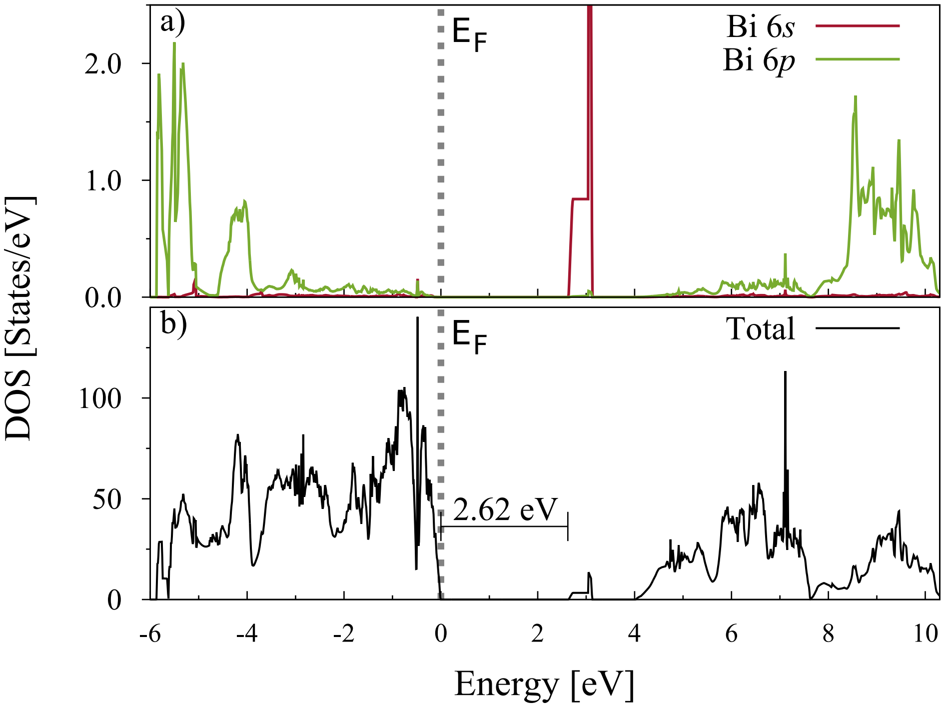

Figure 5.5: (Color online) Calculated (a) partial DOS and (b) total DOS of Bi@Ta doped $NaTaO_3$.

Ta-site), and total DOS are shown in Figure 5.6a, 5.6b, and 5.6c, respectively. Our results show that some occupied gap states are introduced in the band gap, which is above the valence band about 1.35 eV (Figure 5.6c). As a result, the corresponding electron transition energy from these occupied gap states to the conduction band is about 1.93 eV, less than the band gap of the pristine $NaTaO_3$ by 2.17 eV. As a result, it is expected that a significant redshift of the optical absorption edge would occur in the Bi@(Na,Ta) doped system. Actually, this is well consistent with the experimental visible light absorption spectra measurement, and it is found that the Bi@(Na,Ta) doping show stronger optical absorption than the other two doping cases, *i.e.*, Bi@Na, and Bi@Ta doping.[55, 52] In addition, the partial DOS of Bi-I shows similar characteristics with that of Bi@Na doped model. That is, the occupied Bi 6*s* states are located just above the VBM, and most of Bi 6*p* states are in the conduction band. Similarly, the partial DOS of Bi-II shows that the dominant Bi 6*p* orbitals are in the conduction band, while Bi 6*s* orbitals are occupied and located in the band gap. The main difference between the partial DOS of Bi-I and Bi-II are the

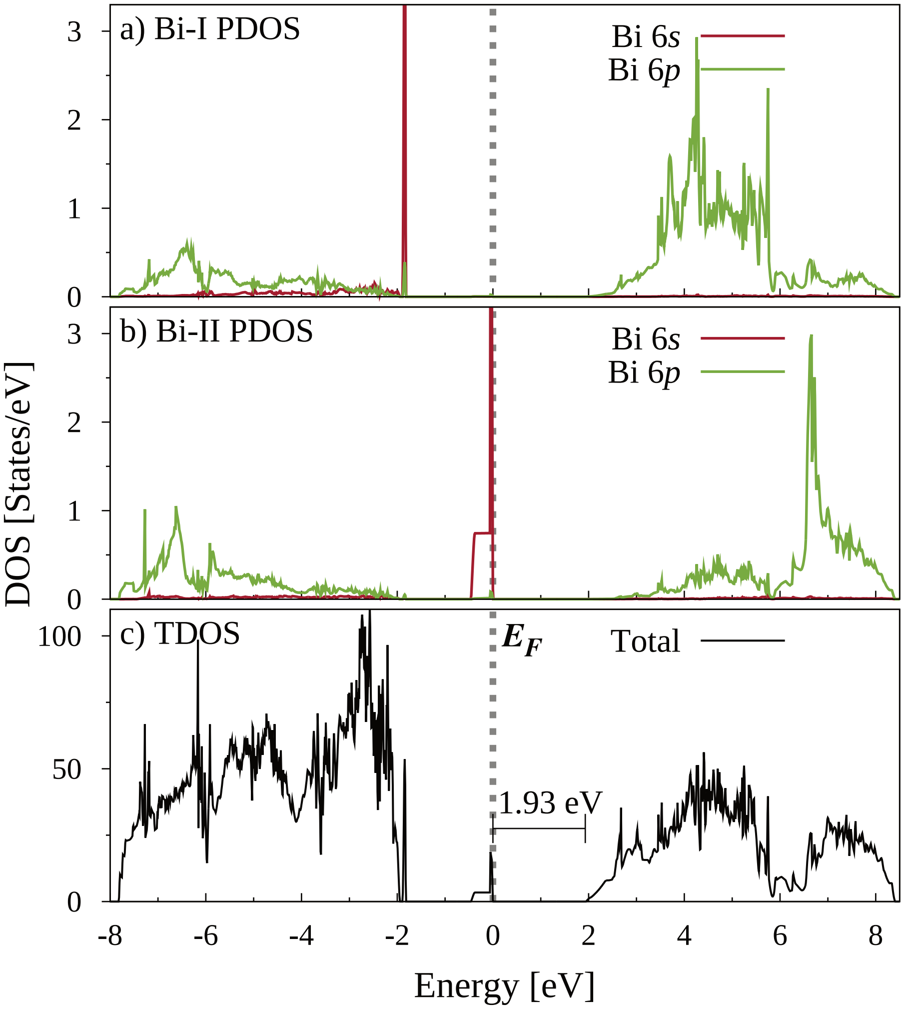

Figure 5.6: (Color online) Calculated (a) partial DOS of Bi-I (at Na-site), (b) Bi-II (at Ta-site), and (c) total DOS of Bi@(Na,Ta) doped $NaTaO_3$.

location of Bi 6*s* orbitals, though they are both below the Fermi level and occupied. These results indicate that the two Bi dopants have an electron configuration of $6s^2 6p^0$, and thus they exist as Bi^{3+} ions in the $NaTaO_3$ system. This is reasonable because the Bi@(Na,Ta) doped $NaTaO_3$ system can reach charge balance when two Bi^{3+} ions substitutes one Na^+ and one Ta^{5+} ions. This conclusion is well consistent with the experimental characterization of the chemical states of Bi ions for Bi@(Na,Ta) doped $NaTaO_3$.[55, 52]

In addition, we also considered Bi@(Na,Ta,Ta) doped $NaTaO_3$ in which three Bi dopants

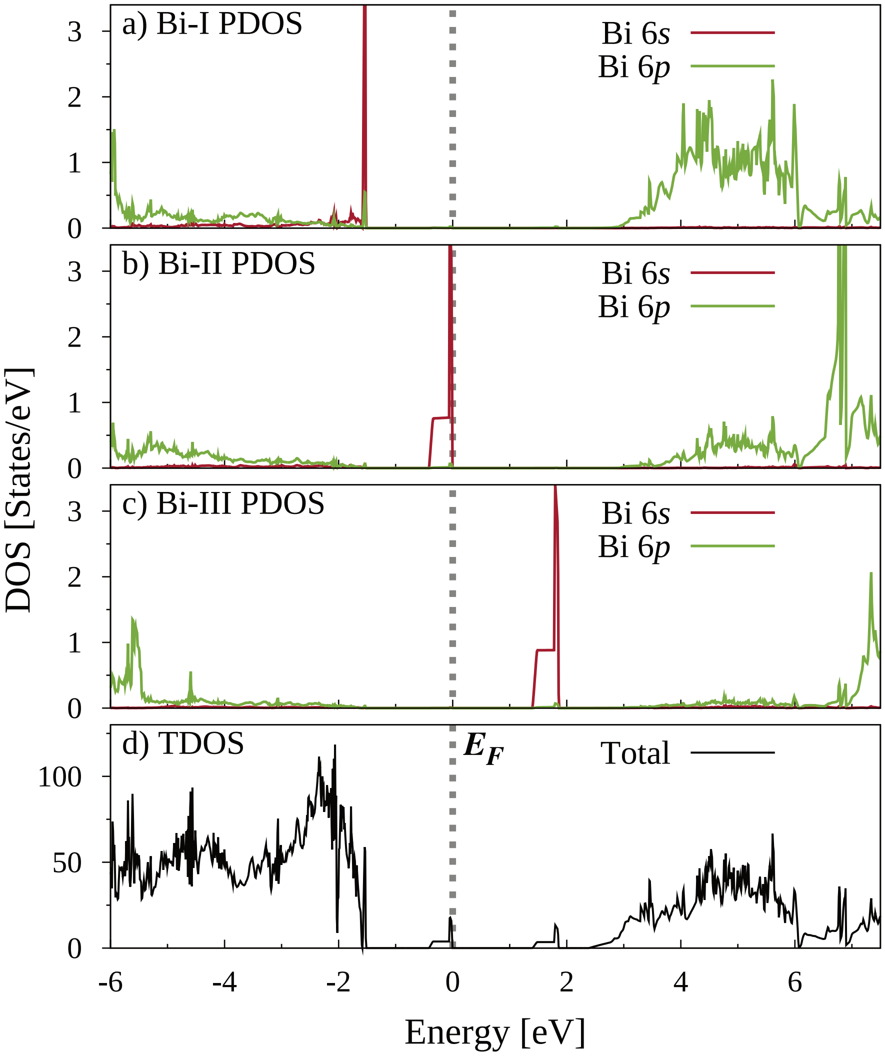

Figure 5.7: (Color online) Calculated (a) partial DOS of Bi-I (at Na-site), (b) Bi-II (at Ta-site), (c) Bi-III (at Ta-site), and (c) total DOS of Bi@(Na,Ta,Ta) doped $NaTaO_3$.

are introduced, and two Bi dopants (labeled as Bi-I and Bi-II as in the case of Bi@(Na,Ta) model) replace Na and Ta simultaneously, while the third one (Bi-III) replaces Ta atom. This is based on two following reasons. i) From our above analysis, the Bi dopants exhibit as Bi^{3+} in the Bi@(Na,Ta) doped model and Bi^{5+} in the Bi@Ta doped model. Hence, one can speculate that Bi^{3+} and Bi^{5+} ions may coexist in the $NaTaO_3$ if the Bi@(Na,Ta) and Bi@Ta models both exist. If this hypothesis is verified, then it can provide another explanation for the experimental uncertainty of the Bi dopants' oxidation states (+3 or +5).[27, 55] ii) In reality, it might be hard to realize an accurate control of the 1:1 ratio of the Bi dopants at Na sites to that at Ta sites, and the additional Bi dopants are likely to occupy the Ta site. Thus, modeling a Bi@(Na,Ta,Ta) doped $NaTaO_3$ can provide informative results for supporting experimental data analysis. The calculated partial DOS and total DOS plots of this model are shown in Figure 5.7. Figure 5.7a, 5.7b, and 5.7c represent the PDOS of Bi-I, Bi-II, and Bi-III, respectively. In the Bi@(Na,Ta,Ta) model, some occupied and unoccupied gap states consisting of Bi 6*s* are both introduced in the band gap, and they can be considered as a combination of the occupied states from the Bi@(Na,Ta) model (see Figure 5.6) and the unoccupied states from the Bi@Ta model (see Figure 5.4). This picture can be well depicted from their partial DOS plots. It is found that the partial DOS plots for the Bi-I and Bi-II in the Bi@(Na,Ta,Ta) model are similar to that in the Bi@(Na,Ta) model (see Figure 5.6a and 5.6b), indicating that these two Bi ions at Na and Ta sites exhibit as Bi^{3+}. Interestingly, the partial DOS of the Bi-III is similar to the case in the Bi@Ta doped model (see Figure 5.5a), implying that the Bi-III exists as Bi^{5+}. These results verified the proposed hypothesis above, which can clarify the experimental uncertainty on the oxidation states of Bi dopants in $NaTaO_3$. That is, in the Bi@(Na,Ta,Ta) doped $NaTaO_3$ model, the Bi^{3+} and Bi^{5+} ions both exist.

5.3.3 Photocatalytic Activity Evaluation

Besides the narrowed band gap, another important factor influencing the visible-light photocatalytic activity is the relative band edges of the semiconductor photocatalyst with respect to the water redox level. In principle, the VBM and CBM must be below and above the photo-oxidation and photo-reduction level, respectively, so that the photoinduced holes and electrons can be transferred to the absorbed species in a thermodynamically favorable fashion. Here, by aligning the O 2*s* orbital of the undoped and various Bi-doped $NaTaO_3$, we calculated their relative band edge positions in Figure 5.8. This is because O 2*s* orbital lies in the deep energy range, far away from the bonding states (valence band states) and less influenced by the atom bonding, and thus it can be used as the energy reference. The VBM and CBM positions of the undoped $NaTaO_3$ were taken from the experimental values measured from Mott-Schottky plot.[56] For undoped $NaTaO_3$, its CBM lies above the H^+/H_2O level about 1.19 eV, and its VBM lies below the O_2/H_2O level about 1.68 eV, implying that the $NaTaO_3$ has a strong oxidation and reduction capability. This may explain why the $NaTaO_3$ shows the higher photocatalytic efficiency under the ultraviolet light.[57, 74, 141, 36, 148, 40, 26, 76, 55, 158, 159, 73, 42, 75, 157, 103, 53, 55, 138, 84] For Bi@Na doped model, its VBM and CBM both lie below that of the undoped model, suggesting that this model has higher oxidation ability and lower reduction ability than the undoped model. However, its large band gap determines that it has no visible-light photocatalytic activity, which explains the experimental phenomenon why the Bi@Na doped $NaTaO_3$ cannot show photocatalytic hydrogen evolution under the visible-light irradiation.[56] For Bi@Ta doped model, as discussed above, some empty Bi 6*s* states appear in the band gap and below the H^+/H_2 level, and thus the excited electrons in these empty gap states by the visible light has no reduction ability. In other words, the Bi@Ta doped model can absorb the visible light by exciting the electron from the valence band to these empty gap states, but the electrons in these gap states will not lead to visible-light photocatalytic reaction. Interestingly, this conclusion is consistent with the experimental observation in the Bi@Ta doped $NaTaO_3$ sample in which the sample does not show any hydrogen evolution under the visible-light irradiation ($\lambda > 390$ nm).[56] For Bi@(Na, Ta) doped model, its VBM shifts towards H^+/H_2O level as compared to that of $NaTaO_3$, while its CBM has no significant changes; nevertheless, the Bi@(Na, Ta) doping introduces occupied Bi 6*s* states, which lies below the O_2/H_2O level. This indicates that the Bi@(Na, Ta) model may exhibit lower reduction ability, nearly similar oxidation ability, and meanwhile the visible-light photocatalytic activity because of the presence of the occupied gap states. This may be responsible for the enhanced photocatalytic hydrogen evolution under the visible light in the Bi@(Na, Ta) doped $NaTaO_3$ system.[56]

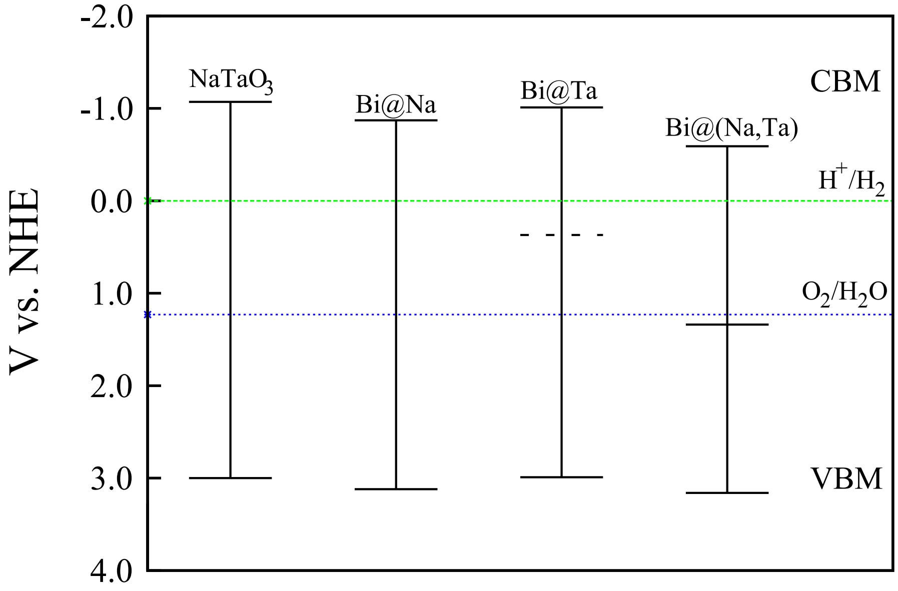

Figure 5.8: Comparison of the calculated VBM and CBM positions of the Bi-$NaTaO_3$ with that of the undoped $NaTaO_3$. The VBM and CBM values are given with respect to the normal hydrogen electrode (NHE) potential. The dashed and solid lines within the band gap in the Bi@Ta and Bi@(Na, Ta) doped models indicate the unoccupied and occupied gap states, respectively.

5.4 Conclusion

In summary, we constructed three possible Bi-doped $NaTaO_3$ models including Bi@Na, Bi@Ta, and Bi@(Na, Ta) doped structures, and studied their energetic stability, oxidation states, and electronic properties for each model from first-principles hybrid density functional theory calculations. Our results lead to the following conclusions:

(i) The preferred doping sites of Bi strongly depend on the preparation condition of $NaTaO_3$. It is energetically preferable to form the Bi@Na model under Na-poor condition, the Bi@Ta model under Na-rich condition, and the Bi@(Na, Ta) model under mildly Na-rich condition.

(ii) For Bi@Na doped $NaTaO_3$, the system exhibits an *n*-type conducting character with a blueshift of the optical absorption edge, in which the Bi atoms exist as Bi^{3+}.

(iii) For Bi@Ta doped $NaTaO_3$, some empty gap states consisting of Bi 6*s* orbitals appear in the band gap, and the electron transition among the valence band, conduction band, and the gap states is responsible for the visible-light absorption. The Bi dopant exist as Bi^{5+} ions in this structural model.

(iv) For Bi@(Na, Ta) doped $NaTaO_3$, unlike the Bi@Ta doped model, some occupied states consisting of Bi 6*s* orbitals are introduced in the band gap, and hence the electron excitation from these occupied states to the conduction band is able to lead to the visible-light absorption. In this model, the Bi dopant exists as Bi^{3+}.

(v) Although Bi@Ta and Bi@(Na, Ta) doped $NaTaO_3$ both tend to show visible light absorption, Bi@(Na, Ta) doped model can show enhanced photocatalytic hydrogen evolution under the visible light as compared to the undoped $NaTaO_3$ while Bi@Ta doped model can not. This is because Bi@Ta doping introduces unoccupied states below the H^+/H_2 level while Bi@(Na, Ta) doping introduce occupied states below the O_2/H_2O level.

Our electronic structure calculations unraveled the relationship between the three Bi-doped structures and the materials preparation conditions, and formulated the oxidation states of the Bi dopants in the $NaTaO_3$, and clarified the origin of the different photocatalytic hydrogen evolution behavior under the visible light.

5.5 Acknowledgment

Chapter 5, in full, is a reprint of the material ”Energetic Stability, Oxidation States, and Electronic Structure of Bi-doped $NaTaO_3$: First-Principles Hybrid Functional Study” as it appears in Physical Chemistry Chemical Physics. Paul H. Joo, Maziar Behtash, Kesong Yang, 18, 857-865, 2016. The dissertation author was the primary investigator and author of this paper.

Chapter 6

Nip the Sodium Dendrites in the Bud on Planar Doped Graphene:a first-principles study

Understanding the Na nucleation/growth mechanism in different electrolyte systems is the key to tackling the challenge of its severe dendritic growth at high-current densities. The structural complexities of existing substrates for Na plating can complicate the challenge and therefore, this chapter discusses three representative plating substrates; pristine (undoped), B-doped, and N-doped graphene. Based on the first-principles calculations, the dopants in doped graphene provide abundant preferential nucleation sites possessing strong affinity with Na atoms. Theses preferential nucleation sites are likely to be near the dopants, indicated by high binding energy. Also, the calculations reveal significant changes in the binding energies of Na nuclation on doped graphene compared to those of pristine graphene. As a result, the theoretical investigations allow the enhancement of the understanding of the stabilization of Na metal batteries.

6.1 Introduction

Sodium is known to be one of the most abundant element in the Earth's crust and since it possesses many similar physiochemical properties, it is discovered to be the most promising alternative for lithium batteries. Compared to Li, Na holds higher abundance and availability in terms of topography and cost. Such advantages have lead to a rapid research and development of high-energy Na batteries. Theoretically, it has already been discovered that specific energies of Na-ion batteries are three times higher than that of the conventional Li-ion batteries. As previously mentioned, Na metal suffers from the formation of dendritic nucleation/growth and low Coulombic efficiency over electrochemical plating at high current densities. Many attempts have been made to bring solutions to such limitations, which include the application of foreign material on Na metal surface [110, 163, 140] and encapsulation of the Na metal into an electrically conductive host with a porous channel structure.[79] However, less research effort has been placed on the fundamental underlying nucleation process of Na plating.

In this chapter, first-principles calculations have been conducted to examine the Na nucleation behaviors on the computational models of planar graphene substrates with different heteroatom dopants (B and N). The varying of binding affinity between Na atoms and the graphene substrates is observed with different types of heteroatom doping forms. Furthermore, the preferential "hot spots" for Na nucleation are determined by the binding energy calculations. Our theoretical study predicts the possibility of dendrite-free Na anode with doped planar graphene substrates.

6.2 Computational Details

First-principles density functional theory (DFT) calculations were carried out using the Vienna Ab initio Simulation Package (VASP).[63, 60] The Projector-Augmented Wave (PAW) potential was employed for the treatment of the electron-ion interactions [ref], and the Generalized

Gradient Approximation (GGA) parameterized by Perdew-Burke-Ernzerhof (PBE) was used for the electron exchange-correlation functional [97, 7]. The cut-off energy of 840 eV and $4 \times 4 \times 1$ k-point meshed centered at Γ-point were used. The relaxation of all atoms was performed until all components of the residual forces became less than 0.02 eV/Å and the convergence tolerance for the self-consistent-field iteration was set to 10^{-5} eV.

To investigate the structural stability of the N-doped graphene, we calculated their formation energies using the equation: $E_f = E_{N-doped} - (E_{undoped} - x\mu_C + y\mu_N$, where $E_{N-doped}$ and $E_{undoped}$ are the total energy of N-doped and undoped graphene, respectively; x is the number of C atoms removed from the undoped graphene and y is the number of doped N atoms.

To evaluate the strength of bonding strength between Na and N-doped graphene, we calculated the binding energy using the equation: $E_b = (E_{N-doped} + E_{Na}) - E_{Na-N-doped}$, where $E_{N-doped}$ and E_{Na} are the total energy of the N-doped graphene and an isolated Na atom, respectively; $E_{Na-N-doped}$ represents the total energy of the N-doped graphene after the Na-deposition.

6.3 Results and discussion

6.3.1 Binding Energy

In order to evaluate the interactions between Na atom and plating graphene substrate, we calculated the binding energies between the Na atoms and pristine (undoped), N-doped, and B-doped graphene. N and B atoms are selected as the dopants because they are the most widely studied dopants for graphene experimentally.[125, 77, 162] The calculated binding energies are shown in Figure 6.1a. As a comparison, the binding energies between Na atom and Cu surfaces were also calculated, because Cu foil is the regular plating substrate for metallic anode. Since the surface of Cu foil is polycrystalline with a combination of different facets, we modelled both Cu (111) and (001) surfaces. The deposition sites of Na atom on the graphene substrate are indicated

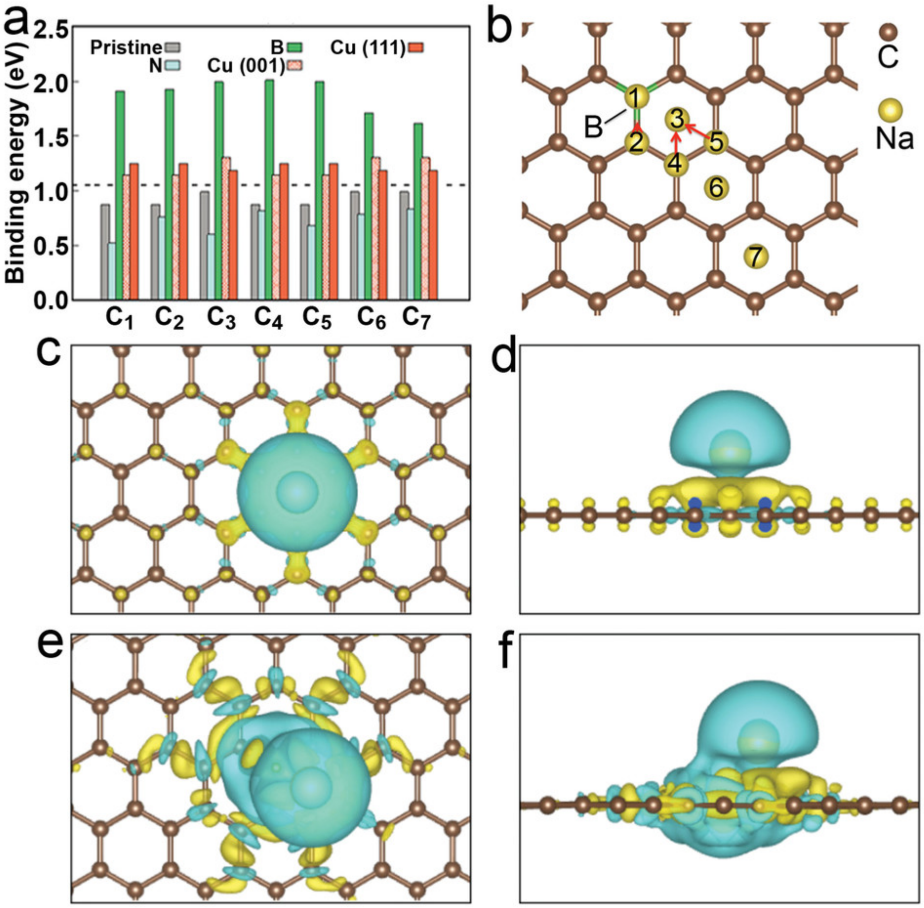

Figure 6.1: First-principles calculations of the interaction between Na atoms and different plating substrates. (a) Calculated binding energies of one Na atom with the pristine (undoped) graphene, B-doped graphene, and N-doped graphene, as well as with the Cu (001) and (111) surfaces. The C_n ($1 \leq n \leq 7$) represents the deposition sites of Na atoms on the substrates. (b) Structural models of Na deposition on the B-doped graphene. The yellow balls labelled from 1 to 7 are Na atoms, corresponding to the C_n ($1 \leq n \leq 7$). (c-f) Differential charge density plots of Na-deposited graphene. (c,d) Top view and side view of Na deposition on pristine graphene. (e,f) Top view and side view of Na deposition on B-doped graphene at site C_1. The cyan and yellow colors indicate the electron density decrease and increase, respectively.

by C_n ($1 \leq n \leq 7$), in which they are named according to the distance between the doping atoms and adsorption sites. C_1, $C_{2,4,5}$, and $C_{3,6,7}$ are located on top of the doping atoms, hexagonal rings, and C atoms, respectively, as shown with B-doped graphene, as an example in Figure 6.1b. For the B-doped graphene, the binding energy does not change significantly with the Na deposition in the same hexatomic ring (C_1-C_5, ranging between 1.9-2.0 eV). However, when the

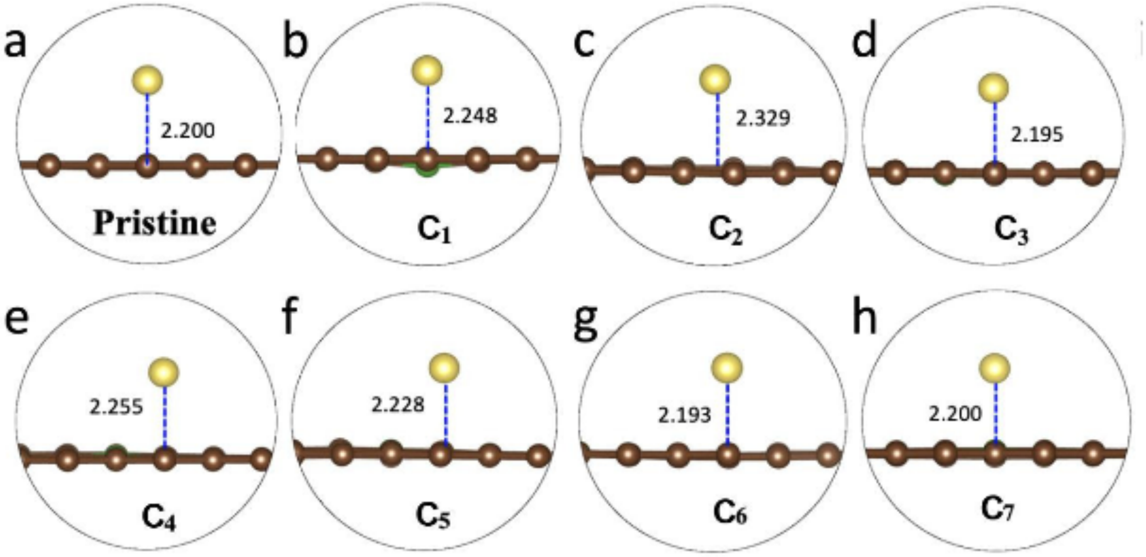

Figure 6.2: a) Partial geometry of pristine (undoped) graphene model with Na deposition and b-h) partial geometries of B-doped graphene with Na deposition. The distance (in *Å*) between the Na and the graphene plane is indicated in the blur dash line.

deposition sites are away from the B dopant (C_6-C_7), the binding energy decreases to 1.6-1.7 eV. Overall, the average binding energy between Na and the substrate decreases in the order of B-doped graphene (1.9 eV) $>$ bare Cu (1.21 eV for (001) and 1.19 eV for (111) $>$ pristine graphene (0.95 eV) $>$ graphitic N-doped graphene (0.70 eV). This indicates that Na atoms are energetically more favorable to be deposited on the B-doped graphene. The graphitic N model was selected for comparison, out of the three common types of N doping (graphitic N, pyridinic N, and pyrrolic N) because it has the lowest formation energy, as shown in Table 6.2. Figure 6.2 depicts the side view of Na depositions on the pristine and B-doped graphene substrate and it clearly shows that no significant distortion in the graphene plane is observed and that the distance between the Na atom and the plane varies at an insignificant range.

Next, we calculated the differential charge density for the Na-deposited graphene to display the charge transfer between the Na atoms and graphene substrate, as shown in Figure 6.1c-f. Figure 6.1c,d represent the top and side view of Na-deposited pristine (undoped) graphene, respectively. The yellow and cyan color indicate the electron density increase and decrease,

Table 6.1: Calculated number of transferred electrons of the Na onto B-doped graphene via Bader charge analysis. The model labels are consistent with the structures in Figure 6.1a. As a comparison, the calculated number of the Na on the pristine graphene (same position with C_1) is 0.882.

Na Atom	C_1	C_2	C_3	C_4	C_5	C_6	C_7
Bader charge	0.903	0.909	0.908	0.908	0.908	0.924	0.925

respectively. It is clear that the electrons are being transferred from the Na atom to the surrounding C atoms below the Na atom, implying that Na is chemically absorbed on the graphene surface. Figure 6.1e,f represent the top and side views of Na-deposition at site C_1 of the B-doped graphene, respectively. It clearly shows that the cyan region around the Na atom, particularly at the region connecting the Na and graphene, is relatively larger compared to the Na-deposited pristine graphene. This indicates more transfer of electrons from the Na to the B-doped graphene. In the same manner, larger yellow region is observed in the B-doped graphene than in the pristine graphene, meaning more gain of electrons in the B-doped graphene. To verify this conclusion, a quantitative analysis for the number of transferred electrons was carried out by using the Bader charge calculations. Table 6.2 shows the calculated number of transferred electrons of the Na atom onto B-doped graphene at each of the C_{1-7} sites, which the number of electrons range from 0.903-0.925. This is larger than the number of transferred electrons of the Na onto pristine graphene, which is calculated to be 0.882. Such phenomenon can be explained from the *p*-type doping effects caused by B dopants in the carbon-based materials. One substitution of C site with a B dopant can produce one hole in the graphene, which then can naturally attract electrons from the Na atom. Figure 6.1e clearly shows larger yellow regions on the nearest neighboring C atoms around the B dopant, as well as a large cyan region under the graphene plane in Figure 6.1f, compared to the pristine graphene. This indicates that the neighboring C atoms around the B dopant also gain electrons from Na, leading to more electron transfer from Na to the B-doped graphene and thus, larger adsorption energy compared to that in the pristine graphene.The hole states introduced by the B dopant extends to wider area on the graphene surface and thus, increasing the binding energy for different Na-deposition sites as well. In other word, the B-doped graphene substrate possesses abundant ”hot spots”, providing plentiful nucleation sites and lower the nucleation barrier for Na plating, therefore promoting uniform and dendrite-free Na plating. An opposite phenomenon occurs in the case of N-doped graphene, since N atom donates one electron into the graphene, suppressing the ability of graphene to obtain electrons from Na. This can be indicated by the decrease in the binding energy in Figure 6.1a.

Table 6.2: Calculated formation energy (E_f) and the binding energy (E_b) of Na on N-doped graphene. The model labels are consistent with the structures in Figure 6.3.

Model	System	E_f (eV)	E_b (eV)
A	Graphitic N	0.98	0.84
B	Pyridinic N (one N atom)	6.05	2.57
C	Pyridinic N (two N atom)	5.10	2.62
D	Pyridinic N (three N atom)	3.58	3.35
E	Pyridinic N (four N atom)	4.10	3.86
F	Pyrrolic N (one N atom)	6.04	2.56

For N-doped graphene, the N atoms can be embedded into the graphene lattice in two different forms, namely pyridinic and dominantly graphitic. The configurations of graphitic and pyridinic N are represented in Figure 6.3a and b-f, respectively. The calculated binding energy of the ideal graphitic N model is actually, already, shown in Figure 6.1a. Therefore, we further calculated the binding energy between the Na atom and different types of pyridinic N models, as shown in Table 6.2. Each model (A-F) corresponds to the configurations in Figure 6.3a-f, respectively. Because the pyridnic N can have different geometrical arrangements in N-doped graphene, the binding energy for each scenario is found to be different. Our formation energy calculations reveal that the pyridinic N model with three N atoms (model D) has the lowest formation energy, indicating that it is most likely to be formed experimentally. On the basis of model D, we selected three different Na-deposition sites; center of three N atoms (on top of hole), on top of one N, and on top of one hexagonal ring, as represented in Figure 6.4a,b, and c,

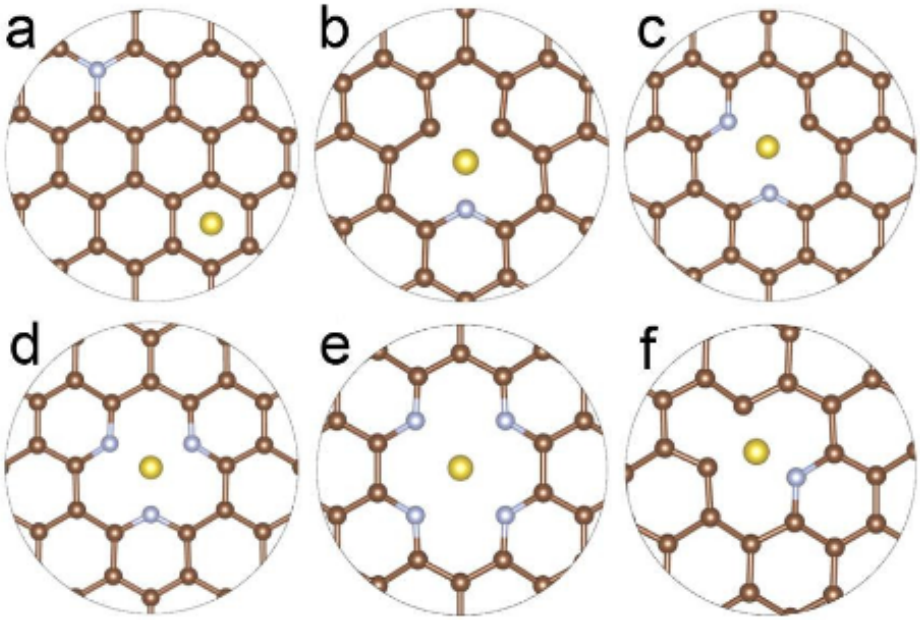

Figure 6.3: Relaxed geometrical structures of Na on N-doped graphene. a) graphitic N, b-e) pyridinic N with one, two, three, and four N atoms, respectively, and f) pyrrolic N. Note that the pyrrolic N model in f) becomes the pyridinic after structural relaxation.

respectively. However, the Na atom eventually migrated to the center after structural relaxation, as shown in Figure 6.4d-f, exhibiting the exact same structures as Figure 6.4a and thus, the same binding energy of 3.35 eV. Therefore, Na-deposition on pyridinic N-doped graphene is most likely to occur on top of the hole surrounded by the three N atoms.

6.4 Conclusions

Based on the theoretical investigations, we have studied the affinity of Na atoms to the B-doped, N-doped, and pristine graphene. The B-doped graphene reduces the Na nucleation barriers compared to the pristine graphene, indicated by the increase in the binding energy from 0.95 eV (pristine) to a range of 1.6-1.9 eV (B-doped). The range of binding energy among the different Na-deposition sites (C_1-C_7) on the B-doped graphene depends on the proximity of Na to the B dopant. As Na deposits further away from the B dopant, the binding energy is decreased meaning

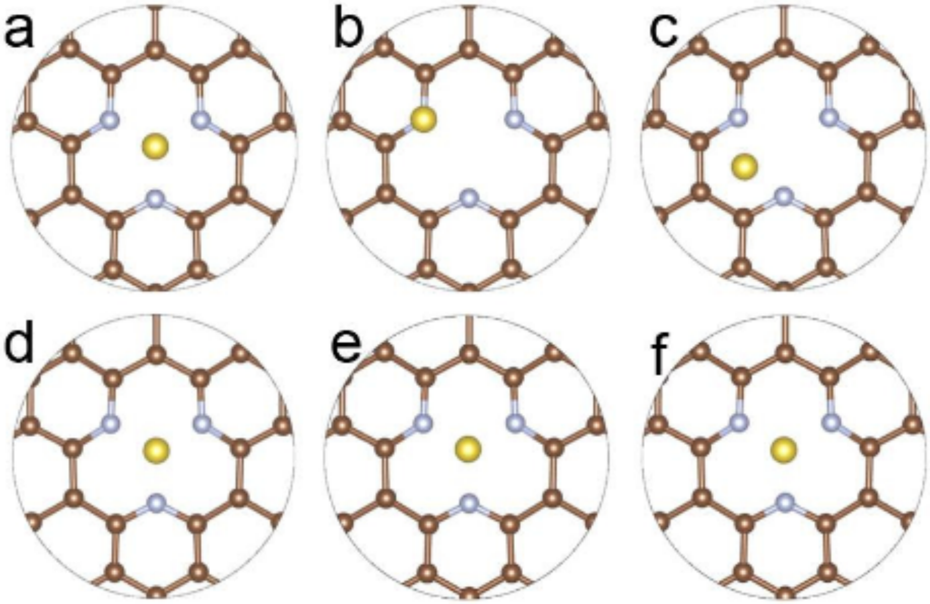

Figure 6.4: a-c) Unrelaxed and d-f) relaxed geometrical structures of Na on N-doped graphene based on the model of pyridinic N that has three N atoms and the lowest formation energy.

that the B dopant mainly contributes to the stronger affinity between the Na and the graphene substrate. The calculated differential charge densities show that more transfer of electrons occur between Na and B-doped graphene, compared to the pristine graphene. Quantitatively, the Bader charge analysis confirms the larger number of transferred electrons for the B-doped graphene. In terms of N-doped graphene, the formation energy calculations reveal that three N dopants are likely to be embedded pyridinically onto the graphene surface and Na is deposited on top of the hole surrounded by the dopants, verified by structural relaxation. The binding energy calculations show that the pyridinically N-doped graphene enhances Na nucleation, compared to that of graphitically N-doped graphene that actually suppresses the Na-deposition.

6.5 Acknowledgement

Chapter 6, in part, is a reprint of the material " Nip the Sodium Dendrites in the Bud on Planar Doped Graphene in Liquid/Gel Electrolytes". Xiaofei Hu, Paul Hyunggyu Joo, Huan Wang, Edward Matios, Chuanlong Wang, Jianmin Luo, Xuan Lu, Kesong Yang, and Weiyang Li. The dissertation author is the primary co-investigator and co-author of this paper.

Chapter 7

Conclusions

MoS_2 nano-catalysts are applied in the downstream sector of the petroleum industry, specifically, for the conversion of crude oil petroleum products into clean diesel fuel. To reduce the release of sulfur dioxide (SO_2) from the petroleum refinery and produce the ultra-low sulfur diesel, it is in critical need for detailed understanding of the properties of the MoS_2 nano-catalysts. In this thesis, we studied the single-layer MoS_2 nanosheets in two different shapes, triangular and hexagonal, using first-principles DFT calculations. Our research focused on the structural and catalytic properties of MoS_2, with the motivation to predict the improvements of the catalytic efficiency in the HDS process.

In the first project, our focus was centered on the structural properties of the triangular MoS_2 nanosheets, which are experimentally observed under S-rich conditions. By modeling the four commonly studied edge types, including ZZ-Mo1, ZZ-Mo2, ZZ-S1, and ZZ-S2, the formation energies were calculated with respect to size, n, to reveal the size effects on the MoS_2 nanosheets. It has been revealed that the formation energy decreases for all four edge-type MoS_2 with increase in the size of the nanosheets, indicating that larger MoS_2 nanosheets are energetically more favorable than the smaller nanosheets in terms of formation. Taking the most energetically favorable edge-type MoS_2, that is the ZZ-S2 type, we applied sulfur dimer vacancies at the extreme corner (V_S@Cnr) and center (V_S@Cen) site of one edge, in which sulfur vacancy is part of an initiating step in the HDS reaction. A strong odd-even effect in the formation of sulfur vacancies was discovered for both V_S@Cnr and V_S@Cen. Sulfur dimer vacancies tend to form at the center of the edge with an even number of Mo atoms on the edges of the MoS_2 nanosheets, while sulfur dimer vacancies tend to form at the corner with an odd number of Mo atoms on the edges. Theoretically, this can be described by the formation of Mo-S bonds between the vacancy site and the adjacent sulfur dimers in the relaxed structures.

As a potential alternative to the triangular MoS_2, we have introduced the structural and catalytic properties of monolayer Janus MoXY, which is commonly used in the HER process. The formation energy calculations revealed a similar decreasing trend for MoSSe and MoSTe, with respect to size. The hydrogen adsorption, which can determine the catalytic behavior, on corner of the Se-edge of the nanosheet (H@Cnr) also revealed an odd-even effect in the hydrogen Gibbs free energy (ΔG_H) regarding the size. The H@Cnr for the ZZ-S1 edge-type MoSSe resulted in a, relatively, lower ΔG_H for the nanosheets with an even number of Mo atoms on the edges, while H@Cnr for the ZZ-S2 edge-type MoSSe showed a complete opposite trend. The calculated ΔG_H for ZZ-S1 (n=5) and ZZ-S2 (n=4) was found to be 0.10 and -0.19 eV, respectively, indicating the best catalytic behavior.

To predict the trends within the TM promoters and the potential TM atoms for enhancing the HDS catalytic activity, 26 TM atoms were selected to study the promotion effects on the hexagonal MoS_2 nanosheets. Our calculations revealed that most TM promotions must occur under sulfur saturating conditions. Otherwise, most TM atoms would not attach on the nanosheet. The decreasing trend in the formation energy of sulfur vacancy (V_S@Cen) from group 3 to group 12 of the periodic table directly relates to the decreasing trend in the binding energy of each corresponding bulk TM-sulfide (E_b), as E_b can, in general, represent the bonding strength of TM-S. Therefore, weaker bonding strength leads to an easier formation of sulfur vacancy. Using E_b as descriptors, the Gibbs free energy for each of the three subindividual steps in the HDS reaction was calculated to evaluate the promotion effects. Higher E_b resulted in higher ΔG_1 and lower ΔG_3, while lower ΔG_2 resulted under optimal range of E_b that is neither too high nor too low. Combining the three steps, the TM-S bonding strength should not be extremely strong or extremely weak for an effective TM promotion. Based on the findings, the most promising TM promoters included Co, Cr, and Fe for the enhancement of catalytic performance of the MoS_2 nanocatalysts.

In the fourth project, we have studied a new material for an additional application of photocatalytic water splitting, which is the Bi-doped $NaTaO_3$. The energetic stability of the Bi-$NaTaO_3$ was found to be different with different doping sites under different growth conditions of the materials. Under Na-rich conditions, Bi is likely to be doped at Ta-site (Bi@Ta), while Bi is likely to be doped at Na-site (Bi@Na) under Na-poor conditions. Under mildly Na-rich conditions, two Bi are likely to be doped, simultaneously, at both Na- and Ta-site (Bi@(Na,Ta)). The Bi@Na showed an increase in the energetic bandgap with an *n*-type semiconductor characteristic, while Bi@Ta and Bi@(Na,Ta) showed intrinsic semiconducting characters with reduced bandgap within the visible-light range. However, only Bi@(Na,Ta) is found to be active for the photocatalytic water splitting, since its CBM and VBM lie above and below the photo-reduction and photo-oxidation level, respectively.

In the last project, we investigated the affinity of Na atoms to the B-doped, N-doped, and pristine graphene to understand the Na nucleation/growth mechanism for another application of Na metal batteries. Compared to the pristine graphene, the B-doped graphene tends to increase the Na affinity to the graphene, indicated by higher binding energy. The binding energies were found to be become lower as the Na atom deposits further away from the B dopant. The differential charge density and the Bader charge analysis showed larger electron transfers for the B-doped graphene, confirming its stronger affinity to the Na atom. Our calculations also showed weaker affinity of the Na atom to the N-doped graphene. However, the formation energy for different types of N-doping revealed that the N dopants are, actually, likely to be embedded pyridincally onto the graphene plane and the pyridinically N-doped graphene was found to enhance Na nucleation by depositing Na on top of the hole surrounded by the N dopants.

In summary, our first-principles DFT investigations on the structural and catalytic properties allow detailed understanding of the effects on the MoS_2 nanocatalysts for the HDS process. On the basis of such findings and predictions, we can increase the research motivations for the development of better high-performance HDS nanocatalysts.

Bibliography

[1] M. Ahtee and C. N. W. Darlington. Structures of $NaTaO_3$ by neutron powder diffraction. *Acta Crystallogr. Sect. B*, 36(5):1007–1014, 1980.

[2] M. Armand and J.-M. Tarascon. Building better batteries. *Nature*, 451:6521, 2008.

[3] M. Behtash, P. H. Joo, S. Nazir, and K. Yang. Electronic structures and formation energies of pentavalent-ion-doped SnO_2: First-principles hybrid functional calculations. *J. Appl. Phys.*, 117:175101, 2015.

[4] C. Bernal and K. Yang. First-principles hybrid functional study of the organicinorganic perovskites $CHNH_3SnBr_3$ and $CH_3NH_3SnI_3$. *J. Phys. Chem. C*, 118(42):24383–24388, 2014.

[5] F. Besenbacher, M. Brorson, B. Clausen, S. Helveg, B. Hinnemann, J. Kibsgaard, J. Lauritsen, P. Moses, J. Nørskov, and H. Topsøe. Recent STM, DFT and HAADF-STEM studies of sulfide-based hydrotreating catalysts: Insight into mechanistic, structural and particle size effects. *Catal. Today*, 130:86–96, 2008.

[6] B. Black. Oil creek as industrial apparatus: Re-creating the industrial process through the landscape of pennsylvania's oil boom. *Environmental History*, 3(2):210–229, 1998.

[7] P. E. Blöchl. Projector augmented-wave method. *Phys. Rev. B*, 50:17953–17979, 1994.

[8] M. V. Bollinger, J. V. Lauritsen, K. W. Jacobsen, J. K. Nørskov, S. Helveg, and F. Besenbacher. One-dimensional metallic edge states in MoS_2. *Phys. Rev. Lett.*, 87:196803, 2001.

[9] A. Bruix, H. G. Füchtbauer, A. K. Tuxen, A. S. Walton, M. Andersen, S. Porsgaard, F. Besenbacher, B. Hammer, and J. V. Lauritsen. *In Situ* detection of active edge sites in single-layer MoS_2 catalysts. *ACS Nano*, 9:9322–9330, 2015.

[10] E. Burstein. Anomalous optical absorption limit in InSb. *Phys. Rev.*, 93:632–633, 1954.

[11] L. S. Byskov, J. K. Nørskov, B. S. Clausen, and H. Topsøe. DFT calculations of unpromoted and promoted MoS_2-based hydrodesulfurization catalysts. *J. Catal.*, 187:109–122, 1999.

[12] D. Cao, T. Shen, P. Liang, X. Chen, and H. Shu. Role of Chemical Potential in Flake Shape and Edge Properties of Monolayer MoS_2. *J. Phys. Chem. C*, 119:4294–4301, 2015.

[13] I. E. Castelli, D. D. Landis, K. S. Thygesen, S. Dahl, I. Chorkendorff, T. F. Jaramillo, and K. W. Jacobsen. New cubic perovskites for one- and two-photon water splitting using the computational materials repository. *Energy Environ. Sci.*, 5:9034–9043, 2012.

[14] P. Chakraborty, G. Datta, and K. Ghatak. The simple analysis of the burstein-moss shift in degenerate n-type semiconductors. *Physica B: Condensed Matter*, 339(4):198 – 203, 2003.

[15] D. Chen, D. Yang, Q. Wang, and Z. Jiang. Effects of boron doping on photocatalytic activity and microstructure of titanium dioxide nanoparticles. *Ind. Eng. Chem. Res.*, 45(12):4110–4116, 2006.

[16] X. Chen, S. Shen, L. Guo, and S. S. Mao. Semiconductor-based photocatalytic hydrogen generation. *Chem. Rev.*, 110(11):6503–6570, 2010.

[17] R. R. Chianelli, M. H. Siadati, M. P. De la Rosa, G. Berhault, J. P. Wilcoxon, R. Bearden Jr., and B. L. Abrams. Catalytic properties of single layers of transition metal sulfide catalytic materials. *Cat. Rev.-Sci. Eng.*, 48:1–41, 2006.

[18] R. D. Chirico, S. E. Knipmeyer, A. Nguyen, and W. V. Steele. The thermodynamic properties of biphenyl. *J. Chem. Thermodynamics*, 21:1307–1331, 1989.

[19] R. D. Chirico, S. E. Knipmeyer, A. Nguyen, and W. V. Steele. The thermodynamic properties of dibenzothiophene. *J. Chem. Thermodynamics*, 23:431–450, 1991.

[20] X. Dai, K. Du, Z. Li, M. Liu, Y. Ma, H. Sun, X. Zhang, and Y. Yang. Co-doped MoS_2 nanosheets with the dominant CoMoS phase coated on carbon as an excellent electrocatalyst for hydrogen evolution. *ACS Appl. Mater. Interfaces*, 7(49):27242–27253, 2015.

[21] F. L. Deepak, A. Mayoral, and M. J. Yacaman. Faceted MoS_2 nanotubes and nanoflowers. *Mater. Chem. Phys*, 118:392–397, 2009.

[22] S. Ding, S. Jiang, Y. Zhou, Q. Wei, and W. Zhou. Catalytic characteristics of active corner sites in Co-Mo-S nanostructure hydrodesulfurization – a mechanism study based on DFT calculations. *J. Catal.*, 345:24–38, 2017.

[23] M. R. DuBois. Catalytic applications of transition-metal complexes with sulfide ligands. *Chem. Rev.*, 89:1–9, 1989.

[24] D. Escalera-López, Y. Niu, J. Yin, K. Cooke, N. V. Rees, and R. E. Palmer. Enhancement of the hydrogen evolution reaction from Ni-MoS_2 hybrid nanoclusters. *ACS Catal.*, 6:6008–6017, 2016.

[25] H. Farag. A Comparative Assessment of the Effect of H_2S on Hydrodesulfurization of Dibenzothiophene Over Nanosize MoS_2- and CoMo-Based Al_2O_3 Catalysts. *Appl. Catal. A: Gen.*, 331:51–59, 2007.

[26] H. Fu, S. Zhang, L. Zhang, and Y. Zhu. Visible-light-driven $NaTaO_{3-x}N_x$ catalyst prepared by a hydrothermal process. *Mater. Res. Bull.*, 43:864 – 872, 2008.

[27] Y. Fujimoto. Local structure of the infrared bismuth luminescent center in bismuth-doped silica glass. *J. Am. Ceram. Soc.*, 93(2):581–589, 2010.

[28] J. H. Gary, G. E. Handwerk, and M. J. Kaiser. *Petroleum Refining: Technology and Economics*. CRC Press: Taylor & Francis Group, 5 edition, 2013.

[29] C. Geantet, J. De Los Reyes, M. Cattenot, M. Vrinat, M. Breysse, and S. Gőbölös. Ruthenium molybdenum sulphide catalysts: physicochemical characterization and catalytic properties in hds, hydrogenation and hdn reactions. *Catal. Today*, 10(4):665–680, 1991.

[30] M. R. Gholipour, D. Cao-Thang, B. François, and D. Trong-On. Nanocomposite heterojunctions as sunlight-driven photocatalysts for hydrogen production from water splitting. *Nanoscale*, 7:8187–8208, 2015.

[31] S. Grimme, J. Antony, S. Ehrlich, and H. Krieg. A consistent and accurate ab initio parametrization of density functional dispersion correction (dft-d) for the 94 elements H-Pu. *J. Chem. Phys.*, 132(15):154104, 2010.

[32] S. S. Grønborg, N. Salazar, A. Bruix, J. Rodríguez-Fernández, S. D. Thomsen, B. Hammer, and J. V. Lauritsen. Visualizing hydrogen-induced reshaping and edge activation in MoS_2 and Co-promoted MoS_2 catalyst clusters. *Nat. Commun.*, 9:2211, 2018.

[33] Y. Guo, J. Tang, H. Qian, Z. Wang, and Y. Yamauchi. One-pot synthesis of zeolitic imidazolate framework 67-derived hollow $Co_3S_4@MoS_2$ heterostructures as efficient bifunctional catalysts. *Chem. Mater.*, 29(13):5566–5573, 2017.

[34] R. He, S. Cao, P. Zhou, and J. Yu. Recent advances in visible light Bi-based photocatalysts. *Chin. J. Catal.*, 35:989 – 1007, 2014.

[35] T. He, L. Xu, Y. Zhang, H. Huang, and H. Jiao. High-quality vanadium-doped MoS_2 ultrathin nanosheets as an efficient orr catalyst. 43:1611–1616, 2019.

[36] Y. He, Y. Zhu, and N. Wu. Synthesis of nanosized $NaTaO_3$ in low temperature and its photocatalytic performance. *J. Solid State Chem.*, 177(11):3868 – 3872, 2004.

[37] S. Helveg, J. V. Lauritsen, E. Lægsgaard, I. Stensgaard, J. K. Nørskov, B. S. Clausen, H. Topsøe, and F. Besenbacher. Atomic-scale structure of single-layer MoS_2 nanoclusters. *Phys. Rev. Lett.*, 84:951–954, 2000.

[38] B. Hinnemann, P. G. Moses, and J. K. Nørskov. Recent density functional studies of hydrodesulfurization catalysts: insight into structure and mechanism. *J. Phys.: Conden. Matt.*, 20:064236, 2008.

[39] M. R. Hoffmann, S. T. Martin, W. Choi, and D. W. Bahnemann. Environmental applications of semiconductor photocatalysis. *Chem. Rev.*, 95(1):69–96, 1995.

[40] C.-C. Hu and H. Teng. Influence of structural features on the photocatalytic activity of $NaTaO_3$ powders from different synthesis methods. *Appl. Catal. A: Gen.*, 331:44–50, 2007.

[41] C. Huanan, S. Jianying, and L. Hong. Influence of Bi chemical state on the photocatalytic performance of Bi-doped $NaTaO_3$. *Chin. J. Catal.*, 36(7):969 – 974, 2015.

[42] A. Iwase, H. Kato, and A. Kudo. The effect of alkaline earth metal ion dopants on photocatalytic water splitting by $NaTaO_3$ powder. *ChemSusChem*, 2:873–877, 2009.

[43] S. Jafarinejad. Control and treatment of sulfur compounds specially sulfur oxides (SO_x) emissions from the petroleum industry: A review. *Chem. Int.*, 2:242–253, 10 2016.

[44] A. Janotti, J. B. Varley, P. Rinke, N. Umezawa, G. Kresse, and C. G. Van de Walle. Hybrid functional studies of the oxygen vacancy in TiO_2. *Phys. Rev. B*, 81:085212, 2010.

[45] T. F. Jaramillo, K. P. Jørgensen, J. Bonde, J. H. Nielsen, S. Horch, and I. Chorkendorff. Identification of Active Edge Sites for Electrochemical H_2 Evolution from MoS_2 Nanocatalysts. *Science*, 317:100–102, 2007.

[46] C. Jiang, S. J. A. Moniz, A. Wang, T. Zhang, and J. Tang. Photoelectrochemical devices for solar water splitting materials and challenges. *Chem. Soc. Rev.*, 46:4645–4660, 2017.

[47] H.-Y. Jiang, J. Liu, K. Cheng, W. Sun, and J. Lin. Enhanced visible light photocatalysis of Bi_2O_3 upon fluorination. *J. Phys. Chem. C*, 117(39):20029–20036, 2013.

[48] R. O. Jones and O. Gunnarsson. The density functional formalism, its applications and prospects. *Rev. Mod. Phys.*, 61:689–746, 1989.

[49] P. H. Joo, J. Cheng, and K. Yang. Size effects and odd-even effects in MoS_2 nanosheets: First-principles studies. *Phys. Chem. Chem. Phys.*, 19:29927–29933, 2017.

[50] K. Y. Jung, S. B. Park, and S.-K. Ihm. Local structure and photocatalytic activity of B_2O_3-SiO_2/TiO_2 ternary mixed oxides prepared by sol-gel method. *Appl. Catal. B: Environ.*, 51(4):239 – 245, 2004.

[51] T. Kako, Z. Zou, M. Katagiri, and J. Ye. Decomposition of organic compounds over $NaBiO_3$ under visible light irradiation. *Chem. Mater.*, 19(2):198–202, 2007.

[52] H. W. Kang, S. N. Lim, and S. B. Park. Photocatalytic H_2 evolution under visible light from aqueous methanol solution on $NaBi_xTa_{1-x}O_3$ prepared by spray pyrolysis. *Int. J. Hydrogen Energy*, 37:4026 – 4035, 2012.

[53] P. Kanhere, J. Nisar, Y. Tang, B. Pathak, R. Ahuja, J. Zheng, and Z. Chen. Electronic structure, optical properties, and photocatalytic activities of $LaFeO_3$-$NaTaO_3$ solid solution. *J. Phys. Chem. C*, 116(43):22767–22773, 2012.

[54] P. Kanhere, Y. Tang, J. Zheng, and Z. Chen. Synthesis, photophysical properties, and photocatalytic applications of Bi doped $NaTaO_3$ and Bi doped $Na_2Ta_2O_6$ nanoparticles. *J. Phys. Chem. Solids*, 74(12):1708 – 1713, 2013.

[55] P. Kanhere, J. Zheng, and Z. Chen. Site specific optical and photocatalytic properties of Bi-doped $NaTaO_3$. *J. Phys. Chem. C*, 115(23):11846–11853, 2011.

[56] P. Kanhere, J. Zheng, and Z. Chen. Visible light driven photocatalytic hydrogen evolution and photophysical properties of Bi^{3+} doped $NaTaO_3$. *Int. J. Hydrogen Energy*, 37:4889 – 4896, 2012.

[57] H. Kato, K. Asakura, and A. Kudo. Highly efficient water splitting into H_2 and O_2 over lanthanum-doped $NaTaO_3$ photocatalysts with high crystallinity and surface nanostructure. *J. Am. Chem. Soc.*, 125(10):3082–3089, 2003.

[58] H. Kato and A. Kudo. Water splitting into H_2 and O_2 on alkali tantalate photocatalysts $ATaO_3$ (A = Li, Na, and K). *J. Phys. Chem. B*, 105(19):4285–4292, 2001.

[59] V. Kaushik, S. Wu, H. Jang, J. Kang, K. Kim, and J. W. Suk. Scalable exfoliation of bulk MoS_2 to single- and few-layers using toroidal taylor vortices. *Nat. Mater.*, 8(8), 2018.

[60] G. Kresse and J. Furthmüller. Efficiency of ab-initio total energy calculations for metals and semiconductors using a plane-wave basis set. *Comp. Mat. Sci.*, 6:15–50, 1996.

[61] G. Kresse and J. Furthmüller. Efficiency of ab-initio total energy calculations for metals and semiconductors using a plane-wave basis set. *Comp. Mat. Sci.*, 6(1):15 – 50, 1996.

[62] G. Kresse and J. Furthmüller. Efficient iterative schemes for *ab initio* total-energy calculations using a plane-wave basis set. *Phys. Rev. B*, 54:11169–11186, 1996.

[63] G. Kresse and D. Joubert. From ultrasoft pseudopotentials to the projector augmented-wave method. *Phys. Rev. B*, 59:1758–1775, 1999.

[64] P. S. Kulkarni and C. A. M. Afonso. Deep desulfurization of diesel fuel using ionic liquids: current status and future challenges. *Green Chem.*, 12:1139–1149, 2010.

[65] D. Laughton. The management of flexibility in the upstream petroleum industry. *Energy J.*, 19(1):83–114, 1998.

[66] J. Lauritsen and F. Besenbacher. Atom-resolved scanning tunneling microscopy investigations of molecular adsorption on MoS_2 and CoMoS hydrodesulfurization catalysts. *J. Catal.*, 328:49–58, 2015.

[67] J. V. Lauritsen, S. Helveg, E. Lægsgaard, I. Stensgaard, B. S. Clausen, H. Topsøe, and F. Besenbacher. Atomic-scale structure of Co-Mo-S nanoclusters in hydrotreating catalysts. *J. Catal.*, 197:1–5, 2001.

[68] J. V. Lauritsen, J. Kibsgaard, S. Helveg, H. Topsøe, B. S. Clausen, E. Lægsgaard, and F. Besenbacher. Size-dependent structure of MoS_2 nanocrystals. *Nat. Nanotechnol.*, 2:53–58, 2007.

[69] J. V. Lauritsen, J. Kibsgaard, G. H. Olesen, P. G. Moses, B. Hinnemann, S. Helveg, J. K. Nørskov, B. S. Clausen, H. Topsøe, E. Lægsgaard, and F. Besenbacher. Location and coordination of promoter atoms in Co- and Ni-promoted MoS_2-based hydrotreating catalysts. *J. Catal.*, 249:220–233, 2007.

[70] J. H. Lee, W. S. Jang, S. W. Han, and H. K. Baik. Efficient hydrogen evolution by mechanically strained MoS_2 nanosheets. *Langmuir*, 30(32):9866–9873, 2014.

[71] R. G. Leliveld and S. E. Eijsbouts. How a 70-year-old catalytic refinery process is still ever dependent on innovation. *Catal. Today*, 130:183–189, 2008.

[72] R. Li, F. Zhang, D. Wang, J. Yang, M. Li, J. Zhu, X. Zhou, H. Han, and C. Li. Spatial separation of photogenerated electrons and holes among $\{010\}$ and $\{110\}$ crystal facets of $BiVO_4$. *Nat. Commun.*, 4:1432, 2013.

[73] Z. Li, Y. Wang, J. Liu, G. Chen, Y. Li, and C. Zhou. Photocatalytic hydrogen production from aqueous methanol solutions under visible light over $Na(Bi_xTa_{1-x})O_3$ solid-solution. *Int. J. Hydrogen Energy*, 34(1):147 – 152, 2009.

[74] W.-H. Lin, C. Cheng, C.-C. Hu, and H. Teng. $NaTaO_3$ photocatalysts of different crystalline structures for water splitting into H_2 and O_2. *Appl. Phys. Lett.*, 89:211904, 2006.

[75] D.-R. Liu, C.-D. Wei, B. Xue, X.-G. Zhang, and Y.-S. Jiang. Synthesis and photocatalytic activity of N-doped $NaTaO_3$ compounds calcined at low temperature. *J. Hazard. Mater.*, 182(13):50 – 54, 2010.

[76] J. Liu, G. Chen, Z. Li, and Z. Zhang. Hydrothermal synthesis and photocatalytic properties of $ATaO_3$ and $ANbO_3$ (A= Na and K. *Int. J. Hydrogen Energy*, 32:2269 – 2272, 2007.

[77] L. Liu, Y.-X. Yin, J.-Y. Li, S.-H. Wang, Y.-G. Guo, and L.-J. Wan. Uniform lithium nucleation/growth induced by lightweight nitrogen-doped graphitic carbon foams for high-performance lithium metal anodes. *Adv. Mater.*, 30:1706216, 2018.

[78] A.-Y. Lu, H. Zhu, J. Xiao, C.-P. Chuu, Y. Han, M.-H. Chiu, C.-C. Cheng, C.-W. Yang, K.-H. Wei, Y. Yang, Y. Wang, D. Sokaras, D. Nordlund, P. Yang, D. A. Muller, M.-Y. Chou, X. Zhang, and L.-J. Li. Janus monolayers of transition metal dichalcogenides. *Nat. Nanotechnol.*, 12:744–749, 2017.

[79] W. Luo, Y. Zhang, S. Xu, J. Dai, E. Hitz, Y. Li, C. Yang, C. Chen, B. Liu, and L. Hu. Encapsulation of metallic Na in an electrically conductive host with porous channels as a highly stable Na metal anode. *Nano Lett.*, 17(6):3792–3797, 2017.

[80] Y. Ma, Q. Guo, M. Yang, Y. Wang, T. Chen, Q. Chen, X. Zhu, Q. Xia, S. Li, and H. Xia. Highly doped graphene with multi-dopants for high-capacity and ultrastable sodium-ion batteries. *Energy Storage Mater.*, 13:134 – 141, 2018.

[81] S. Marzooghi, B. E. Finch, W. A. Stubblefield, and D. M. Di Toro. Predicting phototoxicity of alkylated PAHs, mixtures of PAHs, and water accommodated fractions (WAF) of neat and weathered petroleum with the phototoxic target lipid model. *Environ. Toxicol. Chem.*, 37(8):2165–2174, 2018.

[82] A. J. Medford, A. Vojvodic, J. S. Hummelshøj, J. Voss, F. Abild-Pedersen, F. Studt, T. Bligaard, A. Nilsson, and J. K. Nørskov. From the sabatier principle to a predictive theory of transition-metal heterogeneous catalysis. *J. Catal.*, 328:36–42, 2015.

[83] W. H. Miller, W. L. Hase, and C. L. Darling. A simple model for correcting the zero point energy problem in classical trajectory simulations of polyatomic molecules. *J. Chem. Phys.*, 91(5):2863–2868, 1989.

[84] B. Modak, K. Srinivasu, and S. K. Ghosh. Band gap engineering of $NaTaO_3$ using density functional theory: a charge compensated codoping strategy. *Phys. Chem. Chem. Phys.*, 16:17116–17124, 2014.

[85] F. Niefind, W. Bensch, M. Deng, L. Kienle, J. Cruz-Reyes, and J. M. D. V. Granados. Co-promoted MoS_2 for hydrodesulfurization: New preparation method of MoS_2 at room temperature and observation of massive differences of the selectivity depending on the activation atmosphere. *Appl. Catal. A: Gen.*, 497:72–84, 2015.

[86] J. K. Nørskov, T. Bligaard, A. Logadottir, J. R. Kitchin, J. G. Chen, S. Pandelov, and U. Stimming. Trends in the exchange current for hydrogen evolution. *J. Electrochem. Soc.*, 152:J23 – J26, 2005.

[87] J. K. Nørskov, B. S. Clausen, and H. Topsøe. Understanding the trends in the hydrodesulfurization activity of the transition metal sulfides. *Catal. Lett.*, 13(1):1 – 8, 1992.

[88] K. S. Novoselov and A. H. Neto Castro. Two-dimensional crystals-based heterostructures: Materials with tailored properties. 2012:014006, 2012.

[89] L. Nurdiwijayanto, R. Ma, N. Sakai, and T. Sasaki. Stability and nature of chemically exfoliated MoS_2 in aqueous suspensions. *Inorg. Chem.*, 56(14):7620–7623, 2017.

[90] P. A. G. Ohare, B. M. Lewis, and B. A. Parkinson. Standard molar enthalpy of formation by fluorine-combustion calorimetry of tungsten diselenide (WSe_2). Thermodynamics of the high-temperature vaporization of WSe_2. Revised value of the standard molar enthalpy of formation of molybdenite (MoS_2). *J. Chem. Thermodynamics*, 20:681–691, 1988.

[91] H. Orita, K. Uchida, and N. Itoh. A volcano-type relationship between the adsorption energy of thiophene on promoted MoS_2 cluster-model catalysts and the experimental hds activity: Ab initio density functional study. *Appl. Catal. A: Gen.*, 258:115–120, 2004.

[92] F. E. Osterloh. Inorganic materials as catalysts for photochemical splitting of water. *Chem. Mater.*, 20(1):35–54, 2008.

[93] J.-F. Paul and E. Payen. Vacancy Formation on MoS_2 Hydrodesulfurization Catalyst: DFT Study of the Mechanism. *J. Phys. Chem. B*, 107:4057–4064, 2003.

[94] E. Payen, S. Kasztelan, S. Houssenbay, R. Szymanski, and J. Grimblot. Genesis and characterization by laser raman spectroscopy and high-resolution electron microscopy of supported MoS_2 crystallites. *J. Phys. Chem.*, 93:6501–6506, 1989.

[95] T. A. Pecoraro and R. R. Chianelli. Hydrodesulfurization catalysis by transition metal sulfides. *J. Catal.*, 67:430–445, 1981.

[96] J. P. Perdew, K. Burke, and M. Ernzerhof. Generalized Gradient Approximation Made Simple. *Phys. Rev. Lett.*, 77:3865–3868, 1996.

[97] J. P. Perdew, K. Burke, and M. Ernzerhof. Generalized gradient approximation made simple. *Phys. Rev. Lett.*, 77:3865–3868, 1996.

[98] S. P. Phivilay, A. A. Puretzky, K. Domen, and I. E. Wachs. Nature of catalytic active sites present on the surface of advanced bulk tantalum mixed oxide photocatalysts. *ACS Catal.*, 3:2920–2929, 2013.

[99] H. Qi, D. Li, C. Yang, Y. Ma, W. Li, Y. Sun, and B. Zhong. Nickel and manganese co-modified K/MoS_2 catalyst: high performance for higher alcohols synthesis from CO hydrogenation. 4(7):339–342, 2003.

[100] B. Radisavljevic, A. Radenovic, J. Brivio, V. Giacometti, and A. Kis. Single-layer MoS_2 transistors. *Nat. Nanotechnol.*, 6:147.

[101] S. Rangarajan and M. Mavrikakis. On the preferred active sites of promoted MoS_2 for hydrodesulfurization with minimal organonitrogen inhibition. *ACS Catal.*, 7:501–509, 2017.

[102] B. G. Rao, H. S. S. R. Matte, P. Chaturbedy, and C. N. R. Rao. Hydrodesulfurization of thiophene over few-layer MoS_2 covered with cobalt and nickel nanoparticles. *ChemPlusChem*, 78:419–422, 2013.

[103] K. H. Reddy, S. Martha, and K. M. Parida. Facile fabrication of Bi_2O_3/Bi-$NaTaO_3$ photocatalysts for hydrogen generation under visible light irradiation. *RSC Adv.*, 2:9423–9436, 2012.

[104] P. Sabatier. *Catalysis in Organic Chemistry*. D. Van Nostrand Company, 1913.

[105] S. K. Sahu, S. Zlotnik, A. Navrotsky, and P. M. Vilarinho. Thermodynamic stability of lead-free alkali niobate and tantalate perovskites. *J. Mater. Chem. C*, 3:7691–7698, 2015.

[106] L. Samad, S. M. Bladow, Q. Ding, J. Zhuo, R. M. Jacobberger, M. S. Arnold, and S. Jin. Layer-controlled chemical vapor deposition growth of MoS_2 vertical heterostructures via van der waals epitaxy. *ACS Nano*, 10:7039–7046, 2016.

[107] M. Šarić, J. Rossmeisl, and P. G. Moses. Modeling the active sites of Co-promoted MoS_2 particles by DFT. *Phys. Chem. Chem. Phys.*, 19:2017–2024, 2017.

[108] H. Schweiger, P. Raybaud, G. Kresse, and H. Toulhoat. Shape and edge sites modifications of MoS_2 catalytic nanoparticles induced by working conditions: A theoretical study. *J. Catal.*, 207:76 – 87, 2002.

[109] A. P. Scott and L. Radom. Harmonic vibrational frequencies: an evaluation of hartreefock, møllerplesset, quadratic configuration interaction, density functional theory, and semiempirical scale factors. *J. Phys. Chem.*, 100(41):16502–16513, 1996.

[110] Z. W. Seh, J. Sun, Y. Sun, and Y. Cui. A highly reversible room-temperature sodium metal anode. *ACS Cent. Sci.*, 1(8):449–455, 2015.

[111] D.-H. Seo, A. Urban, and G. Ceder. Calibrating transition-metal energy levels and oxygen bands in first-principles calculations: Accurate prediction of redox potentials and charge transfer in lithium transition-metal oxides. *Phys. Rev. B*, 92:115118, 2015.

[112] S. Sharifvaghefi and Y. Zheng. Development of a magnetically recyclable molybdenum disulfide catalyst for direct hydrodesulfurization. *ChemCatChem*, 7:3397–3403, 2015.

[113] T. A. Shastry, I. Balla, H. Bergeron, S. H. Amsterdam, T. J. Marks, and M. C. Hersam. Mutual photoluminescence quenching and photovoltaic effect in large-area single-layer MoS_2polymer heterojunctions. *ACS Nano*, 10(11):10573–10579, 2016.

[114] W. Shi, K. Fan, and Z. Wang. Catalytic activity for the hydrogen evolution reaction of edges in janus monolayer MoXY (X/Y = S, Se, and Te). *Phys. Chem. Chem. Phys.*, 20:29423–29429, 2018.

[115] W. Shi and Z. Wang. Effect of oxygen doping on the hydrogen evolution reaction in MoS_2 monolayer. *J. Taiwan. Inst. Chem. Eng.*, 82:163–168, 2018.

[116] Y. Shi, J.-K. Huang, L. Jin, Y.-T. Hsu, S. F. Yu, L.-J. Li, and H. Y. Yang. Selective decoration of Au nanoparticles on monolayer MoS_2 single crystals. *Sci. Rep.*, 3:1839, 2013.

[117] Y. Shi, Y. Zhou, D.-R. Yang, W.-X. Xu, C. Wang, F.-B. Wang, J.-J. Xu, X.-H. Xia, and H.-Y. Chen. Energy level engineering of MoS_2 by transition-metal doping for accelerating hydrogen evolution reaction. *J. Am. Chem. Soc.*, 139(43):15479–15485, 2017.

[118] V. Shokhen and D. Zitoun. Platinum-group metal grown on vertically aligned MoS_2 as electrocatalysts for hydrogen evolution reaction. 257:49–55, 2017.

[119] H. Shu, F. Li, C. Hu, P. Liang, D. Cao, and X. Chen. The capacity fading mechanism and improvement of cycling stability in MoS_2-based anode materials for lithium-ion batteries. *Nanoscale*, 8:2918–2926, 2016.

[120] D. Singh, S. K. Gupta, Y. Sonvane, A. Kumar, and R. Ahuja. 2d-HfS_2 as an efficient photocatalyst for water splitting. *Catal. Sci. Technol.*, 6:6605–6614, 2016.

[121] J. Sollner, D. F. Gonzalez, J. H. Leal, T. M. Eubanks, and J. G. Parsons. Hds of dibenzothiophene with $CoMoS_2$ synthesized using elemental sulfur. *Inorganica Chim. Acta*, 466:212–218, 2017.

[122] C. Song. An overview of new approaches to deep desulfurization for ultra-clean gasoline, diesel fuel and jet fuel. *Catal. Today*, 86:211–263, 2003.

[123] C. Song and X. Ma. New design approaches to ultra-clean diesel fuels by deep desulfurization and deep dearomatization. *Appl. Catal. B: Environ.*, 41:207–238, 2003.

[124] A. Stanislaus, A. Marafi, and M. S. Rana. Recent advances in the science and technology of ultra low sulfur diesel (ULSD) production. *Catal. Today*, 153:1–68, 2010.

[125] B. Sun, P. Li, J. Zhang, D. Wang, P. Munroe, C. Wang, P. H. L. Notten, and G. Wang. Dendrite-free sodium-metal anodes for high-energy sodium-metal batteries. *Adv. Mater.*, 30:1801334, 2018.

[126] J. Suntivich, K. J. May, H. A. Gasteiger, J. B. Goodenough, and Y. Shao-Horn. A perovskite oxide optimized for oxygen evolution catalysis from molecular orbital principles. *Science*, 334(6061):1383–1385, 2011.

[127] H. Topsøe, B. S. Clausen, R. Candia, C. Wivel, and S. Mørup. *In Situ* M*ö*ssbauer emission spectroscopy studies of unsupported and supported sulfided Co-Mo hydrodesulfurization catalysts: Evidence for and nature of a Co-Mo-S phase. *J. Catal.*, 68:433–452, 1981.

[128] C. Tsai, F. Abild-Pedersen, and J. K. Nørskov. Tuning the MoS_2 Edge-Site Activity for Hydrogen Evolution via Support Interactions. *Nano Lett.*, 14:1381–1387, 2014.

[129] A. Tuxen, J. Kibsgaard, H. Gøbel, E. Lægsgaard, H. Topsøe, J. V. Lauritsen, and F. Besenbacher. Size Threshold in the Dibenzothiophene Adsorption on MoS_2 Nanoclusters. *ACS Nano*, 4:4677–4682, 2010.

[130] A. K. Tuxen, H. G. Füchtbauer, B. Temel, B. Hinnemann, H. Topsøe, K. G. Knudsen, F. Besenbacher, and J. V. Lauritsen. Atomic-scale insight into adsorption of sterically hindered dibenzothiophenes on MoS_2 and Co-Mo-S hydrotreating catalysts. *J. Catal.*, 295:146–154, 2012.

[131] A. Vojvodic and J. K. Nørskov. Optimizing perovskites for the water-splitting reaction. *Science*, 334:1355–1356, 2011.

[132] M. Voldsund, K. Jordal, and R. Anantharaman. Hydrogen production with CO_2 capture. *Int. J. Hydrogen Energy*, 41(9):4969 – 4992, 2016.

[133] D. D. Wagman, W. H. Evans, V. B. Parker, R. H. Schumm, I. Halow, S. M. Bailey, K. L. Churney, and R. L. Nuttall. Erratum: The nbs tables of chemical thermodynamic properties. selected values for inorganic and c_1 and c_2 organic substances in si units [j. phys. chem. ref. data 11, suppl. 2 (1982)]. *J. Phys. Chem. Ref. Data*, 18(4):1807 – 1812, 1989.

[134] N. Wakabayashi, H. G. Smith, and R. M. Nicklow. Lattice dynamics of hexagonal MoS_2 studied by neutron scattering*. *Phys. Rev. B*, 12:659–663, 1975.

[135] A. Walsh, Y. Yan, M. N. Huda, M. M. Al-Jassim, and S.-H. Wei. Band edge electronic structure of $BiVO_4$: Elucidating the role of the Bi s and V d orbitals. *Chem. Mater.*, 21:547–551, 2009.

[136] M. G. Walter, E. L. Warren, J. R. McKone, S. W. Boettcher, Q. Mi, E. A. Santori, and N. S. Lewis. Solar water splitting cells. *Chem. Rev.*, 110:6446–6473, 2010.

[137] A. S. Walton, J. V. Lauritsen, H. Topsøe, and F. Besenbacher. MoS_2 nanoparticle morphologies in hydrodesulfurization catalysis studied by scanning tunneling microscopy. *J. Catal.*, 308:306–318, 2013.

[138] B. Wang, P. D. Kanhere, Z. Chen, J. Nisar, B. Pathak, and R. Ahuja. Anion-doped $NaTaO_3$ for visible light photocatalysis. *J. Phys. Chem. C*, 117(44):22518–22524, 2013.

[139] H. Wang, C. Tsai, D. Kong, K. Chan, F. Abild-Pedersen, J. K. Nørskov, and Y. Cui. Transition-metal doped edge sites in vertically aligned MoS_2 catalysts for enhanced hydrogen evolution. *Nano Res.*, 8:566–575, 2015.

[140] H. Wang, C. Wang, E. Matios, and W. Li. Facile stabilization of the sodium metal anode with additives: Unexpected key role of sodium polysulfide and adverse effect of sodium nitrate. *Angew. Chem. Int. Ed.*, 57(26):7734–7737, 2018.

[141] H. Wang, F. Wu, and H. Jiang. Electronic band structures of $ATaO_3$(A = Li, Na, and K) from first-principles many-body perturbation theory. *J. Phys. Chem. C*, 115(32):16180–16186, 2011.

[142] M. Wang, H. Lee, and J. Molburg. Allocation of energy use in petroleum refineries to petroleum products. *Int. J. Life Cycle Assess*, 9(1):34–44, 2004.

[143] S. Wang, Y. Rong, Y. Fan, M. Pacios, H. Bhaskaran, K. He, and J. H. Warner. Shape evolution of monolayer MoS_2 crystals grown by chemical vapor deposition. *Chem. Mater.*, 26(22):6371–6379, 2014.

[144] C. Wivel, R. Candia, B. S. Clausen, S. Mørup, and H. Topsøe. On the catalytic significance of a Co-Mo-S phase in Co-Mo/Al_2O_3 hydrodesulfurization catalysts: Combined *in situ* M*ö*ssbauer emission spectroscopy and activity studies. *J. Catal.*, 68:453–463, 1981.

[145] Y. Xie, Z. Wang, Y. Zhan, P. Zhang, R. Wu, T. Jiang, S. Wu, H. Wang, Y. Zhao, T. Nan, and X. Ma. Controllable growth of monolayer MoS_2 by chemical vapor deposition via close MoO_2 precursor for electrical and optical applications. *Nanotechnology*, 28(8):084001, 2017.

[146] F. Xiong, H. Wang, X. Liu, J. Sun, M. Brongersma, E. Pop, and Y. Cui. Li intercalation in MoS_2: In situ observation of its dynamics and tuning optical and electrical properties. *Nano Lett.*, 15(10):6777–6784, 2015.

[147] C. Xu and Q. Shi. *Structure and Modeling of Complex Petroleum Mixtures*. Structure and Bonding. Springer International Publishing, 2015.

[148] J. Xu, D. Xue, and C. Yan. Chemical synthesis of $NaTaO_3$ powder at low-temperature. *Mater. Lett.*, 59(23):2920 – 2922, 2005.

[149] K. Yang, Y. Dai, and B. Huang. Origin of the photoactivity in boron-doped anatase and rutile TiO_2 calculated from first principles. *Phys. Rev. B*, 76:195201, 2007.

[150] K. Yang, Y. Dai, and B. Huang. Study of nitrogen-concentration influence on N-doped TiO_2 anatase from first-principles. *J. Phys. Chem. C*, 111:12086–12090, 2007.

[151] K. Yang, Y. Dai, and B. Huang. Understanding photocatalytic activity of S- and P-doped TiO_2 under visible light from first-principles. *J. Phys. Chem. C*, 111:18985–18994, 2007.

[152] K. Yang, Y. Dai, and B. Huang. First-principles calculations for geometrical structures and electronic properties of Si-doped TiO_2. *Chem. Phys. Lett.*, 456:71–75, 2008.

[153] K. Yang, Y. Dai, and B. Huang. Density functional characterization of the electronic structure and visible-light absorption of Cr-doped anatase TiO_2. *ChemPhysChem*, 10:2327–2333, 2009.

[154] K. Yang, Y. Dai, B. Huang, and M.-H. Whangbo. Density functional characterization of the band edges, the band gap states, and the preferred doping sites of halogen-doped TiO_2. *Chem. Mater.*, 20(20):6528–6534, 2008.

[155] K. Yang, Y. Dai, B. Huang, and M.-H. Whangbo. On the possibility of ferromagnetism in carbon-doped anatase TiO_2. *Appl. Phys. Lett.*, 93:132507, 2008.

[156] L. Yang, P. Liu, J. Li, and B. Xiang. Two-dimensional material molybdenum disulfides as electrocatalysts for hydrogen evolution. *Catalysts*, 7, 2017.

[157] M. Yang, X. Huang, S. Yan, Z. Li, T. Yu, and Z. Zou. Improved hydrogen evolution activities under visible light irradiation over $NaTaO_3$ codoped with lanthanum and chromium. *Mater. Chem. Phys*, 121:506 – 510, 2010.

[158] Z. G. Yi and J. H. Ye. Band gap tuning of $Na_{1-x}La_xTa_{1-x}Co_xO_3$ solid solutions for visible light photocatalysis. *Appl. Phys. Lett.*, 91:254108, 2007.

[159] Z. G. Yi and J. H. Ye. Band gap tuning of $Na_{1-x}La_xTa_{1-x}Cr_xO_3$ for H_2 generation from water under visible light irradiation. *J. Appl. Phys.*, 106:074910, 2009.

[160] B. Yoosuk, J. H. Kim, C. Song, C. Ngamcharussrivichai, and P. Prasassarakich. Highly active MoS_2, $CoMoS_2$ and $NiMoS_2$ unsupported catalysts prepared by hydrothermal synthesis for hydrodesulfurization of 4,6-dimethyldibenzothiophene. *Catal. Today*, 130:14–23, 2008.

[161] J. Zhang, S. Jia, I. Kholmanov, L. Dong, D. Er, W. Chen, H. Guo, Z. Jin, V. B. Shenoy, L. Shi, and J. Lou. Janus monolayer transition-metal dichalcogenides. *ACS Nano*, 11(8):8192–8198, 2017.

[162] R. Zhang, X.-R. Chen, X. Chen, X.-B. Cheng, X.-Q. Zhang, C. Yan, and Q. Zhang. Lithiophilic sites in doped graphene guide uniform lithium nucleation for dendrite-free lithium metal anodes. *Angew. Chem. Int. Ed.*, 56:7764–7768, 2017.

[163] Y. Zhao, L. V. Goncharova, A. Lushington, Q. Sun, H. Yadegari, B. Wang, W. Xiao, R. Li, and X. Sun. Superior stable and long life sodium metal anodes achieved by atomic layer deposition. *Adv. Mater.*, 29(18):1606663, 2017.

[164] Y. Zhu, Q. M. Ramasse, M. Brorson, P. G. Moses, L. P. Hansen, C. F. Kisielowski, and S. Helveg. Visualizing the stoichiometry of industrial-style Co-Mo-S catalysts with single-atom sensitivity. *Angew. Chem. Int. Ed.*, 53(40):10723–10727, 2014.